AD-A266 318

ON PAGE

Form Approved
OMB No. 0704-0188

Public r... gathern... collectic... Davis H...

...1 hour per response, including the time for reviewing instructions, searching existing data sources, collection of information. Send comments regarding this burden estimate or any other aspect of this ...ington Headquarters Services, Directorate for information Operations and Reports, 1215 Jefferson ...gement and Budget, Paperwork Reduction Project (0704-0188), Washington, DC 20503.

1. AC... (Leave blank)	2. REPORT DATE	3. REPORT TYPE AND DATES COVERED
	June 6, 1993	Final Technical Rept. 01/01/90-12/31/92

4. TITLE AND SUBTITLE

Studies in turbulence and turbulence control

5. FUNDING NUMBERS

G-X
AFOSR-91-0139
2307/BS

6. AUTHOR(S)

K.R. Sreenivasan

7. PERFORMING ORGANIZATION NAME(S) AND ADDRESS(ES)

Yale University
9 Hillhouse Ave.
New Haven, CT 06520-2159

AFOSR-TR

8. PERFORMING ORGANIZATION REPORT NUMBER

...149

9. SPONSORING/MONITORING AGENCY NAME(S) AND ADDRESS(ES)

AFOSR/NA
Building 410
Bolling Air Force Base, D.C. 20332-6448

NA

10. SPONSORING/MONITORING AGENCY REPORT NUMBER

AFOSR-91-0139
2307/BS

11. SUPPLEMENTARY NOTES

--

DTIC
JUN 29 1993
B

12a. DISTRIBUTION/AVAILABILITY STATEMENT

Approved for public release; distribution is unlimited

12b. DISTRIBU...

UL

13. ABSTRACT *(Maximum 200 words)*

A summary of the research performed under this grant is provided. It consists of work that bears on reacting flow research as well as basic turbulence studies. In the former category, the research involves differential diffusion, photobleaching, conditional scalar dissipation, helium jets, and the thickness-distribution of OH regions in diffusion flames. In the former category, the summary is limited to Kolmogorov's refined hypothesis, self-affine traces of turbulent signals, synthetic turbulence, wavelet decomposition of turbulence and the intermittency exponent in the turbulence dissipation. Only briefly mentioned are other aspects such as the scaling of structure functions, the scaling of circulation and the effect of filtering on Kolmogorov's 4/5 relation.

14. SUBJECT TERMS	15. NUMBER OF PAGES
Differential diffusion, conditional scalar dissipation, helium jets, OH regions in flames, Kolmogorov's refined hypothesis, wavelets, intermittency	7 + three reprints
	16. PRICE CODE: --

17. SECURITY CLASSIFICATION OF REPORT	18. SECURITY CLASSIFICATION OF THIS PAGE	19. SECURITY CLASSIFICATION OF ABSTRACT	20. LIMITATION OF ABSTRACT
unclassified	unclassified	unclassified	UL

Standard Form 298 (Rev. 2-89)

DISCLAIMER NOTICE

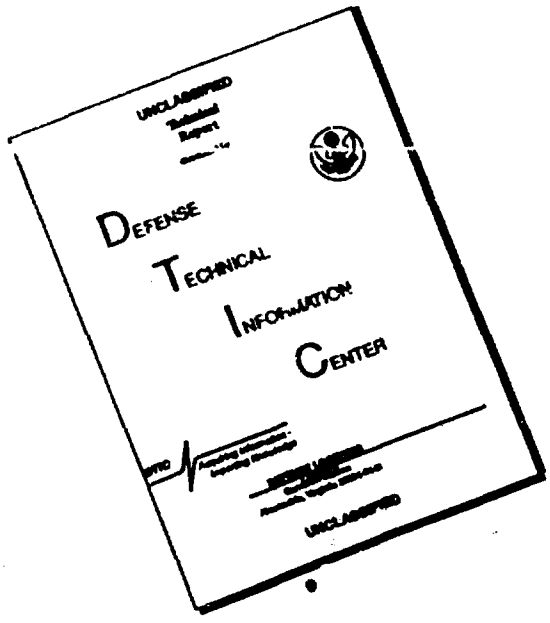

THIS DOCUMENT IS BEST QUALITY AVAILABLE. THE COPY FURNISHED TO DTIC CONTAINED A SIGNIFICANT NUMBER OF PAGES WHICH DO NOT REPRODUCE LEGIBLY.

Final report submitted to the

Air Force Office of Scientific Research

for the grant

AFOSR-91-0139

STUDIES IN TURBULENCE AND TURBULENCE CONTROL

by

K.R. Sreenivasan

Mechanical Engineering Department

Yale University

June 6, 1993

93-14808

93 6 29 060

STUDIES IN TURBULENCE AND TURBULENCE CONTROL

The following projects have been completed. A brief discussion of the work is given, and the principal publications are listed.

A. Projects which bear on research in reacting flows

1. Differential diffusion: Consider two scalars homogeneously mixed in the plenum chamber of a jet. The jet is turbulent. The two scalars have different Schmidt numbers (i.e., their molecular diffusion coefficient are different). What effect will this difference in Schmidt numbers have in the far field in the instantaneous spatial and temporal distributions of the two scalar fields? This is a fundamental issue in the context of combustion where several species with different diffusion properties are mixed by turbulence. A popular assumption made in combustion studies is that differential diffusion effects are negligible.

Experimental data on differential diffusion between two species with large and quite disparate Schmidt numbers were obtained in a turbulent water jet by optically measuring the two species concentrations simultaneously. Experimental conditions were chosen to eliminate possible inertial effects. Schmidt number ratios of 4 and 18 were considered. Differential diffusion was found to be statistically significant and to manifest at scales far larger than the Batchelor scale. In some instances, the concentration signal for the species with larger diffusivity was simply a blurred version of the other, while in some instances structures present in one signal were absent from the other. This second observation, presumably a more complex effect due to diffusion across velocity gradients, has been discussed.

The work is submitted for publication to the Journal of Fluid Mechanics as: Differential diffusion in low Reynolds number water jets, by J.R. Saylor and K.R. Sreenivasan

3. Photobleaching of sodium fluorescein in water: As a secondary outcome of the differential diffusion study, data concerning the photobleaching of sodium fluorescence in water were obtained. The importance of avoiding this effect in fluorescence studies is emphasized.

The results are available in preprint form: The temporal behavior of the photobleaching of disodium fluorescein in water, by J.R. Saylor

2. Scalar dissipation conditioned on the scalar concentration: In the pdf methods for the scalars, the quantity that needs modeling is the conditional expectation of the scalar dissipation conditioned on the scalar concentration itself. To date, there are no reliable measurements of this quantity. We have measured it in the following cases: dye concentration fluctuations in a water jet, temperature fluctuations in the wake behind a heated cylinder, and temperature fluctuations in high-Reynolds-number atmospheric turbulence. The effects of Taylor's hypothesis are tested by obtaining both spatial and temporal data. Similarly, the effect of probe resolution has also been tested by making measurements at different resolutions. Finally, the effect of using one component of the scalar dissipation instead of the sum of all its three components has been studied.

This work has been has been submitted for publication to Physics of Fluids A: Conditional scalar dissipation rates in turbulent wakes, jets and boundary layers, by P. Kailasnath, K.R. Sreenivasan and J. Saylor.

3. Helium jets: We have finally completed a detailed study of with helium jets issuing into air. The principal results were summarized in the final report on AFOSR-87-0116, and the publication summarizing the results has appeared in the Journal of Fluid Mechanics (vol. 249, pp. 619-664, 1993), and a copy is enclosed.

4. The thickness distribution of the OH regions in turbulent diffusion flames: The OH radicals in a hydrogen diffusion flame burning in ambient air were visualized using planar laser-

induced fluorescence. Local thickness of the OH regions were measured at three downstream distances. Measurements show that the thickness is distributed approximately lognormally.

The results were published as: The thickness distribution of OH regions in a turbulent diffusion flame, by A. Johnson, K.R. Sreenivasan and M. Winter, Comust. Sci. and Tech. 89, 1 4, 1992. A copy is enclosed.

B. Basic turbulence work

1. Kolmogorov's refined hypotheses: In 1962, Kolmogorov put forward a vital refinement of his earlier phenomenological theory of high-Reynolds-number turbulence. An important quantity in this description is the flux of energy ϕ_r transferred across scales of size r. Kolmogorov assumed that, in the inertial range, ϕ_r is the only relevant quantity upon which all other quantities would depend. Furthermore, he identified ϕ_r with $r\varepsilon_r$, where ε_r is the rate of energy dissipation per unit mass averaged over a volume of linear scale r. The basis of Kolmogorov's theory is contained in the following two celebrated hypotheses.

The first similarity hypothesis: If r«L, where L is a measure of the large scale of turbulence, the probability density function (pdf) of the stochastic variable

$$V = \frac{\Delta u(r)}{(r\varepsilon_r)^{1/3}}$$

depends only on the local Reynolds number $Re_r = r(r\varepsilon_r)^{1/3}/\nu$, where ν is the kinematic viscosity of the fluid and $\Delta u(r)=u(x+r)-u(x)$, u being the x-component of the velocity vector $\mathbf{u}(\mathbf{x})$ and r is measured along x.

The second similarity hypothesis: If $Re_r \gg 1$, the pdf of V does not depend on Re_r either (nor on r, and is therefore universal).

We have earlier shown that the pdf of V depends on r as well, but also showed that several other aspects of these hypotheses hold. Even before this verification, consequences of these

hypotheses had been used extensively in the turbulence literature. In spite of their widespread use, the hypotheses pose some troubling problems; the primary shortcoming is that they have not yet been derived from basic principles. Under the assumption of statistical independence of velocity increments across scales of the order of the Kolmogorov scale, we have been able to show that a modified version of Kolmogorov's refined similarity hypotheses follows purely from probabilistic arguments. The connection of this result to three-dimensional fluid turbulence has been discussed. It has been shown that the physical picture of a cascade need not be assumed *a priori*, but rather as an *a posteriori* interpretation.

The work will appear in an AIP book as: Independent velocity increments and Kolmogorov's refined similarity hypothesis, by G. Stolovitzky and K.R. Sreenivasan

2. *Self-affine time traces of turbulent signals:* Consider a snapshot of a turbulent flow, and define iso-velocity or iso-concentration surfaces in that snapshot. Previous studies have shown that such surfaces are self-similar and can be characterized by fractal dimensions. In contrast, consider a time trace of temperature or velocity at a single point in a turbulent flow. For such quantities, the abscissae (i.e., time) and the ordinate (i.e., temperature or velocity) are two very dissimilar entities, and the signal can be rendered into a variety of objects by stretching one or the other axis. For example, by stretching the time axis, one can make the signal look very smooth; it will then have a dimension of unity. By compressing the time axis, the signal can be made very rough and almost space-filling. These curves are therefore harder to characterize in terms of fractal dimensions. We have finally understood the way in which this can be done.

The material is written up for publication as: Fractal dimensions of time series in turbulent flows, by K.R. Sreenivasan and A. Juneja, submitted to J. Fluid Mech., 1992

3. *Synthetic turbulence:* On the basis of the fractal and multifractal work with which we have been concerned so far, we have been able to outline a scheme for constructing a stochastic field that differs in no significant way statistically from velocity fluctuations in high-Reynolds-number

turbulence. We designate this field as synthetic turbulence. The scheme for generating synthetic turbulence consists of the following three ingredients, implemented here in one dimension. From such signals, one can construct velocity increments, box-averaged dissipation rate, Kolmogorov's universal variable V, all of which have the same properties as their counterparts in the real signal. Also, properties such as the power spectral density, correlation function, fractal dimensions, etc can be duplicated. The importance of this finding is two-fold:

(a) It shows that the physical picture we have of the turbulence dynamics in high-Reynolds-number turbulence is essentially correct up to some level of accuracy.

(b) If one can generate a field that is so close to turbulence, such a field can serve as good initial conditions for direct numerical simulations.

The work is available in the form of a preprint as: Synthetic turbulence, by A. Juneja, D.P. Lathrop, K.R. Sreenivasan and G. Stolovitzky.

4. The wavelet decomposition of turbulence: The wide range of spatial and temporal scales excited in fully turbulent flows have been historically represented by Fourier modes. It has been recognized recently that wavelets possess several advantages over Fourier modes, especially in strongly inhomogeneous shear flows dominated by localized structures. We apply wavelet transform to independent realizations of two-dimensional sections of the dye concentration field in turbulent water jets at moderate Reynolds numbers, and show that the smaller the scale the more stringy it is in two-dimensional intersections. The transformation from the large scale to small scale can be better described by a self-affine process associated with the stretching due to the velocity field rather than by a strictly self-similar process characterized by a geometrically similar break down process. Statistical measures such as the number of structures at a given scale and the average aspect ratio of these structures are calculated. We also analyze the space-time data on two-dimensional sections of the concentration field, and analyze interactions of various wavelet scales. A principal conclusion to emerge from the analysis is that the wavelet coefficients which are disparate in scale or separated widely in space are nearly statistically independent. This notion has been put to use in predicting the probability density function of wavelet coefficients (wpdf). A theory has been worked out for the wpdf for passive scalars in turbulent flows, and the resulting equations are closed by invoking the Fokker-Planck

approximation as well as the statistical independence of wavelet coefficients. The theory is compared with the results from experiments. It is found that the theory works well for large and intermediate scales but not for the small scales. The reasons for this failure of the theory have been explored, and it is shown that a particular form of statistical dependence makes the theory in agreement with the experiment.

One paper has been written and submitted to Physics of Fluids A: The wavelet coefficient probability density function for turbulent flows, by P.L. Similon and K.R. Sreenivasan. A seconfd paper is available in draft form as: The multiscale structure of turbulent water jets, by K.R. Sreenivasan and R.M. Everson

5. An update on the intermittency exponent in turbulence: The issue of the experimental determination of the intermittency exponent , m, is revisited and it is shown that the 'best' estimate for it is 0.25±0.05. This 'best' estimate is obtained from recent atmospheric data, and is based on several different techniques of measurement. The work appeared in Phys. Fluids A, and a copy is enclosed.

6. Other work: Aspects such as the scaling of the structure functions in the inertial as well as dissipative scale ranges, the effect of filtering on the Kolmogorov's 4/5 relation, the scaling relations of circulation, have been studied in some detail. They will not be reported here. As and when the results appear in print, copies of the papers will be mailed to AFOSR.

J. Fluid Mech. (1993), *vol.* 249, *pp.* 619–664
Copyright © 1993 Cambridge University Press

The instability and breakdown of a round variable-density jet

By D. M. KYLE AND K. R. SREENIVASAN

Department of Mechanical Engineering, Mason Laboratory, Yale University, New Haven, CT 06520, USA

(Received 23 May 1991 and in revised form 10 November 1992)

A study has been made of the instability and the subsequent breakdown of axisymmetric jets of helium/air mixtures emerging into ambient air. Although the density of the nozzle gas is less than that of the ambient fluid, the jet is essentially non-buoyant. Two kinds of instability are observed in the near field, depending upon the mean flow parameters. When the ratio of the exiting nozzle fluid density to ambient fluid density is $\rho_e/\rho_\infty > 0.6$, shear-layer fluctuations evolve in a fashion similar to that observed in constant-density jets: the power spectrum near the nozzle is determined by weak background disturbances whose subsequent spatial amplification agrees closely with the spatial stability theory. When the density ratio is less than 0.6, an intense oscillatory instability may also arise. The overall behaviour of this latter mode (to be called the 'oscillating' mode) is shown to depend solely upon the density ratio and upon D/θ, where D is the nozzle diameter and θ is the momentum thickness of the boundary layer at the nozzle exit. The behaviour of this mode is found to be independent of the Reynolds number, within the range covered by the present experiments. This is even true in the immediate vicinity of the nozzle where, unlike in the case of shear-layer modes, the intensity of the oscillating mode is independent of background disturbances. The streamwise growth rate associated with the oscillating mode is not abnormally large, however. The frequency of the oscillating mode compares well with predictions based on a spatio-temporal theory, but not with those of the standard spatial theory.

From high-speed films it is found that the overall structure of the oscillating mode repeats itself with extreme regularity. The high degree of repeatability of the oscillating mode, in association with a strong pairing process, leads to abnormally large centreline velocity fluctuation, with its root-mean-square value being about 30% of the nozzle exit velocity. Energetic and highly regular pairing is found also to lead to the early and abrupt breakdown of the potential core. The regularity often extends even to the finer structure immediately downstream of the breakdown. An attempt is made to explain these special features both in terms of the large-amplitude vorticity field, and in terms of the theoretically predicted space–time evolution of wave packets.

1. Introduction

Except at very low Reynolds numbers, a laminar shear layer with constant density is unstable to arbitrarily small disturbances. These disturbances evolve by selective amplification as they convect downstream (Cohen & Wygnanski 1987). The migration of vorticity resulting from the instability forms axisymmetric or helical structures accompanied by large-amplitude fluctuations. Generally, these structures interact with one another and contribute significantly to entrainment and mixing by convective

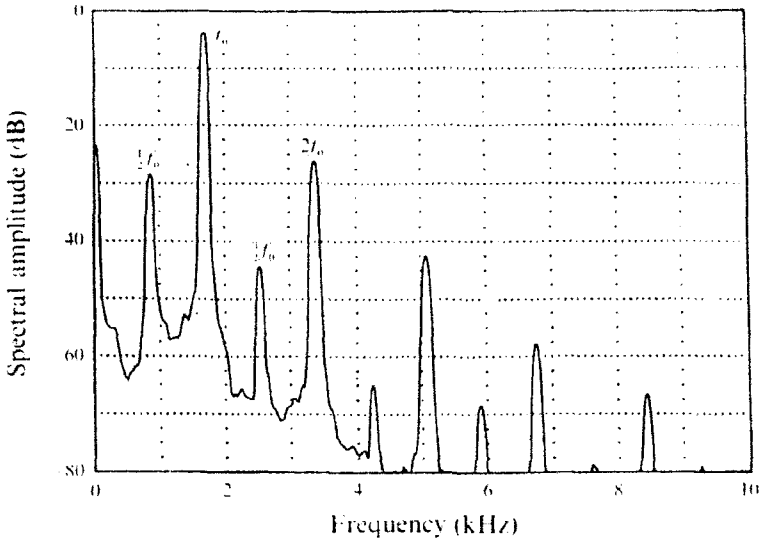

FIGURE 1. Power spectral density in a helium jet ($S = 0.14$), showing large peaks at f_0, its subharmonic, $\frac{1}{2}f_0$, and several harmonics. The hot wire was located along the jet centreline at 1.33 diameters downstream of the nozzle exit. The frequency f_0 of the oscillating mode does not depend on the spatial position in that region. (Taken from Sreenivasan *et al.* 1989.)

transport (Winant & Browand 1974), and to the generation of acoustic noise (Crighton 1975; Sarohia & Massier 1977; Kibens 1980). Very often, engineering interest arises when the nozzle fluid density ρ_0 is significantly less than the ambient fluid density, ρ_∞. The kinematics and dynamics in the near field of variable density jets is the focus of the present study. Before discussing its specific objectives, it is helpful to review the previous literature on the subject. This is best done by reviewing the experimental and theoretical studies separately.

1.1. *Experiment*

Several early studies indicate that the mean flow evolution in the near field can be sensitively dependent upon the density ratio, $S = \rho_0/\rho_\infty$. Corrsin & Uberoi (1949) measured the temperature and velocity fields for various nozzle gas temperatures in heated air jets. For temperatures corresponding with $S = 0.95$ and 0.62, they found that the potential core terminated at $x/D \approx 5$, where x is the distance along the axis and D is the nozzle orifice diameter. When S was decreased to 0.49, however, the potential core terminated at $x/D \approx 3.5$, followed by a relatively sharp drop in the centreline temperature and velocity. Beyond the potential core, the jet width for $S = 0.49$ was approximately twice that for $S = 0.95$. Data obtained by Landis & Shapiro (1951) and Sforza & Mons (1978) in heated air jets, and by Chriss (1968), Tombach (1969) and by Abramovich *et al.* (1969) in heterogeneous jets confirm that, below $S \approx 0.60$, mixing processes are significantly enhanced in the near field. Abramovich *et al.* (1969) measured the spread rate of the shear layer and found that in addition to the dependence on the density ratio, spread rates were also sensitively dependent upon the jet Reynolds number and upon the initial shear-layer thickness.

There is evidence to suggest that the mean flow variations described above may be linked to abnormally intense instability modes sustained only when the density ratios are small. Smith & Johannesen (1986) obtained power spectra using microphones located in the acoustic far field of helium/argon jets issuing into air. In pure helium jets

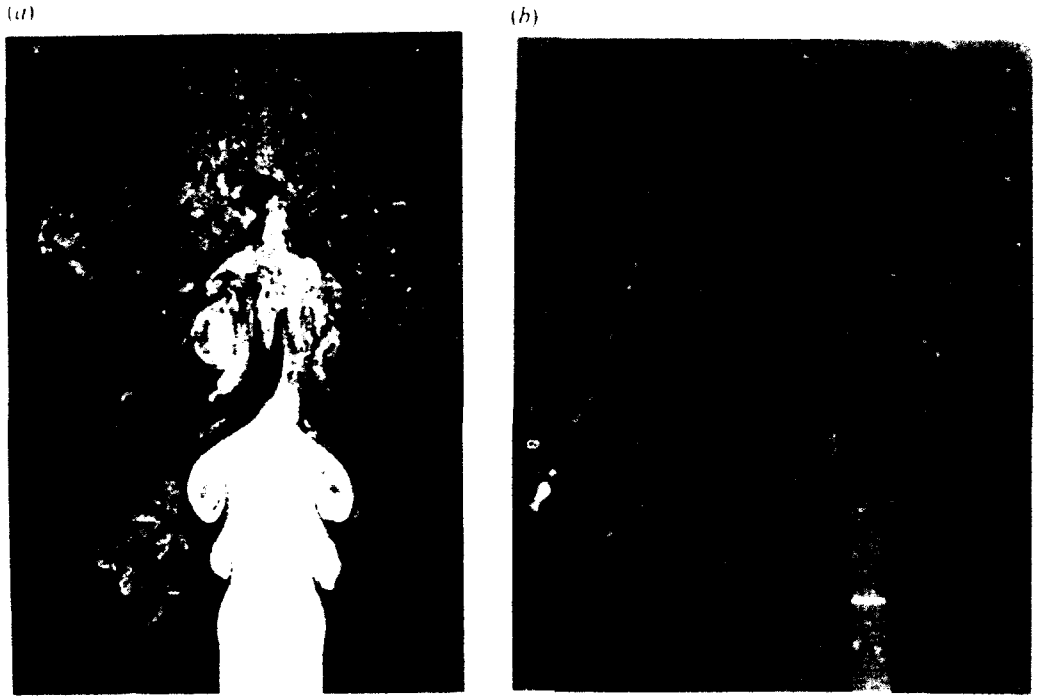

FIGURE 2. *(a) Instantaneous digital image* of the aerosol distribution in the axial plane of a seeded flow. A single pulse from a YAG laser illuminates the flow. $S = 0.29$. (Taken from Kyle 1988.) *(b)* A typical realization of the helium jet issuing from the nozzle into ambient air; the jet spreads very rapidly beyond a reasonably well-defined streamwise position. The figure is taken from Sreenivasan *et al.* (1989), where details are given of how this picture was obtained; see also §2 of the text. $Re = 1400$, $S = 0.14$, nozzle diameter = 6 mm.

they discovered an oscillatory jet instability for Mach numbers below 0.56. Reminiscent of the mean flow results of Abramovich *et al.* (1969), this instability was found to depend upon the precise nozzle contour. The density dependence of jet noise for higher velocities is reported by Hoch *et al.* (1973) and by Chan & Leong (1973). Kyle (1986) and Sreenivasan, Raghu & Kyle (1989) examined spectra obtained along the centreline of low-speed helium/air jets, and found that the jet instability of the type observed by Smith & Johannesen is sustained in jets with density ratios at least as large as 0.5. These authors showed that the oscillatory behaviour can dominate the flow in the entire near field (see figure 1). Monkewitz *et al.* (1990) have obtained similar results in heated air jets.

The observation that the spectral density function is dominated by a discrete frequency spike of large magnitude and its higher harmonics, quite unlike the situation in constant density jets, suggests the occurrence of a new phenomenon. The time records used for calculating these spectra are so long that many wave crests pass by the fixed hot-wire position during a single time record. In order to produce such 'spiky' spectra, there must be relatively little random variation from one passing structure to the next, or the modes must preserve their phase over many cycles. Stationary images in the near field of variable-density jets reveal that the spiky power spectra are indeed accompanied by extremely coherent ring vortices formed along the jet column, as exemplified by figure 2(*a*) and other photographs presented by Kyle (1988), Sreenivasan *et al.* (1989) and Monkewitz *et al.* (1989). We shall denote this henceforth as the 'oscillating mode'. Radial profiles of the mean temperature (Monkewitz *et al.* 1990)

suggest that these structures may be unusually effective in convective transport. The variable-density jet can undergo a catastrophic spread near the end of the potential core, as seen in figure 2(*b*) (see also Sreenivasan *et al.* 1989; Monkewitz *et al.* 1989). This spread is associated with the radial ejection of fluid in the form of 'side jets' (Monkewitz *et al.* 1989), which may be due to the growth of azimuthal instabilities in the highly strained region between the vortex rings (Liepmann 1991). At the end of the potential core, the ring structures vanish (figure 2). Power spectra generally show that the subharmonic reaches its maximum towards the end of the potential core (Kyle 1986, 1988), suggesting the occurrence of vortex pairing (Ho & Huang 1982).

In addition to variable-density jets, several other flows such as wakes (e.g. Strykowski & Sreenivasan 1990) and countercurrent shear layers (e.g. Strykowski & Niccum 1992) show similarly well-ordered structure under certain conditions. Partly in an effort to explain these observations, the theoretical framework of space time instability of fluid flows has seen a resurgence in the last few years. Since we wish to remark on the applicability of the theory to our experiments, it is necessary to review the theory briefly.

1.2. *Theory*

Even though the organized state that we are trying to explain here is highly nonlinear, the theory – which purports to explain the onset of this state – is linear. Unlike temporal instability of the basic state where one considers the growth in time of spatially periodic perturbations, or the spatial instability where one considers the steady-state response of the basic state to spatially localized but time-periodic disturbances, it has been found more useful to study the response of a quiescent system for $t < 0$, perturbed impulsively by a disturbance of the form $\sim \delta(x)\delta(t)$. The resulting disturbance takes the form of a wave packet, as discussed by Sturrock (1958), Briggs (1964), Gaster (1968*a*, *b*) and Huerre & Monkewitz (1985), among others. The wave packet may be regarded as the Green function from which the complete response to any distributed perturbation can be deduced.

Using closely related formulations, Briggs (1964) and Gaster (1968*a*, *b*) have shown that if the wave packet evolves over a long period of time, then the motion at every point (x, t) in the physical plane which results from a single pulse perturbation can be associated with a specific wavenumber k. Thus for quite general conditions (Bers 1983), along each trajectory x/t = constant the fluid motion is eventually dominated by a single complex wavenumber k^*, which simultaneously must satisfy the two relations:

$$\partial\omega_i(k^*)/\partial k_r = 0, \tag{1.1}$$

$$\partial\omega_r(k^*)/\partial k_r = x/t. \tag{1.2}$$

We may view (1.1) and (1.2) as determining $k^*(x/t)$ for any given x/t. Note that the functions ω_r, ω_i are just the real and imaginary components of the dispersion relation.

Our intention is not to review the mathematics which leads to (1.1) and (1.2), but to point out its physical content to the extent needed here. Each wave excited by the impulse perturbation immediately starts to grow (or attenuate) and propagate at a distinct, finite rate. In due course, the energy associated with certain of these modes will tend to prevail in particular locations. To see which modes prevail and at what locations, let us imagine several observers of this system, each moving at a different speed x/t. At first, each observer may notice many of the excited waves that are propagating at his speed, but one wave will eventually dominate his field of view; it is the wave which simultaneously has an associated real group velocity that matches the observer's speed (equation (1.2)), and has a transient growth rate ω_i that is a maximum

in the sense of (1.1). If several wavenumbers $k^*(x/t)$ satisfy (1.1) and (1.2), the one which has the largest growth rate will dominate. Because there is only a single dominant mode at large time for each x/t, the disturbance will appear to each observer as a discrete frequency wavetrain having wavelength $k^*(x/t)$ and frequency $\omega_r(k^*)$, and will appear to grow in space and time as $\sim \exp[-(k_i^*(x/t))x + \omega_i(k^*)t]$.

In certain systems, the wave packet will evolve in such a way that the observer moving with speed $x/t = 0$ will see the mode with wavenumber $k^*(0)$ grow with time, i.e. that $\omega_i(k^*(0)) > 0$. As pointed out earlier, this mode alone will eventually dominate the observer's field of view. This behaviour has been analysed explicitly by Gaster (1968*a*), Briggs (1964) and others (see the review by Huerre & Monkewitz 1990), and is called 'absolute instability'. It has further been shown that when $\omega_i(k^*(0)) > 0$, discrete frequency oscillations will evolve near the origin not only in response to an impulse perturbation, but also in response to nearly any spatially localized perturbation with arbitrary time dependence (see Briggs 1964, §2.3.5). Often in real flows, natural excitation resembles a continual random process that is localized in space (e.g. at the system boundary). It is therefore compelling to conjecture that if such a flow resembles in some approximate sense an absolutely unstable system, it may support oscillatory instabilities of the sort described earlier.

Gaster & Davey (1968) have examined the wavepacket which evolves from an impulse perturbation in the inviscid wake. In this study, $k^*(x/t)$ and $\omega(k^*)$ were calculated for a range of x/t. The particular wake profiles which they examined were not absolutely unstable. Huerre & Monkewitz (1985) have evaluated the impulse response in a plane shear layer between two parallel streams, and found for certain countercurrent flows that $\omega_i(k^*(0)) > 0$, i.e., if perturbed locally, this idealized system will eventually develop oscillations with frequency $\omega_r(k^*(0))$ at fixed points surrounding the space–time origin. Koch (1985) has examined the wake for a broad range of profiles and found that the wake can also be absolutely unstable. Pavithran & Redekopp (1989) have studied the impulse response for variable-density shear layers, while Monkewitz & Sohn (1986, 1988) have examined heated round jets. These latter authors found for a family of density and velocity profiles that the jet is absolutely unstable when S is sufficiently small.

1.3. *Motivation for the present work and the organization of the paper*

This experimental investigation is aimed at obtaining a clearer physical understanding of unstable modes which evolve in the near field (or the transition region) of variable-density jets. A key feature of these experiments is that they are well controlled, in that they explore – within the ranges covered – the dependence of the flow on each of the important governing parameters separately, while the others are fixed. We have chosen conditions for which the flow is incompressible and buoyancy effects are negligible.

We had earlier (Kyle 1986; Sreenivasan *et al.* 1989) performed an experimental investigation of the S-dependence of the oscillatory mode, and found that at some jet speeds, the measured onset value of S roughly corresponded with the theoretical value for which $\omega_i(k^*(0))$ first became positive. Monkewitz *et al.* (1990) found this behaviour in heated jets as well, and further observed that the Strouhal number generally falls within the range predicted by their theory. Detailed quantitative comparisons between theory and observation for corresponding values of governing parameter values have not been made, primarily because of the lack of experimental control already discussed. An added motivation for the present study is to compare, where possible for a relatively wide parameter range, the predicted parametric dependence of the onset of the instability with the observed behaviour.

The rest of the paper is organized as follows. After a discussion in §2 of the experimental conditions, we discuss in §3 the parameters governing the jet behaviour near the onset of oscillating mode and argue that it should depend essentially upon the Reynolds number, the density ratio, the ratio of nozzle diameter to shear-layer thickness, and background disturbances. In §4, we discuss measurements focusing on obtaining a time-resolved kinematic description of the oscillating mode and its subsequent breakdown process; using a set of high-speed films obtained for a range of parameter values, in conjunction with laser Doppler velocimetry measurements, we study the growth and interaction of large-amplitude waves associated with both the oscillating mode and normal shear layer modes. In §5, we concentrate on features of the power spectrum obtained in the region close to the nozzle exit, where the disturbances are small; we study the intensity and the frequency of each kind of mode as functions of the four governing parameters and of the streamwise distance. Emphasis is placed on the behaviour of the oscillating mode near onset, and on distinguishing the different kinds of instability existing in variable-density jets. Where appropriate, comparisons between experiment and theory are noted. As an aid to understanding the origin of the oscillating mode, we discuss in §6 its response to acoustic forcing and other changes in the environment. The paper concludes with §7 in which the nature of the oscillating mode is discussed in terms of both vorticity and the space time instability. The Appendix summarizes certain issues involved in interpreting the hot-wire measurements made in the inhomogeneous flow considered here.

2. Experimental arrangement

The jet facility consists of a stainless steel settling chamber with screens of varying gradation and a capability for attaching matching nozzles of different exit diameters. The nozzle and the settling chamber are movable while the optical table surrounding the nozzle is fixed, making measurements at various streamwise locations relatively easy. Details of the facility are described in Stein (1969). Measurements were made with nozzles of 9.3 and 13.3 mm, both machined from aluminium stock. The 9.3 mm nozzle (contraction ratio 190) is designed using a cubic equation for the contour (Hussain & Ramjee 1976), and the 13.3 mm nozzle (contraction ratio 93) is designed with an ASME series low β contour (Bean 1971).

Various densities of the jet fluid were obtained by mixing helium and air in desired proportions. Before being mixed, the helium and air flow rates were metered separately using calibrated rotameters. The calibrations were carried out separately by correlating the rotameter readings with the volumetric discharge Q through the nozzle. Q was calculated using

$$Q = \pi[\tfrac{1}{2}D - \delta^*]^2 U_{\infty}, \tag{2.1}$$

where D is the exit diameter of the nozzle, U_{∞} is the potential core velocity in the exit plane (found to be uniform except for the boundary layer), δ^* is the displacement thickness associated with the boundary layer at the nozzle exit. The displacement thickness was measured directly, as described in §3. U_{∞} was determined by measuring the pressure drop through the nozzle with a Baratron pressure transducer (Type 370H-10), and using Bernoulli's formula.

A few critical velocity measurements were made using a TSI laser-Doppler velocimeter (LDV) operated in forward-scatter mode; an aerosol of water droplets was used for seeding particle. A hot wire (5 μm diameter, 0.6 mm active length), operated

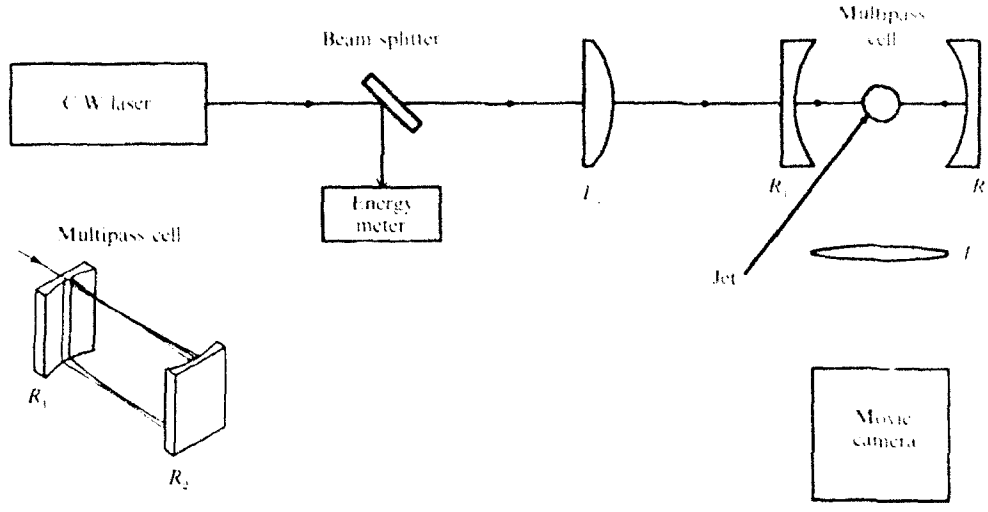

FIGURE 3. Experimental configuration used for obtaining high-speed motion pictures of the aerosol field in a gas jet. Framing speed was 7000 f.p.s. R_1 and R_2 are two concave cylindrical reflectors which create an intense plane of illumination.

on constant temperature mode on the DANTEC 55M01 anemometer, was also used to measure velocity in air jets. In heterogeneous regions, the hot wire cannot, in general, be used for determining the absolute value of the velocity, because the signal E is a function of both velocity $u(t)$ and local helium concentration $c(t)$, i.e. $E = E(u(t), c(t))$. One can always measure the velocity inside the potential core where the fluid is homogeneous, but such probe intrusion can significantly alter the stability characteristics of the oscillating mode (see Sreenivasan *et al.* 1989). Unless otherwise stated, the hot wire was positioned outside the shear layer at $r = \frac{1}{2}D + 5\theta$. It is shown in the Appendix that normalized power spectra obtained at this location are approximately the same as the normalized power spectra of u' obtained inside the potential core, as long as the disturbances are small. Spectral density curves were obtained on a single channel HP Spectrum Analyser (model 3561A). This device displays a discretized spectrum using 400 equal subintervals, or 'lines' to span the desired frequency interval. Several standard spectral windows can be used with the fast Fourier transform (FFT) algorithm. We have always chosen to use a 'flat top' window. A few of the spectral measurements to be reported are concerned with the 'width' of a given peak in the power spectrum. For such measurements, the bandwidth and centre frequency of the spectrum analyser display were adjusted so that the spectral peak spanned a number of lines which was of the order of 10^2. This practice was found to minimize the effects of discretization on this type of measurement.

High-speed motion pictures were made of the jet by illuminating the flow with a narrow sheet of continuous laser light (7 W) in a plane coinciding with the jet axis. Motion pictures were obtained using a Wollensak 'Fastax WF6' 16 mm motion picture camera with 400 ASA movie film. In order to capture several frames within one oscillation cycle, it was necessary to film at high repetition rates, and the film speed ranged up to 7000 s^{-1}. This required intense illumination for adequate quality of the images. The laser sheet was therefore formed using a 'multipass cell' as shown in figure 3. The laser light was reflected back and forth between the two concave cylindrical reflectors creating an intense plane of illumination without ever passing through a

diverging lens. This method is discussed by Long *et al.* (1983). The nozzle fluid was made visible by seeding it with a polydisperse aerosol of water droplets doped with a fluorescent dye (sodium fluorescene). The droplets were generated using a TSI aerosol generator (model 9306). Instantaneous images were obtained using a pulsed Nd:YAG laser. In this case, the laser sheet was formed using a concave cylindrical lens to diverge the beam in the axial plane, and a convex cylindrical lens to converge the beam in the horizontal plane. The laser had a power density of 2×10^7 J s^{-1} per pulse and a pulse duration of about 10 ns. The images were captured on a Photometrics 'IC200' CCD array with a 1300×1035 pixels, and were processed using in-house software (Prasad & Sreenivasan 1990).

3. Governing parameters

Separated free shear flows of heterogeneous composition can potentially depend upon a large number of parameters. However, by limiting the range of flow conditions and by exploiting justifiable approximations, one can construct a set of experiments whose outcome depends upon just a few non-dimensional parameters. We chose at the outset to limit this study to Mach numbers $M = U_e/a_s$ less than 0.3; here a_s is the sound speed for the ambient air. For most of the experiments, M was substantially smaller. Under these conditions, the Mach number effects are uniformly small. Experiments of Bradshaw (1966) in isothermal air jets suggest the same (see also §5.1); straightforward scaling arguments applied to the full energy equation (Kyle 1991) suggest that this is so also for the variable density case. Thus, the non-dimensional governing equations depend upon the Reynolds number $Re = U_e D/\nu_e$, the Richardson number $Ri = (\rho_e - \rho_s) Dg/\rho_s U_e^2$, and the Schmidt number $Sc = \nu_s/D_{\mathrm{He,air}}$. Here, $D_{\mathrm{He,air}}$ is the diffusivity of helium into air, g is the acceleration due to gravity, and ν_e is the kinematic viscosity of the nozzle fluid, which itself can be calculated using Wilke's (1950) approximation based on the statistical mechanical theory of Chapman–Enskog. In the present experiments, the Richardson number $Ri \leqslant 1.4 \times 10^{-4}$, and so the buoyancy effects are negligible (Kotsovinos 1975). Further, although Schmidt number effects may not be neglected *a priori*, Sc is not an experimental variable in this study because $D_{\mathrm{He,air}}$ is essentially independent of the relative concentrations of helium and air (Geankoplis 1972).

3.1. *Inflow boundary conditions*

The flow everywhere upstream of the nozzle exit is slow and has uniform composition. Reynolds number similarity therefore assures us that the non-dimensional velocity distribution at the nozzle exit is a unique function of the Reynolds number. Figures 4(*a*, *b*) show radial profiles of the streamwise velocity $U(r)/U_e$ obtained in the separated boundary layer for the 13.3 and the 9.3 mm nozzles, respectively, over the Re range covered in the experiments. The profiles are similar and agree closely with the Blasius profile. For all profiles, δ^*/θ was within $\pm 4\%$ of the Blasius value. Here, θ is the momentum thickness defined by

$$\theta = \int_0^{r_{0.1}} (U(r)/U_e)[1 - U(r)/U_e]\,\mathrm{d}r, \tag{3.1}$$

and δ^* is the equivalent plane displacement thickness defined by

$$\delta^* = \int_0^{r_{0.1}} [1 - U(r)/U_e]\,\mathrm{d}r. \tag{3.2}$$

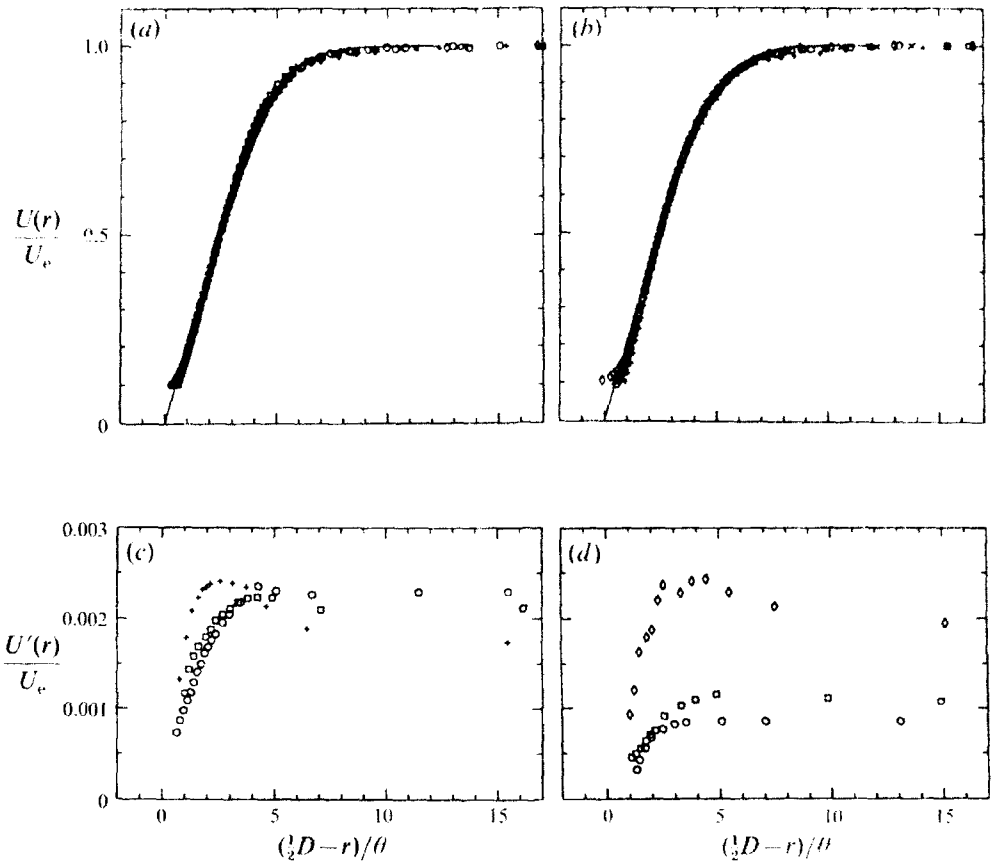

FIGURE 4. Variation of streamwise velocity in the nozzle plane ($x = 0.06$ mm) at various Reynolds numbers: ○, $Re = 16000$; □, $Re = 7000$; ×, $Re = 5000$; ∗, $Re = 3500$; +, $Re = 2700$; ◇, $Re = 2100$. (*a*) $U(r)/U_e$ for ASME nozzle. $D = 13.3$ mm; (*b*) $U(r)/U_e$ for cubic equation nozzle. $D = 9.3$ mm. (*c*) Fluctuation amplitude u'/U_e for ASME nozzle; $D = 13.3$ mm. (*d*) Fluctuation amplitude u'/U_e for cubic equation nozzle; $D = 9.3$ mm. Measurements are obtained using a standard hot wire in air jets.

The upper limits of integration $r_{0.1}$ signify the location where $U(r)/U_e = 0.1$. The longitudinal velocity fluctuation intensity profiles $u'(r)/U_e$ (figures 4(*c*, *d*)) exhibit peaks at $(\frac{1}{2}D-r)/\theta = 3$, this being typical of jets with initially laminar shear layers (Hussain & Zedan 1978). Centreline values $u'(0)/U_e$ at various speeds U_e were in the range 0.08–0.19% in the 9.3 mm cubic equation nozzle, and 0.17–0.23% for the 13.3 mm ASME nozzle. Both the mean and fluctuating velocity data indicate that the boundary layers separating at the lip of the nozzle are laminar over the Re range considered. Because the separated boundary layers are laminar, and their shapes are essentially invariant, the parameter θ fully characterizes the normalized velocity profiles, so that an appropriate non-dimensional ratio is D/θ. Figure 5 shows D/θ values calculated from the above profiles. For all the data presented here, D/θ will be reported – from which the corresponding value of Re can be found from figure 5.

The jet is isothermal, as confirmed by direct measurements. The density ratio $S = \rho_e/\rho_r$ is therefore just equal to the ratio of the molecular weight of the helium/air mixture to that of air since, for low Mach numbers, the effect of pressure on the density is negligible. With these assumptions, it is easy to show (Kyle 1991) that all other (non-

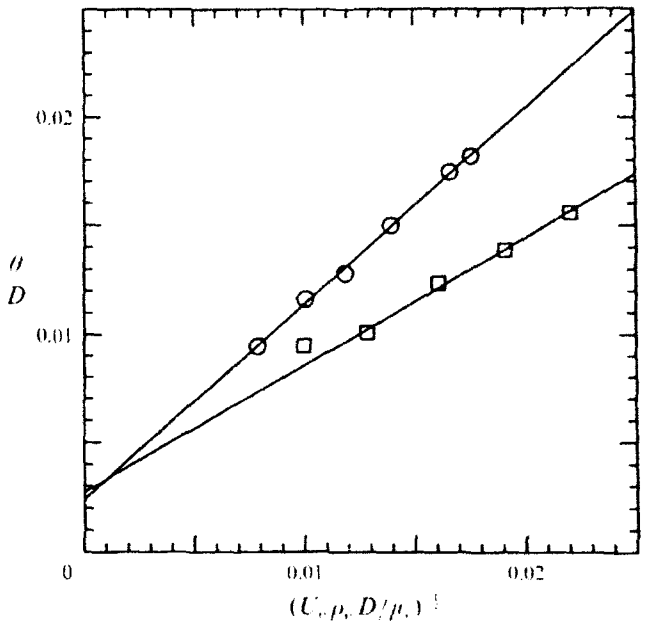

FIGURE 5. Momentum thickness θ/D as a function of the Reynolds number Re: ○, 13.3 mm ASME nozzle; □, 9.3 mm cubic equation nozzle.

dimensionalized) thermophysical properties of the nozzle fluid, such as the kinematic viscosity ratio ν_c/ν_∞ are uniquely specified by S.

3.2. *Overall parameter dependence*

The analysis so far suggests that all non-dimensional characteristics of the flow should depend primarily upon the global parameters D/θ, S and Re. A major goal of this paper is to evaluate the dependence of the oscillating mode of these three global parameters. As we are interested in the growth of small disturbances in the near field, it is also important to take account of the effects of the time-dependent disturbances imposed on the flow. These are due to acoustic noise and to vortical disturbances originating upstream of the nozzle. Such background disturbances may, under certain circumstances, strongly affect the flow, though they may be weak (Cohen & Wygnanski 1987; §5 of present paper).

Finally, it is of interest to note that in the limit $Re \to \infty$ and $M \to 0$, the system of equations and boundary conditions governing the heterogeneous, isothermal flow is analogous to those governing the heated air jet (Brown & Roshko 1974; Kyle 1991). Whenever possible we shall compare our measurements with results obtained by Monkewitz *et al.* (1989, 1990) and Raghu & Monkewitz (1991) in heated air-jet experiments for similar values of D/θ and S.

4. Evolution of highly organized structures in the near field

Before proceeding further, it is helpful to have an overall kinematical description of the transition from organized to disorganized states in variable-density jets. At the instant shown in figure 2(*a*), an axisymmetric wave appears close to the nozzle and is followed by two vortex rings in the streamwise direction; beyond this, the nozzle fluid necks down and finally 'pinches off', leading to a disorderly structure downstream. A

D/θ	92	69	69	**69**	60	60	**60**	50	**50**
S	1.0	0.66	0.48	**0.29**	1.0	0.58	**0.48**	0.48	**0.29**
λ/θ	38	37	35	**44**	36	31	**38**	37	**39**
L/θ	125	120	85	**67**	132	146	**75**	110	**47**

TABLE 1. λ/θ and L/θ as measured directly from the films; $D = 13.3$ mm. Values represent an average of 100 successive eddies. Jets dominated by the oscillating mode are indicated in bold print.

region of fluid having a relatively low concentration of nozzle gas surrounds the disorderly structure and extends beyond the range of the image. In order to study the history and interaction of these structural elements, high-speed motion pictures have been made of the transition region of the jet issuing from the 13.3 mm nozzle for nine different combinations of the governing parameter S, D/θ and Re. The density ratios range from unity (air into air) down to $S = 0.14$ (pure helium into air) while D/θ lies roughly between 50 and 91 (see table 1). LDV measurements are correlated with the films for the same flow conditions. The results of this effort are summarized below.

4.1. *General observations*

In certain visual respects, the evolution of large-amplitude structures was found to be similar for all nine flow conditions considered. Instability waves which form in the initially laminar shear layer are always axisymmetric; between 1 and 2.5 diameters downstream of the nozzle, these waves fold or 'break' and quickly roll up to form a train of vortex rings, the centres of which continually move downstream. These are the vortex ring structures seen in figure 2(*a*). When the oscillating mode is present, each vortex ring is involved in exactly one pairing inside the viewing region ($0 \leqslant x/D \leqslant 4.75$), whereas in jets not supporting the oscillating mode, the interaction is less repeatable and a vortex ring occasionally passes from view without coalescence.

The pairing process itself can be seen in the sequence of ten successive movie frames of figure 6. These frames advance from left to right, with the left-most frame in the bottom row immediately following the last frame in the top row. By comparing frames 1 and 6, 2 and 7, and so forth, it is seen that the overall structure in the transition region repeats itself to a remarkable degree; even the fine structure downstream of the potential core termination repeats for many cycles. It is evident that the processes involved in the growth, interaction and breakdown of vortices all evolve temporally in a periodic fashion.

While these pictures are quite instructive, they do not tell the whole story: flow visualization experiments in constant density jets also show some repeatability of structure interactions at low Reynolds numbers below about 10^4 (Becker & Massaro 1968; Browand & Laufer 1975; Davies & Baxter 1977). However, for nozzle Reynolds numbers of the order 10^5 and above, there is much less repeatability in constant-density jets; further, the initial instability of the laminar shear layer could be both axisymmetric and helical (Browand & Laufer 1975; Drubka & Nagib 1981) – quite unlike the situation here.

The differences between the two classes of jets are quantified in the remaining subsections.

4.2. *The disturbance wavelength and wave-breaking length*

Two lengthscales which characterize the disturbances in a shear layer are: (i) the wave-breaking length, L, and (ii) the disturbance wavelength, λ. These are defined in figure 7. Their values, as deduced from the high-speed motion pictures, are summarized in

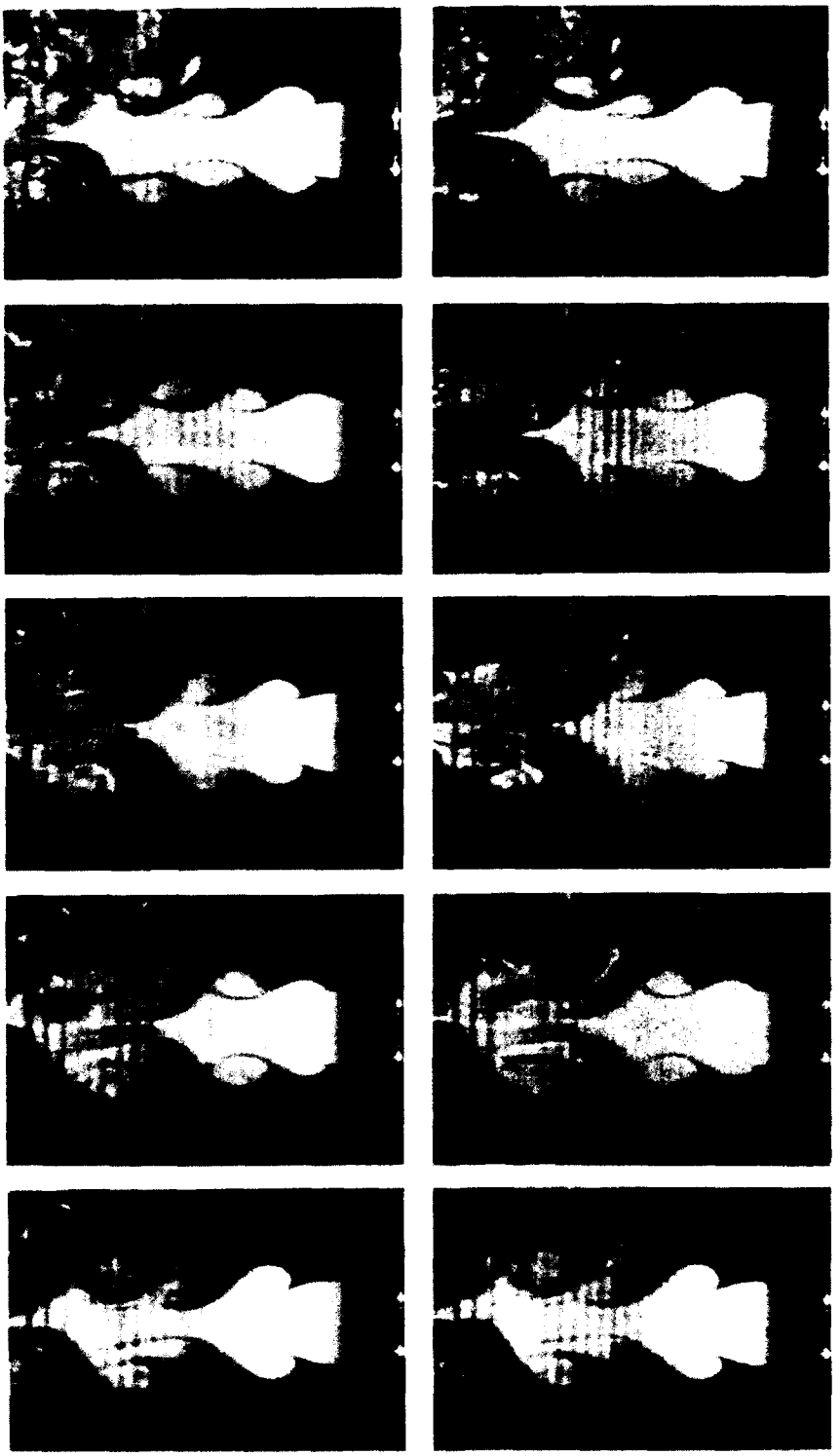

FIGURE 6. Successive movie frames showing the aerosol distribution in an axial plane of a seeded flow. $S = 0.29$; $D/\theta = 50$; $Re = 3025$; $D = 13.3$ mm. The sequence proceeds from left to right and from top to bottom. Framing rate $= \frac{2}{3}f_0$. The horizontal bands in the photographs are artifacts of using the multipass cell (see figure 3).

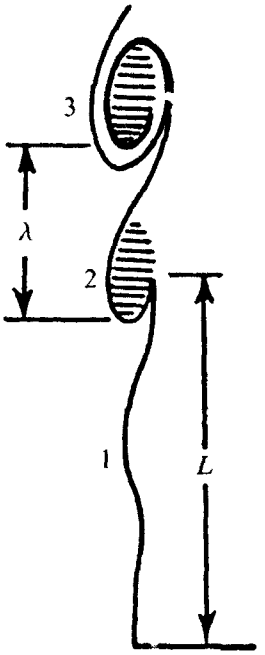

FIGURE 7. Typical pattern of disturbance evolution (after Becker & Massaro 1968).

table 1, where the data have been non-dimensionalized using θ. Each entry represents the average data on 100 successive vortices.

For flows which do not support the oscillating mode, λ/θ values shown in table 1 vary about a mean of 35.7 with a standard deviation of about 2.3. This variation appears random, hence λ/θ appears to be essentially independent of D/θ and S in the ranges considered. We note that the inviscid linear theory of Michalke (1971) indicates that, at $D/\theta \approx 69$, the most spatially amplified mode for $S = 1.0$ has a wavelength $\lambda/\theta \approx 33$. Furthermore, the analysis indicates that λ/θ is only weakly dependent upon D/θ and S; for example the most spatially amplified mode at $D/\theta \approx 69$ for $S = 0.50$ has wavelength $\lambda/\theta \approx 34$. These theoretical results are in good quantitative agreement with the data shown in table 1 for jets which do not sustain the oscillating mode.

For flows which do support the oscillating mode, λ/θ differs significantly from the values just discussed. At $D/\theta = 69$, S is reduced from 0.48 to 0.29, which encompasses the boundary for the onset of the oscillating mode, and λ/θ increases from 35 to 44. This suggests that the characteristics of the oscillating mode differ from other shear-layer modes. Measurements of the passage frequency presented in § 5 will show that this is indeed the case.

The L/θ values presented in table 1 show a marked distinction between the range of wave-breaking lengths in flows which sustain the oscillating mode and those which do not. For $D/\theta = 50$ and 60, reductions in S also correspond with reductions in L/θ (by 57% and 48%, respectively). The implication is that the instability waves break much closer to the nozzle in the presence of the oscillating mode. Physical intuition suggests that the wave-breaking length depends upon both the streamwise amplification rate of the instability waves as well as their 'initial' intensity. In § 5 it will be shown that the intensity of the oscillating mode is indeed closely associated with its large initial value.

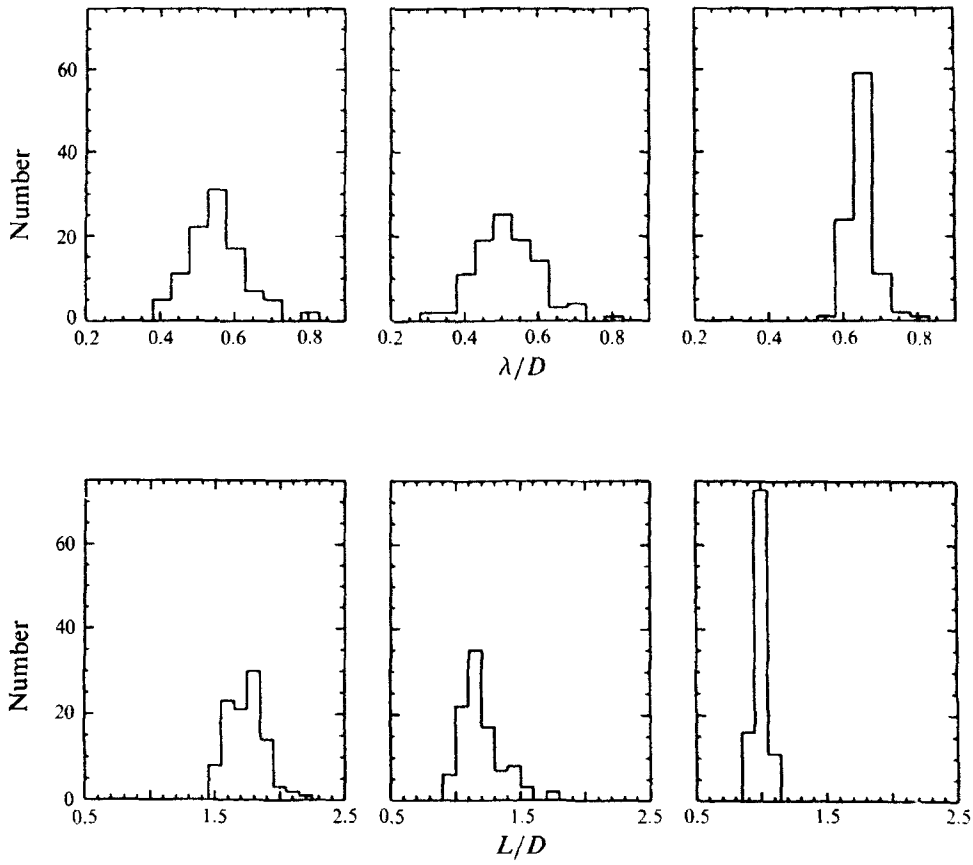

FIGURE 8. Histograms of wavelength λ/D and wave-breaking length L/D for various S: $D/\theta = 69$; $Re = 5500$; $D = 13.3$ mm; sample size = 100. From top left to bottom right: $S = 0.66$, $\sigma = 0.08$ (σ here is the standard deviation for the histogram); $S = 0.48$, $\sigma = 0.09$; $S = 0.29$, $\sigma = 0.04$; $S = 0.66$, $\sigma = 0.14$; $S = 0.48$, $\sigma = 0.16$; $S = 0.29$, $\sigma = 0.05$.

4.3. *Orderliness in kinematics*

Figure 8 shows histograms of λ/D and L/D for three different values of S, for $D/\theta \approx 69$. The standard deviation, σ, characterizing the uncertainty in the measurement of any single passing structure was estimated to be $\pm\frac{1}{20}D$. It is seen that σ for the wavelength data is roughly twice for $S = 0.66$ and 0.48 than that for $S = 0.29$. Recall from table 1 that at $D/\theta \approx 69$, the oscillating mode dominates the transition region for $S = 0.29$, and is absent at $S = 0.66$ and 0.48. The standard deviation for the wave-breaking length is roughly three times larger for $S = 0.66$ and 0.48 than that for $S = 0.29$. These results indicate that, for flows dominated by the oscillating mode, unusual regularity exists in the wavelength and in the location where the wave-braking process begins.

In figure 9, the locations of twelve successive eddies are followed from frame to frame for $S = 0.66$ and $S = 0.29$, with $D/\theta \approx 69$. The trajectory of each individual eddy is plotted from the wave-breaking point to the point where coalescence begins (see figure 6). Once individual vortices begin to wrap around their neighbours, their location can no longer be tracked. Focusing first on $S = 0.66$, it is seen from the first point of each trajectory that wave breaking occurs randomly in time (location along the abscissa) as well as in space (location along the ordinate). This result is expected

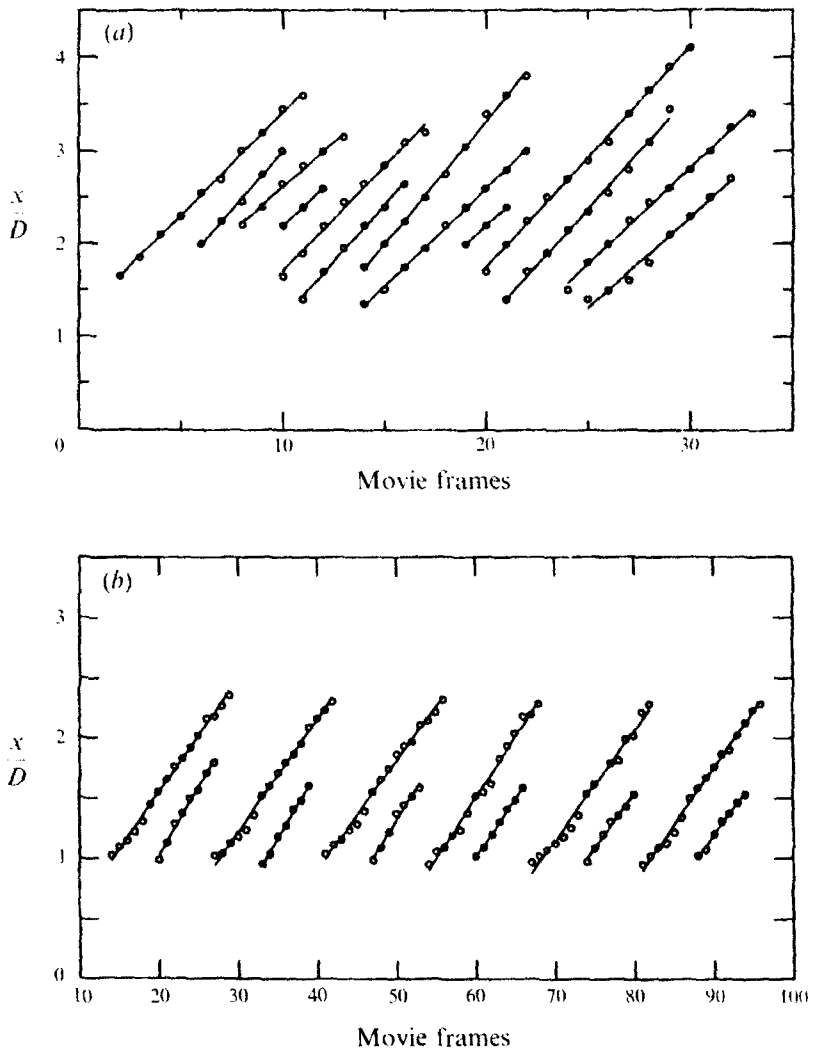

FIGURE 9. Eddy trajectories: $D/\theta = 69$; $Re = 5500$; $D = 13.3$ mm. Each trajectory begins where the wave 'breaks' and ends at the start of the coalescence process. Straight lines are least-squares fits. (*a*) $S = 0.66$. (*b*) $S = 0.29$.

from the histogram of L shown in figure 8 for the same conditions. From the final point of each trajectory it is seen that the coalescence process also exhibits significant random variation. For $S = 0.29$, however, both the roll-up and the coalescence are quite regular (see also figure 8). Such regularity is exhibited in all of the jets which support the oscillating mode. From the combined facts that pairing induces complete pinching off of potential core fluid, and that this process occurs with extreme regularity, one might expect that an axial profile of the time-averaged nozzle fluid concentration should exhibit a very sharp drop in the region where this process occurs. This is in fact the case (see also Chriss 1968; Tombach 1969).

Notice that the framing rate in the films was adjusted to be such that the duration for ten frames coincided with the subharmonic. This orderliness seen in figure 6 shows that the entire flow field approximately repeats itself after every subharmonic period.

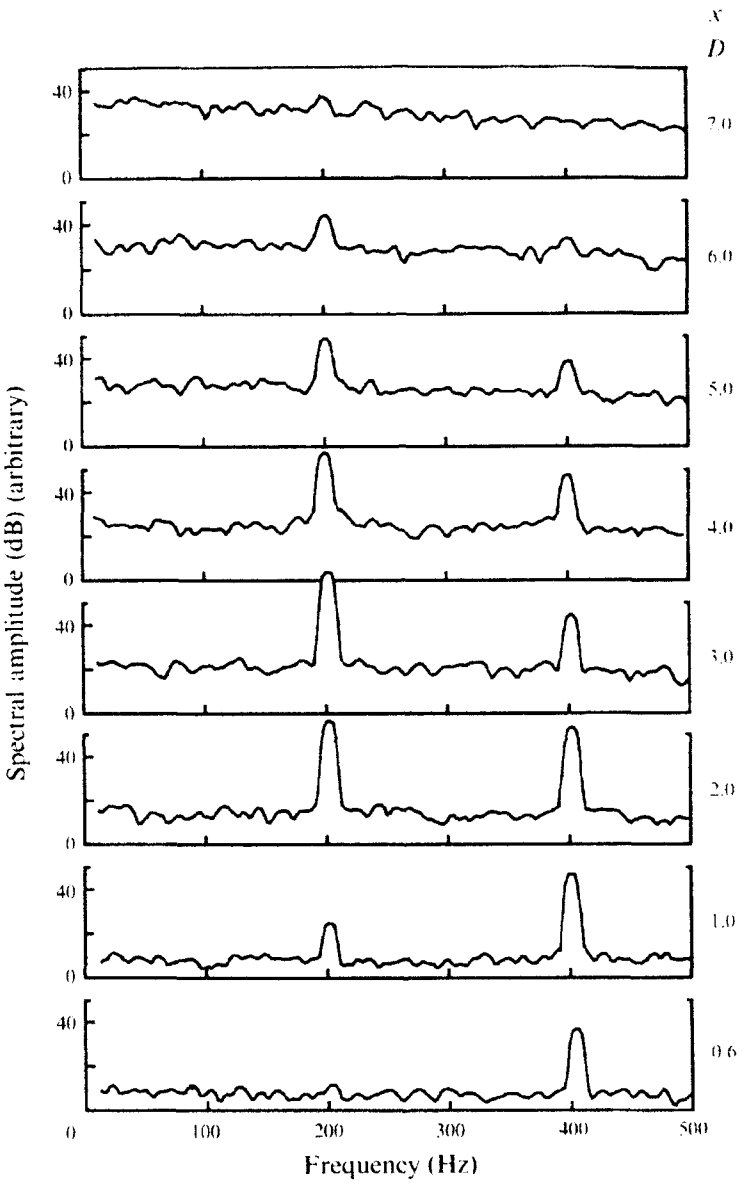

FIGURE 10. Power spectra of u' at various axial locations: $S = 0.29$; $D/\theta = 50$; $Re = 3025$; $D = 13.3$ mm. The corresponding x/D are marked on the curves. Spectra are calculated from time traces obtained using LDV.

4.4. *Centreline velocity*

The longitudinal component of velocity has been measured at various streamwise locations along the centreline using the LDV set-up mentioned in §2. Possible effects of seeding on the flow were investigated by monitoring the change in the frequency of the oscillating mode. The frequency as measured by a hot wire outside the shear layer never differed from the seeded case by more than 2%. A data rate of 10000 s^{-1} allowed us to construct a reasonable time trace, from which the spectra shown in figure 10 were calculated for $S = 0.29$ and $D/\theta = 50$. In figure 11, the spectral intensities of the

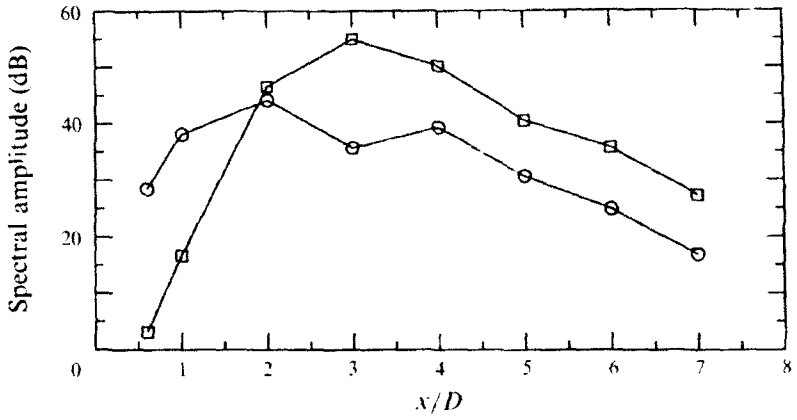

FIGURE 11. Spectral amplitudes for the fundamental and the subharmonic seen in figure 10: ○, fundamental; □, subharmonic.

primary and subharmonic modes are shown explicitly as functions of x/D. Notice that the ordinate in figure 10 is compressed and the abscissa is expanded (say, relative to figure 1) so that the spikiness of the spectral peaks is not apparent at a cursory glance.

It is useful to correlate the spectral intensities in figures 10 and 11 with the motion of the flow structures. At $x/D = 0.6$, the power spectrum exhibits a single peak. The frequency of this mode corresponds with the average local passage frequency of the initial axisymmetric wave. This is the fundamental mode, which continues to grow in intensity along the centreline even as the waves seen in the films break and roll up. The subharmonic appears in the spectra at around $x/D = 1$, and attains its maximum intensity along the centreline at $x/D = 3$. It is seen in the films that this maximum occurs at a location where fluid along the centreline is rapidly accelerated during the pinching off process, which, of course, occurs once every subharmonic period. Beyond $x/D = 3$ all discrete modes in figures 10 and 11 continually decay in the streamwise direction until, at $x/D = 7$, the subharmonic is barely discernable above the background. Correspondingly, the remnant of the pairing process appears in the film to become more diffuse as it travels downstream of $x/D = 3$.

Figure 12 shows the centreline profiles of the root-mean-square (r.m.s.) velocity u'/U_c and the mean velocity U/U_c for $S = 1.0$ and 0.29, and for $D/\theta \approx 50$. For reference, note that these are the same conditions as for figures 6, 10 and 11. The centreline turbulence intensity for $S = 0.29$ attains much larger amplitude compared with the air jet ($S = 1$). To our knowledge, such large intensities of the order 0.3 do not occur in an unforced constant-density jet. The peak u'/U_c value occurs at $x/D = 3.0$, which also corresponds with the peak in the subharmonic mode (figure 11). Thus, the abnormally large velocity fluctuation found in this jet is primarily associated with the vortex pairing process. U/U_c is seen to fall off rapidly starting from a diameter or so from the nozzle. On the other hand, we have already mentioned in §4.3 that the density of the gas along the centreline is approximately uniform until the pinching off starts at about $x/D = 2.5$. In the region $1.0 \leqslant x/D \leqslant 2.5$ slow, dense ambient air is being engulfed by the roll-up process, but this mixing does not penetrate to the centreline. The attenuation of U/U_c therefore implies the existence of an adverse streamwise pressure gradient.

In summary, the breakdown of the highly organized motion near the nozzle occurs in a qualitatively similar manner in all jets with $50 \leqslant D/\theta \leqslant 100$ and $0.6 \leqslant S \leqslant 0.14$, and is characterized by the growth of axisymmetric instability waves in the initially

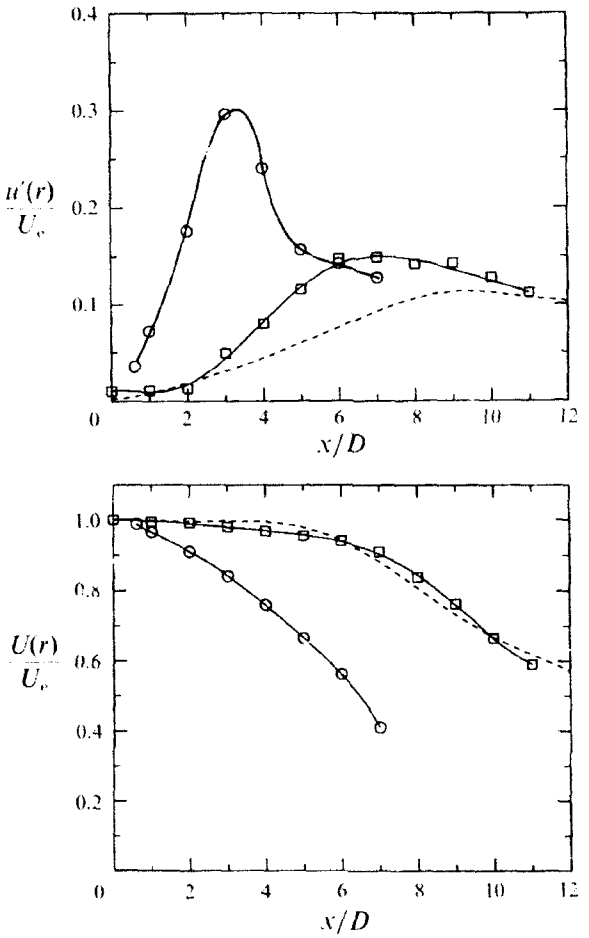

FIGURE 12. Streamwise component of the root-mean-square and the mean velocity as a function of x/D: ○, $S = 0.29$; □, $S = 1.0$; $D/\theta = 50$; $Re \approx 3025$; $D = 13.3$ mm. – – –, Corrsin & Uberoi (1949).

laminar shear layer; they pair and pinch off the potential core. The unique features of the oscillating mode are the following: (i) their wavelengths are not well predicted by linear stability theory (§4.2); (ii) waves break very close to the nozzle (§4.2); (iii) at each point in the near field, the flow is highly organized around the subharmonic period (§4.3); and (iv) fluctuations are intense and interact strongly with the mean flow field (§4.4)

5. The dynamical aspects of the near field

In this section, properties of the oscillating mode are studied at short downstream distances $x/\theta \leqslant 75$. We make use of power spectral density curves obtained from a hot wire located outside the shear layer, where these curves are representative of the power spectrum for the streamwise velocity inside the shear layer (see Appendix). These near-field measurements will be used in §§5.1, 5.2 and 5.3 for the purpose of studying the evolution of the oscillating mode with respect to the global parameters Re, D/θ and S. When cast in dimensionless form, this behaviour may be meaningfully compared with the theory of absolute instability.

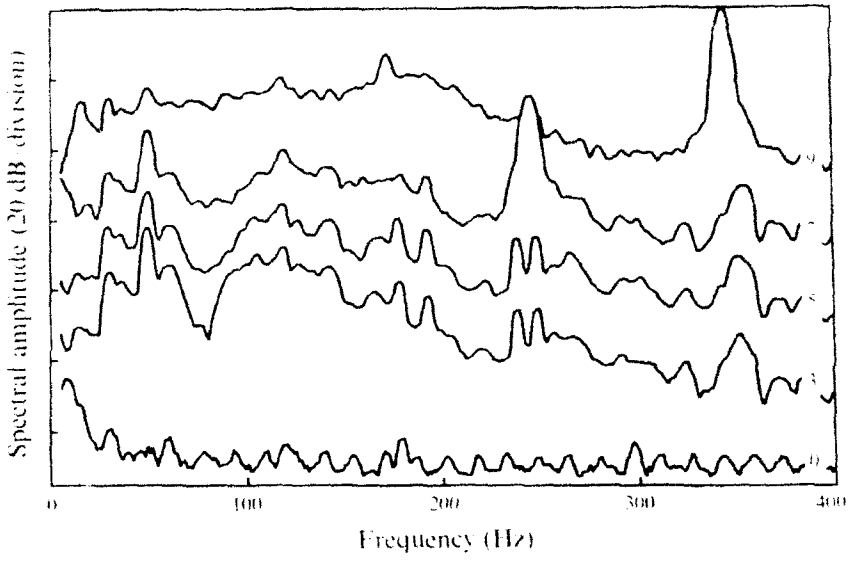

FIGURE 13. Power spectra of u' at various jet velocities U_j; $S = 0.29$; $x/D = 0.10$. Spectra are labelled with U_j in ms^{-1}. The arbitrary reference for the dB scale varies from curve to curve.

5.1. *Modal variations with S fixed*

We emphasize that in quantitative studies reported in this paper, one parameter at a time was varied keeping others fixed. The first section is meant to illustrate the qualitative changes which occur in the power spectrum by steadily varying the jet velocity while holding the nozzle gas density constant.

Figure 13 depicts these qualitative changes for $S = 0.29$ as the exit velocity is varied from 3.0 to 9.0 m/s. Note that the spectral distributions corresponding to 3.0 and 5.0 m/s are similar in that their peaks occur at identical frequencies. This frequency invariance was also exhibited in power spectra of u' obtained by Cohen & Wygnanski (1987) inside the shear layer at $x/D \approx 0$ for air jets. They suggested that the (relatively weak) spectral peaks could be attributed to the acoustic resonance properties of the upstream plenum chamber, which are of course dependent only upon the cavity geometry and the sound speed (see also Crow & Champagne 1971). The same conclusion had been reached by Hussain & Ramjee (1976) when they found that neither the shape of the nozzle contour nor variations in D/θ had any effect on the frequency of several spectral spikes both upstream and downstream of the nozzle contraction. These observations imply that the distribution of spectral peaks obtained in the near field of heterogeneous jets – with uniform gas composition upstream of the nozzle – should likewise be independent of the jet velocity, as indeed evidenced in figure 13. We also note that the frequency of fluctuations that are excited by the ubiquitous ambient acoustic signals will be independent of the velocity and density.

When U_j is increased from 5.0 to 7.0 m/s, however, a distinct spectral peak emerges above the background spectral distribution of u'. This is the oscillating mode which, near to its onset, does not appear to influence the intensity of modes at neighbouring frequencies. Such interaction does appear only when the oscillating mode has grown more intense (as in the uppermost spectrum in figure 13 corresponding to $U_j =$ 9.0 m/s). As suggested by figure 13, we have consistently found that the spectral intensity of the oscillating mode increases rapidly and continuously with U_j near its onset, when measured at any fixed location (see also Monkewitz *et al.* 1990). The

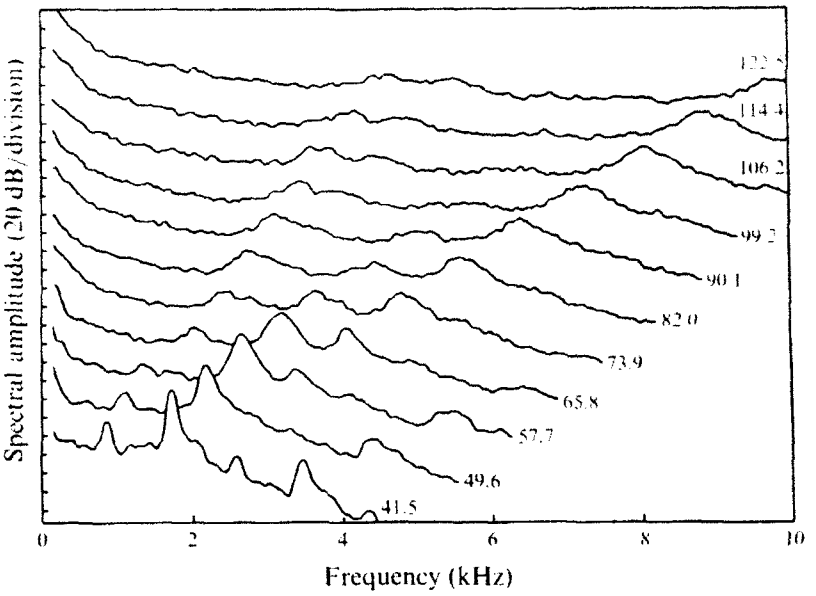

FIGURE 14. Power spectra of streamwise velocity fluctuations u' within the shear layer: $S = 0.14$; $x/D = 0.10$. Spectra are labelled with U_e in ms^{-1}. The arbitrary reference for the dB scale varies from curve to curve.

frequency of the oscillating mode increases monotonically with U_e. Note that because the oscillating mode alone is velocity dependent very near the nozzle, it can be readily distinguished from the background disturbance peaks near to its onset.

Figure 14 shows qualitative changes that occur in the spectral distribution of shear layer disturbances as the velocity is increased above values for which the oscillating mode has already achieved a relatively large intensity. In the spectrum corresponding to $U_e = 41.5$ m/s (at the bottom of figure 14), the tallest peak at $f = 1733$ Hz is the fundamental of the oscillating mode. Its subharmonic and several higher harmonics are also evident. Between $U_e = 49.6$ m/s and 65.8 m/s (second and fourth spectra from the bottom) the velocity evolves from a stable periodic state to one dominated by disturbances with relatively broadband spectral content. Note that although the pure periodicity is lost, these relatively broadband disturbances are still to be regarded as the oscillating mode, simply because the frequency and intensity change smoothly with U_e. This transition has been discussed by Kyle & Sreenivasan (1988, 1989) and Monkewitz *et al.* (1990). In this same velocity range, the subharmonic of the oscillating mode diminishes in intensity at this streamwise location and finally vanishes. As the velocity increases above 65.8 m/s (fourth spectrum from the bottom), the oscillating mode diminishes in amplitude and finally disappears.

At about 57.7 m/s (third spectrum from the bottom) two other broadband modes emerge with frequencies which differ by approximately a factor of two. Their frequencies are apparently not related to that of the oscillating mode. As the velocity increases above 57.7 m/s, these modes intensify. It may be thought that compressibility affects the disappearance of the oscillating mode or the emergence of these other broadband modes, since $M^2 = 0.126$ for the uppermost spectral density. However, this is almost certainly not so because they occur at $M^2 = O(10^{-2})$ for $S = 0.29$ and $M^2 = O(10^{-3})$ for $S = 0.48$ (see §5.2). The possibility of Mach-number dependence will therefore not be further mentioned.

Our measurements were made over a six-year period using several settling chamber configurations, four nozzles with differing contraction contours and relate to the following parameter ranges: $0.14 \leqslant S \leqslant 1.0$; $40 \leqslant D/\theta \leqslant 125$; $800 \leqslant Re < 15000$. On the basis of data obtained from films (§4), centreline LDV measurements (§4) and near field hot-wire measurements described in this section so far, we conclude that the only modes that are sustained in our facility, which are unique to helium/air jets, are: (i) the oscillating mode, along with its subharmonic and higher harmonics, and (ii) the broadband modes evidenced in figure 14 at higher values of D/θ and Re.

Monkewitz *et al.* (1990) have reported that the heated air jet will support two distinct oscillatory instabilities having unrelated frequencies, which they call 'Mode I' and 'Mode II'. The bulk of their observations pertain to 'Mode II'. We note that kinematic features of their 'Mode II' are similar to those of the oscillating mode. In spite of the existing uncertainty about the parameters governing these instabilities, there appears to be good agreement between the S range for 'Mode II' ($S \leqslant 0.62$) and for the oscillating mode ($S \leqslant 0.61$), as well as between the $St_D = fD/U_c$ values for the two modes (≈ 0.45). The oscillating mode, like 'Mode II', was determined by experiment to be axisymmetric. From these comparisons, and others to be developed further in §§5.2, 5.3, it is reasonable to suppose that 'Mode II' supported in heated jets and the oscillating mode in He/air jets are essentially the same.

Little is known about the physical nature of these broadband modes; for example, we have not determined their azimuthal dependence. It is not known whether they occur in heated air jets, because Monkewitz *et al.* did not examine U_c beyond where 'Mode II' (the oscillating mode) began to broaden, whereas it is precisely at these U_c values that the broadband modes first appear in He/air jets (figure 14). As to the possible correspondence of these modes with 'Mode I' of Monkewitz *et al.*, it should be noted that 'Mode I' is very 'spiky' whereas the broadband modes, by definition, are not. Furthermore, at any given S, 'Mode I' occurred in the facility of Monkewitz *et al.* at only the small U_c values (small D/θ and Re), whereas the broadband modes were observed in our facility only at high speeds (large D/θ and Re). We tentatively conclude that the 'Mode I' instability does not occur in helium/air jets.

5.2. *D/θ dependence of the frequency of the oscillating mode*

The principle of dynamic similarity assures us that when fluctuation frequencies are expressed in non-dimensional form, their values must depend only upon D/θ, Re and upon background disturbances, if S is fixed. For the case of fixed nozzle gas composition these parameters cannot be varied separately using a single nozzle. In order to examine whether the Strouhal number $St_D = fD/U_c$ is a function of either D/θ or Re alone, data obtained in both the ASME nozzle and in the cubic equation nozzle are plotted together in figure 15. It is assumed that difference in the exterior geometry of the nozzle lips are not significant enough to affect the results. St_D values for the two jets are quite disparate when plotted as a function of Re (figure 15*a*), where they match well when plotted as a function of D/θ (figure 15*b*). Re values in each jet differ by approximately a factor of 2.3 at each D/θ over the range of interest; the maximum initial shear-layer disturbance levels (u'/U_c) for fixed D/θ values differ in the two nozzles by a factor of about 2.2. It follows that, to within experimental error, non-dimensional frequencies for the oscillating mode – as well as for other modes sustained at large D/θ – are dependent upon D/θ alone over the parameter range of interest, and that the Reynolds number is felt only indirectly through its influence on D/θ. Subbarao (1987) studied an oscillating mode in buoyant helium jets ($0.08 \leqslant Ri \leqslant 0.79$) having fully-developed parabolic velocity profiles at the nozzle exit ($D/\theta = 15$), and found that

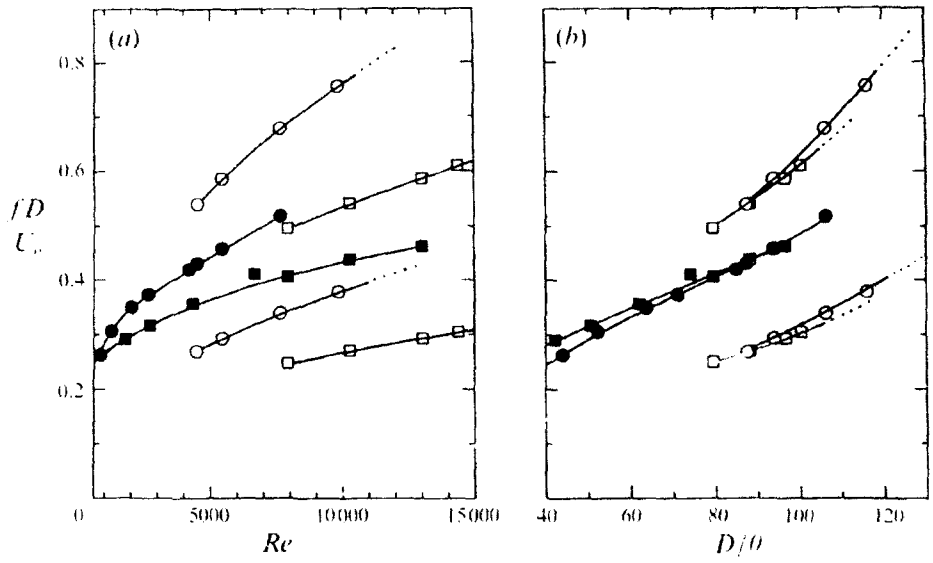

FIGURE 15. Non-dimensional frequency fD/U_∞ plotted separately as a function of D/θ and as a function of Re: ○, $D = 9.3$ mm; □, $D = 13.3$ mm. $S = 0.14$; $x/D = 0.10$. Solid symbols represent the oscillating mode; open symbols represent the other broadband modes prevalent in the near-field measurements (see figure 14).

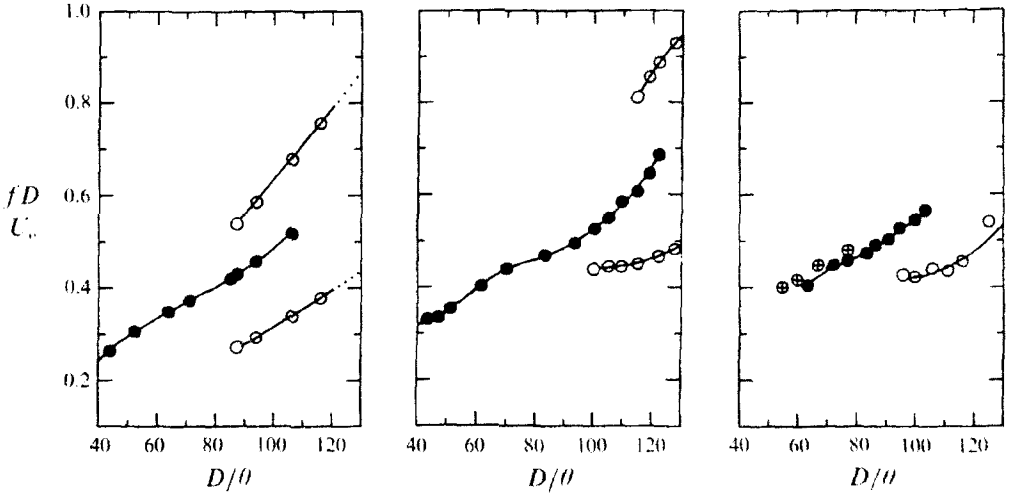

FIGURE 16. Non-dimensional frequency fD/U_∞ as a function of D/θ for various values of S: $x/D = 0.10$; from left to right $S = 0.14$, 0.29 and 0.48 respectively. ●, oscillating mode from present experiments; ○, additional prominent disturbance modes in present facility; ⊕, oscillating mode (Mode II) in the heated air jet (Monkewitz *et al.* 1990).

St_D was independent of Re ($1500 \leqslant Re \leqslant 12500$). However, it is unclear how relevant his results are to the current ones, as the parameter ranges for the two studies are different.

In figure 16, the non-dimensional fluctuation frequencies shown in figure 15 for $S = 0.14$ are replotted along with similar data obtained for $S = 0.29$ and $S = 0.48$. It is seen that as S changes, the functional relation between the near-field stability characteristics and D/θ also changes. The lower onset value of D/θ for the oscillating mode is about 40 for $S = 0.29$ and about 60 for $S = 0.48$, whereas for $S = 0.14$ it

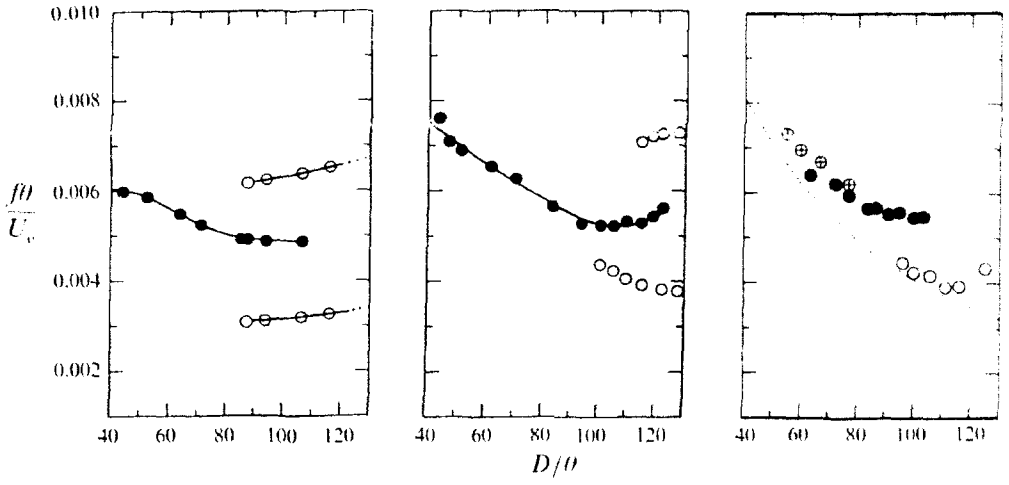

FIGURE 17. Non-dimensional frequency $f\theta/U_c$ as a function of D/θ: $x/D = 0.10$; ●, oscillating mode from present experiments; from left to right $S = 0.14$, 0.29 and 0.48 respectively. ○, additional prominent modes in present facility; ⊕, oscillating mode in the heated air jet (Monkewitz *et al.* 1990); ------, theory (Monkewitz & Sohn 1988).

extends below 40, and could not be ascertained. A qualitative feature common to all three density ratios is that the oscillating mode vanishes when D/θ becomes large enough. At least one of these new modes always persists beyond the D/θ bounds for this study. Experimental data obtained by Monkewitz *et al.* (1990) in a heated air jet with $S = 0.47$ are plotted along with helium/air jet data for $S = 0.48$. D/θ ratios were calculated assuming the vorticity thickness $\delta_\omega \approx 5\theta$ for the initial velocity profile in the heated air jet of Monkewitz *et al.* (1990). It is seen that the comparison is very good indeed, even though at each D/θ, Re differs by roughly a factor of 2 and the two flows are not strictly analogous. This confirms the correspondence between 'Mode II' in heated jets and the oscillating mode in helium/air jets.

The broadband modes that appear when D/θ reaches large values – one or two, depending on the density ratio – do not correspond to 'Mode I' of heated air jets in terms of the frequency range ($0.25 \leqslant St_D \leqslant 0.3$) as well as density ratio ($0.55 \leqslant S \leqslant 0.69$).

The frequency data shown in figure 16 have been non-dimensionalized using the momentum thickness as the lengthscale, and the resulting $St_\theta = f\theta/U_c$ values are plotted in figure 17. It is clear that f scales neither on D nor on θ within the D/θ range covered. In order to find out whether f scales 'more closely' on θ or D, we have evaluated $\Delta(St_D)/(St_D)_{max}$ for each of the curves in figure 16, where $\Delta(St_D)$ is the range in any one curve and $(St_D)_{max}$ is the maximum value in the same curve, and compared these ratios with $\Delta(St_\theta)/(St_\theta)_{max}$ calculated from figure 17. At each S, the ratio for St_θ is approximately half as large as for St_D. Further, much of the variation in St_D occurs for D/θ values above 80 (figure 16), whereas St_θ variations are small in this region (figure 17). This suggests that as the shear-layer thickness becomes small relative to the diameter, the shear-layer thickness tends to play a more dominant role in establishing the frequency of the oscillating mode. The relative invariance of St_θ was not observed in our previous study (Kyle & Sreenivasan 1989) because of the limited D/θ range considered.

Another important feature emerges from figure 17. The frequency of the stationary mode, $\omega_r(k^*(0))$, as calculated by Monkewitz & Sohn (1988), is compared with the

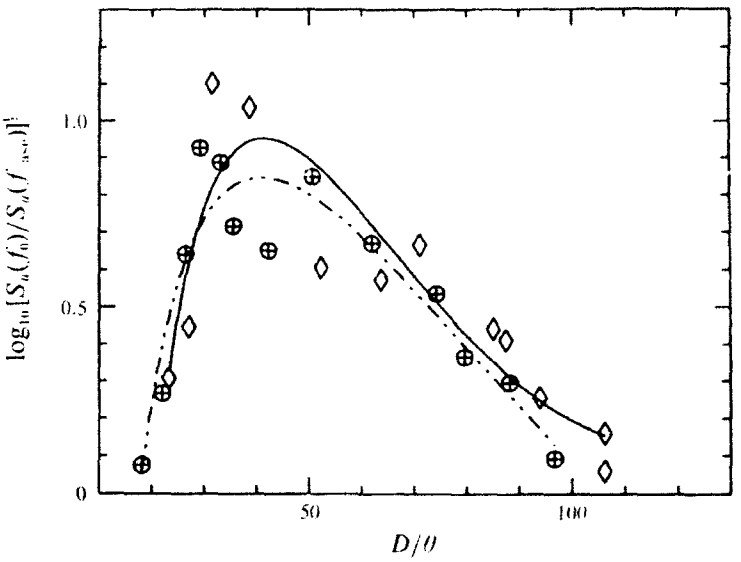

FIGURE 18. Near-field base-to-peak intensity as a function of D/θ: ◇, $D = 13.3$ mm; ⊕, $D = 9.3$ mm. $S = 0.14$; $x/D = 0.10$. Corresponding Reynolds numbers are shown in figure 15. (See text for definitions.)

experimental data for $S = 0.48$. The correspondence seems reasonably good for smaller D/θ, but degrades as D/θ is increased. The Strouhal number of the broadband modes also agrees with the theory for a range of D/θ. The spatial theory predicts that the most unstable mode for $S = 0.5$ should have $0.0125 \leqslant St_n \leqslant 0.013$ for this range of D/θ (Michalke 1984), which is clearly a poor prediction.

5.3. *The intensity of the oscillating mode*

We turn our attention to the intensity of the oscillating mode. Specifically, we are interested in choosing a non-dimensional measure of intensity which will reflect the transition that the oscillating mode undergoes from a pure periodic disturbance to one with a relatively broadband spectral content (see figure 14). One possible measure is the ratio of the maximum intensity on the spectral peak, located at f_0, to the intensity at the base of the peak. The 'base' is arbitrarily chosen to be wherever the width of the spectral peak, measured in Hertz, is equal to $\frac{1}{10}f_0$. Thus, letting $S_u(f)$ denote the power spectral density of u' at frequency f, we define the base-to-peak intensity as $[S_u(f_0)/S_u(f_{base})]^{\frac{1}{2}}$. This measure of base-to-peak intensity is generally greatest whenever velocity fluctuations associated with the oscillating mode are simultaneously intense relative to background disturbance, and distributed over a spectral bandwidth smaller than $\frac{1}{10}f_0$.

In figure 18, the near-field base-to-peak intensities for jets issuing from each of the nozzles are plotted as functions of D/θ for $S = 0.14$. The curves correspond to fourth-order polynomials fitted to the data. The curve for the ASME nozzle matches quite well the curve for the matched cubic nozzle. When the data are plotted as a function of Re, the two curves are relatively far apart (this result is not shown). Thus, given S, the near-field base-to-peak intensity is mainly dependent upon D/θ alone. We had formerly remarked (Sreenivasan *et al.* 1989) that the transition to an oscillatory state occurs abruptly with respect to changes in the governing parameters. This is illustrated by the rapid rise in base-to-peak intensity as D/θ increases from its lower limit (see also figure

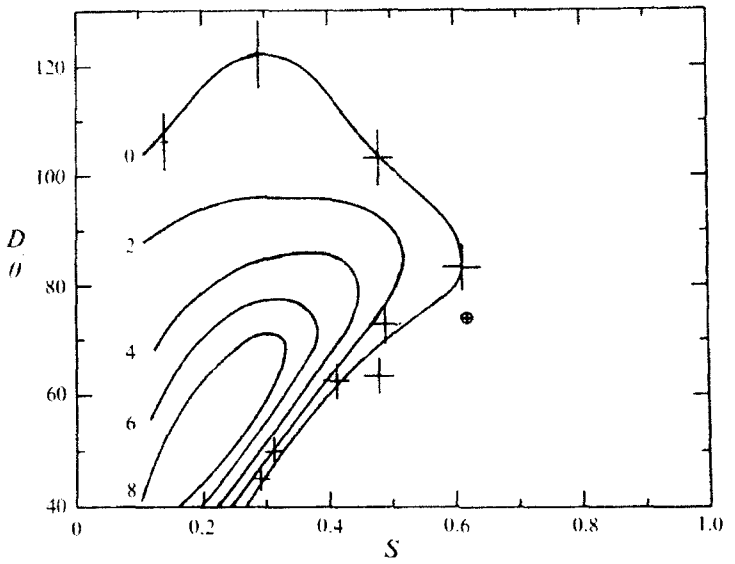

FIGURE 19. Near-field base-to-peak intensity as a function of D/θ and S: contours are labelled with base-to-peak intensity values. The inner contours correspond to larger and larger peak intensities. Error bars denote uncertainty in experimental determination of onset. ⊕, onset in heated air jets (Monkewitz *et al.* 1990).

13). As D/θ nears its upper limit, the base-to-peak intensity varies relatively slowly. This latter aspect is reflected in Sreenivasan *et al.* (1989) by the large error bars used by them.

In summary, we have shown that the non-dimensional frequency of the oscillating mode and its near-field base-to-peak intensity are definite functions of S and D/θ alone. Both these quantities vary significantly with D/θ and do not scale with either D or θ alone. An upper D/θ limit for the oscillating mode has been found for all $S \geqslant 0.14$. This limit is not influenced by either the Mach number or the Reynolds number. Indeed, figure 15 shows that the upper D/θ bound is nearly the same for both nozzles. A lower D/θ limit also exists (except perhaps for $S = 0.14$). Such limits are useful for assessing the accuracy of physical theories (see § 7) which predict 'critical values'. They are also important in the practical sense that they help establish the parameter region relevant to the appearance of the oscillating mode.

5.4. *The onset of the oscillatory state*

In this section we study changes in the flow which result from small changes in S near the onset value S_0 for the oscillating mode, for various fixed values of D/θ. Physically, this means that the normalized mean velocity profile at the exit is held fixed as the nozzle fluid density is changed by small increments.

Figure 19 shows the results of systematic measurements of the near-field base-to-peak intensity for the range of ordered pairs $(S, D/\theta)$ relevant to this study. To construct these contours, base-to-peak data were obtained for $S = 0.14$, 0.29, 0.48 and 0.60. At each S, curves were fitted to the data exactly as for figure 18. Data obtained from these curves were used to construct the contours in figure 19. Onset values were further explored by slowly decreasing S at fixed D/θ values of 83, 70, 60 and 50. Error bars are shown for onset values only. The outermost curve marked '0' is the locus of the onset value, S_0, for the oscillating mode and the corresponding D/θ. The region inside this curve (i.e. below and to the left) correspond to inlet flow conditions which

support the oscillating mode. Everywhere outside this curve, the oscillating mode is absent. The S_0, D/θ curve is useful for comparing the onset of the oscillating mode with the predicted onset – or 'critical' – values of S and D/θ associated with absolute instability. Over a range of D/θ values which includes $D/\theta = 83$, critical S values are predicted to lie between 0.66 and 0.72 (Monkewitz & Sohn 1988). Thus, in the vicinity of $D/\theta = 83$ ($S_0 = 0.61$), one might say that there is reasonable correspondence with the theory. On the other hand, consideration of S_0 over a wider range of D/θ values leads to a salient discrepancy: while figure 19 shows that for each $S \leqslant 0.61$ there is an upper bound on the D/θ values for which the oscillating mode can exist, the theory predicts that for all $S \leqslant 0.62$, $\omega_i(k^*(0)) > 0$ even in the limit of $D/\theta \to \infty$ (Monkewitz & Sohn 1986, 1988).

We are interested in the transition to a stable periodic state. Note that the contours in figure 19 are labelled by the base-to-peak intensity. By drawing horizontal cuts through these contours at different constant values of D/θ, one immediately sees that the transition to a stable periodic state brought about by decreasing S can occur in various ways, depending on the choice of D/θ. For example, at $D/\theta = 50$, a small decrease in S below $S_0 \approx 0.31$ is accompanied by a dramatic rise in base-to-peak intensity, whereas at $D/\theta = 83$ base-to-peak intensity varies slowly with S below $S_0 \approx 0.61$.

In order to quantify the effects of D/θ further, the square root of the power spectral density of u' at f_0, u'_{f_0}, is shown in figure 20 non-dimensionalized using U_e, for $D/\theta = 50$, 62.5, and 83. The data are plotted as functions of the normalized density difference $\Delta S = (S_0 - S)/S_0$. The spectra were measured using a hot wire located at $x = 10\theta$, and $r/D = 0.55$ for all three D/θ values. Shadowgraph images for each flow condition revealed no detectable helium present at these locations.

Figure 20 shows that the functional relation between u'_{f_0}/U_e and ΔS is different at different values of D/θ. The uncertainty in ΔS results primarily from the uncertainty in the empirically determined value of S_0. For small ΔS, the data in figure 20 may be fitted to power laws of the form:

$$\left.\begin{aligned} u'_{f_0}/U_e &= a(\Delta S)^n \quad (\Delta S > 0), \\ u'_{f_0}/U_e &= 0 \qquad\quad (\Delta S \leqslant 0), \end{aligned}\right\} \tag{5.1}$$

where the free parameters a and n are determined by the fitting algorithm. For $D/\theta = 50$, $a = 10^{1.5}$ and $n = 1.3$, while for $D/\theta = 62.5$, $a = 10^{1.0}$ and $n = 1.36$. For $D/\theta = 83$, the gradient changes snarply at $\Delta S \approx 0.15$, so that significant error occurs if the power law relation (5.1) is fitted to the data spanning the entire interval $0 \leqslant \Delta S \leqslant 0.76$. If the model (5.1) is applied only to points lying inside the interval $\Delta S \leqslant 0.15$, however, the power-law assumption seems suitable, with $a = 10^{-1.3}$ and $n = 0.55$. It should be mentioned that the measurements were repeated at two other radial locations with the results that the coefficient a becomes smaller for points further away from the jet (and is thus a function of position), but the exponent n was essentially independent of the probe position.

Monkewitz *et al.* (1990) measured the amplitude of near-field pressure fluctuations in a parameter region quite near to the latter truncated range (onset occurred at $D/\theta \approx 74$, $S = 0.62$). A power-law relation provided a good fit when they assumed the power-law exponent $n = 0.5$ for data spanning the interval $\Delta S \leqslant 0.26$. They further noted that Landau's weakly nonlinear stability theory (Landau & Lifshitz 1959) predicts the r.m.s. amplitude of a discrete temporal instability should lie on the parabola $u'^2 \propto \Delta S$ when ΔS is small. Figure 20 shows that, while Landau's theory may apply to the data at $D/\theta = 83$, it fails for $D/\theta = 50$ and 62.5.

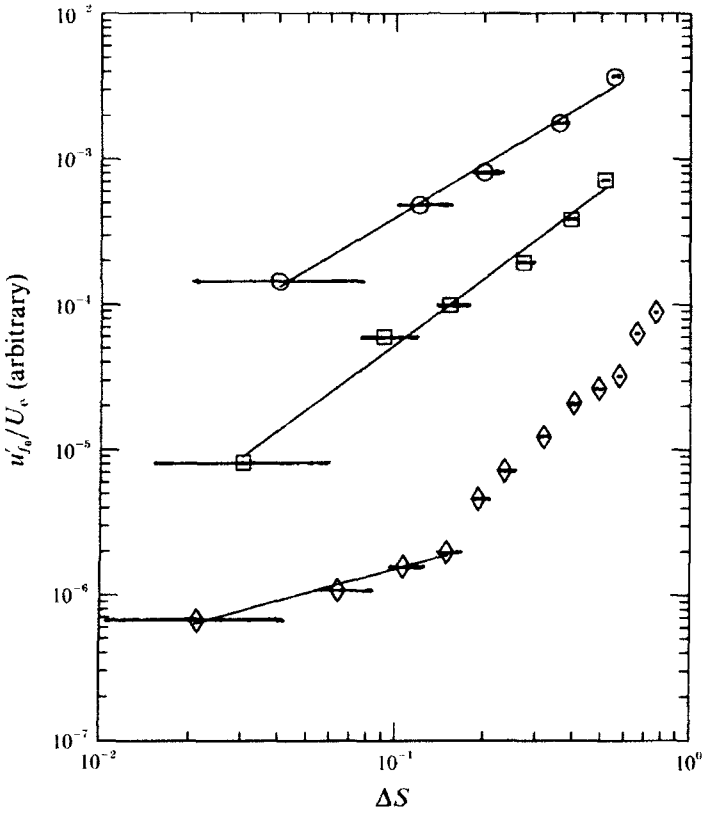

FIGURE 20. Square root of the power spectral density of u' at f_0, u'_{f_0}, normalized by U_e, and plotted as a function of $\Delta S = (S_0 - S)/S_0$ for various D/θ: The power spectrum was measured with respect to an arbitrary reference voltage which was constant for all of the measurements. ◇, $D/\theta = 83$; □, $D/\theta = 62.5$; ○, $D/\theta = 50$. $S = 0.14$; $r/D = 0.55$. The uncertainty in S_0 (see figure 19) is the primary source of uncertainty in ΔS.

This failure is not unexpected. Recall that Landau & Lifshitz (1959) derived the equation beginning with the factorization

$$u'_{f_0}/U_e = A(t; S_0 - S)\boldsymbol{f}(\boldsymbol{x}), \tag{5.2}$$

which assumes that the spatial eigenfunction $\boldsymbol{f}$ is independent of the control parameter S near the critical value S_0. The data of figure 12 (see §4.4) suggest that Landau's assumption concerning $\boldsymbol{f}(\boldsymbol{x})$ near onset does not apply, say, at $D/\theta = 50$. The large intensities shown in figure 12 for $S = 0.29$ correspond with $\Delta S \approx 0.07$, which may be considered small. Even so, the velocity profiles shown in figure 12 imply that the mean flow divergence is profoundly altered by the onset of the oscillating mode. Recall further from table 1 (§4.2) that for $D/\theta = 50$ and 60, small reductions in S correspond with relatively large reductions in the wave-breaking length. These results suggest that the mean flow in the transition region can be significantly affected by the onset of the oscillating mode, especially at D/θ of the order 50. Figure 20 shows that near onset, the near-field spectral intensity and its gradient are largest at just these D/θ values. One may therefore conclude that for D/θ values of the order 50, the rapid increase in near-field disturbance intensity close to the onset can lead to significant variations in the mean flow structure. If the spatial distribution of fluctuation intensity is related to the structure of the mean flow, it follow that (5.2) should not hold for these D/θ values.

Although there is considerable variation in the character of the onset of the

oscillating mode, one may interpret the occurrence of a stable periodic state in homogeneous round jets as a 'bifurcation' of a nonlinear system from an equilibrium state. Although there are obvious problems with this interpretation, such as defining the equilibrium state, the bifurcation is a supercritical one for flow conditions pertaining to this study. This result is in contrast with the findings of Sreenivasan *et al.* (1989) for a small range of parameters; they used a 4.0 mm nozzle and found that the oscillating mode was *conditionally stable* i.e. that the transition to a stable periodic state should be modelled as a *subcritical bifurcation*. We believe that this difference in behaviour is due to changes in the mean velocity profiles at the nozzle exit; however, because of the small size of that nozzle, we could not measure the velocity profile.

5.5. *Streamwise evolution of the oscillating mode*

In §4, the growth and interaction of large-amplitude vortical structures were examined. We were able to distinguish kinematically between the waves associated with the oscillating mode and waves associated with shear-layer modes usually studied in homogeneous jets. In this section we aim to explore this distinction further by examining their streamwise dependence near the nozzle, where the disturbances are still small. We first establish a method for determining the most spatially amplified mode between any two streamwise locations in the air jet, and then extend it to study heterogeneous jets. For reasons that will be made clear later, this method is most instructive when the oscillating mode is relatively weak. Therefore most of the measurements are obtained at D/θ values near 83, for which it has been shown (see §4.2) that oscillation intensities are small.

Figure 21(*a*) shows power spectra for u' measured using a hot wire located in the shear layer of an air jet where $U/U_c = 0.60$ at streamwise locations $x/\theta = 50$, 100, 200 and 300; $D/\theta = 93$ for this flow. All four spectra are normalized by the maximum spectral amplitude at $x/\theta = 300$. It is evident that the mode at 670 Hz plays a dominant role in the evolution of the shear layer for these conditions. This mode is prominent at $x/\theta = 50$ and grows continually until it dominates the spectrum at $x/\theta = 200$. At $x/\theta = 300$ the subharmonic has become dominant.

We would like to characterize the growth of small disturbances in a region of the jet where nonlinear effects are small. With this intention we focus on the region $x/\theta \leqslant 100$. Figure 21(*b*) shows the ratio of spectral amplitudes at $x/\theta = 100$ to those at $x/\theta = 50$ at corresponding frequencies f. This function simply equals, at any given frequency, the spatial growth rate of disturbances integrated between $x/\theta = 50$ and $x/\theta = 100$. The mode that is most spatially amplified corresponds to the maximum value of this function.

Comparison of the total amplification function (figure 21*b*) with the spectra in figure 21(*a*) reveals that the most energetic mode at $x/\theta = 200$ (670 Hz) is not the most amplified mode in the near field (≈ 860 Hz). The spectra indicate that the mode at 670 Hz becomes dominant owing to the combined effects of its near-field prominence and its subsequent amplification. That the initial velocity-independent spectral distribution of u' could affect the frequency of the most energetic mode further downstream in the shear layer was shown by Cohen & Wygnanski (1987); see also Becker & Massaro (1967) and Gutmark & Ho (1983). The total amplification curve (figure 21*b*) allows one to distinguish between amplification, which varies relatively smoothly with frequency, from the influence of initial field, which varies randomly.

Similar information can be extracted from the total amplification function in heterogeneous jets, as long as the disturbances are sufficiently small. In figure 22, the amplification of shear-layer disturbances between $x/\theta = 25$ and 75 is shown as a

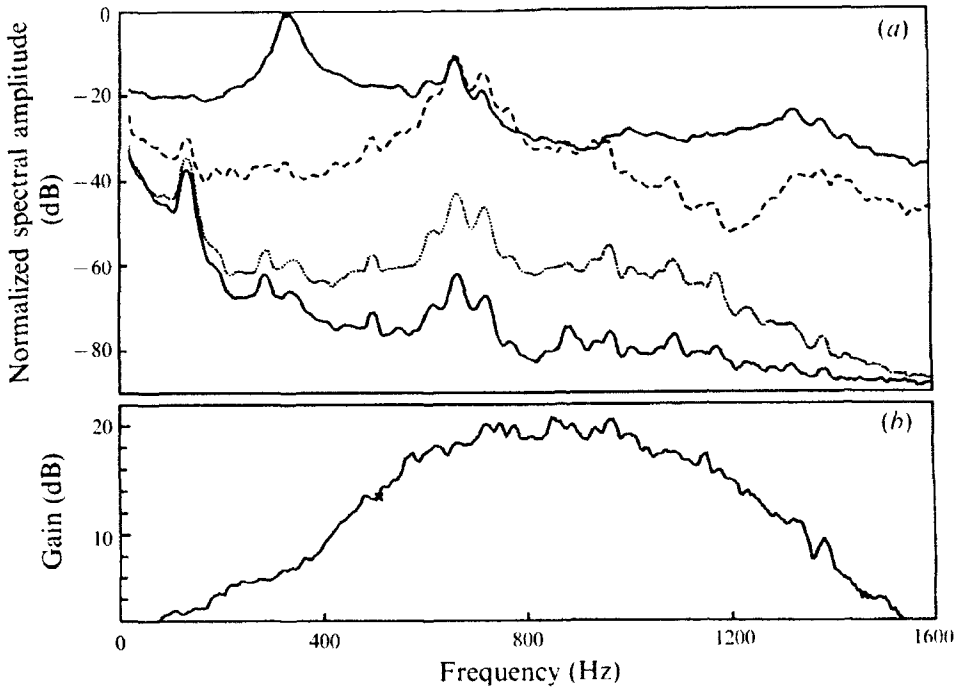

FIGURE 21. (*a*) Normalized power spectra of u' obtained in the shear layer of an air jet at various streamwise locations: ——, $x/\theta = 50$; · · · · ·, $x/\theta = 100$; – – – –, $x/\theta = 200$; — · —, $x/\theta = 300$. $S = 1.0$; $U/U_0 = 0.6$; $D/\theta = 93$. (*b*) Mode amplification between 50θ and 100θ as a function of frequency using spectra shown in (*a*).

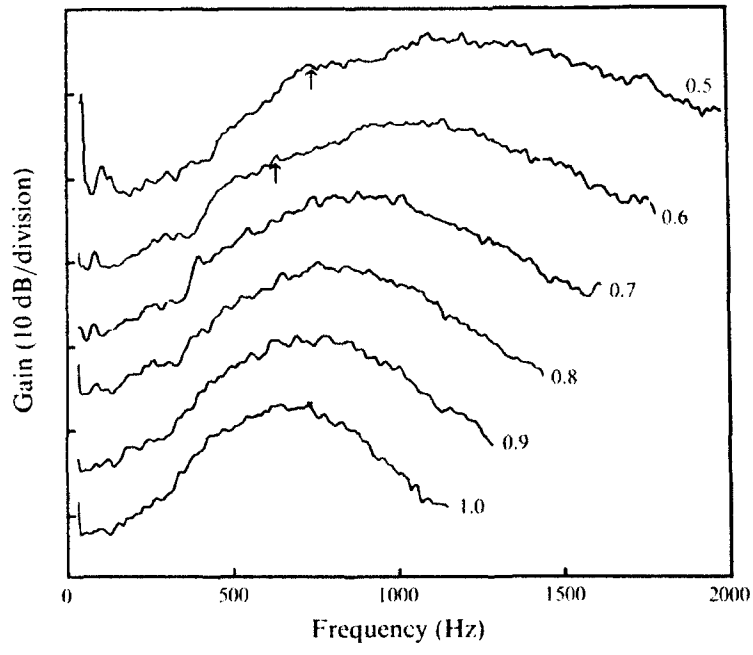

FIGURE 22. Mode amplification between $x/\theta = 25$ and $x/\theta = 75$ as a function of frequency for various values of S. Curves are labelled with S. The gain at each S is determined to within an arbitrary constant factor. Arrows indicate the frequency of the oscillating mode.

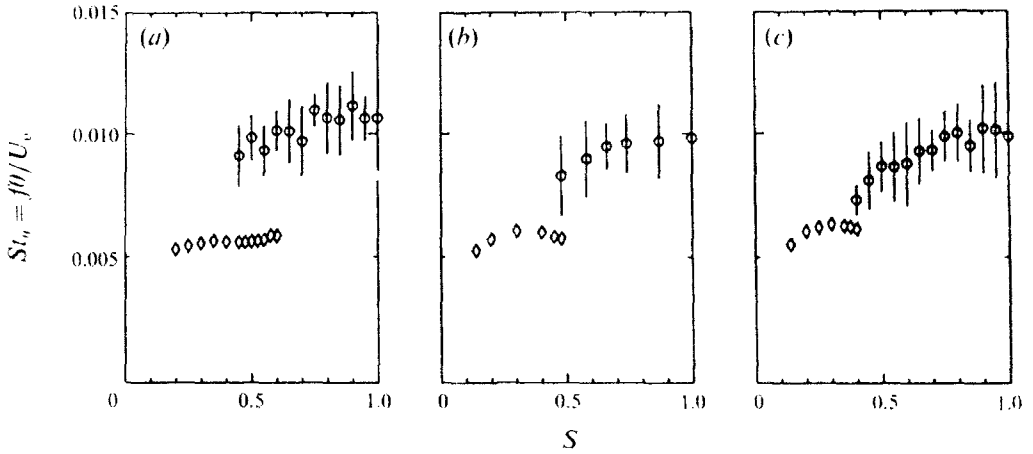

FIGURE 23. Non-dimensional frequency $f\theta/U_e$ plotted as a function of S for (*a*) $D/\theta = 83$; (*b*) $D/\theta = 73$; (*c*) $D/\theta = 62.5$. ◇, oscillating mode; ○, most amplified mode as measured between $x/\theta = 25$ and 75. Errors bars denote measurement uncertainty.

function of frequency for S values ranging from 1.0 to 0.50, for $D/\theta = 83$. (For reasons described in the Appendix, these curves are known only to within an undetermined constant.) Notice that the curves resemble one another in shape, and that the frequency of the most amplified mode varies smoothly with S. This continuity suggests that the underlying physical processes involved in the streamwise amplification of disturbances in homogeneous shear layers are not drastically different from those in the inhomogeneous shear layer for this range of density ratios. This result is substantiated by the general agreement found in §4.2 between the wavelength of regular shear-layer waves and the theoretically predicted value. To our knowledge, this result has not been experimentally confirmed previously (see discussion in Michalke 1984). Regarding the oscillating mode, recall from figure 19 that for $D/\theta = 83$ the jet supports oscillations whenever $S \leqslant 0.61$. The frequency of the oscillating mode for $S = 0.60$ and 0.50 is indicated in figure 22 by an arrow. We note that the frequency of oscillations is distinct from that of the most spatially amplified mode. Evidently, for $D/\theta = 83$ the jet supports both modes simultaneously. We shall shortly see how this observation is consistent with the observed dominance of the oscillating mode.

In figure 23 the non-dimensional frequency of both the oscillating mode and the most spatially amplified mode are plotted as functions of S for $D/\theta = 83$, 73 and 62.5. Notice that the curves for the two modes do not overlap for $D/\theta = 73$ and 62.5. For these D/θ, the oscillating mode is very intense close to the nozzle even for S near S_0. As a result, the harmonics of the oscillating mode grow rapidly in the region $25 \leqslant x/\theta \leqslant 75$, and indeed dominate the amplification curve for $S < S_0$. For all three D/θ, there is no obvious relationship between the frequencies of the most spatially amplified mode and of the oscillating mode. This result could not have been obtained from any scaling argument, simply because no experimental study has been conducted which shows how the most spatially amplified mode varies as a function of either D/θ or S. In fact it is clear from figure 23 that direct measurements are required to show that the frequencies are unrelated.

We note that $f\theta/U_e$ for air jets shown in figure 23 are close to those measured by Michalke (1971), but are some 30% below Drubka & Nagib's (1981) data ($= 0.013$). The latter authors non-dimensionalized the frequency using θ measured away from the nozzle. Because the momentum thickness increases with x, this procedure yields a

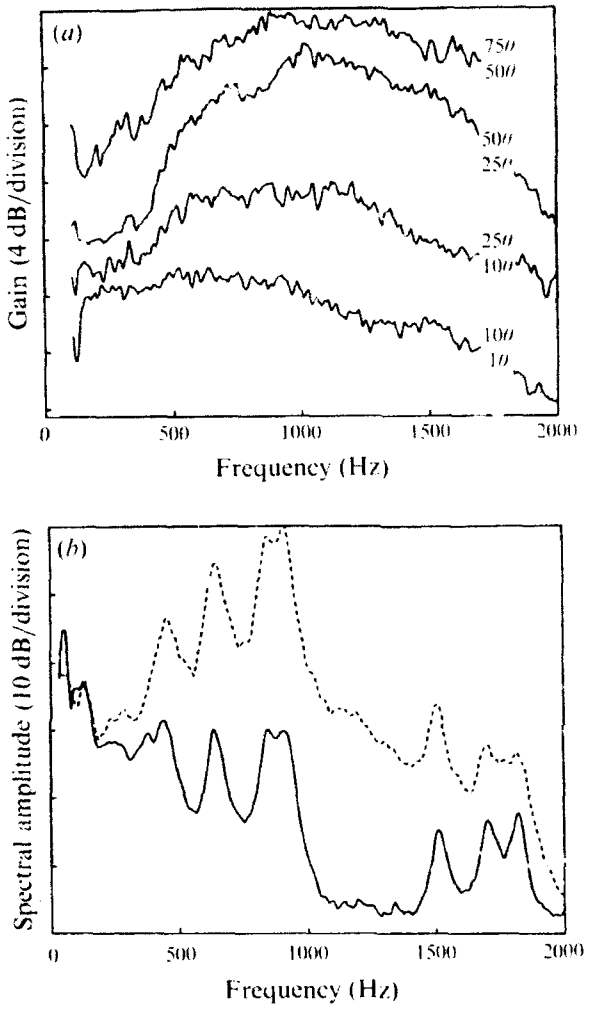

FIGURE 24. (*a*) Mode amplification as a function of frequency: $S = 0.50$; $D/\theta = 83$. Curves are labelled with the appropriate streamwise interval. The gain at each S is determined to within an arbitrary constant factor. (*b*) Power spectra of u' obtained in the shear layer: , $x/\theta = 1$; , $x/\theta = 75$. $S = 0.50$; $D/\theta = 83$. The arbitrary reference for the dB scale differs between the two curves.

higher value for $f\theta/U_c$; Drubka & Nagib indeed noted that θ increased by 40% in the first 80 momentum thicknesses downstream. Regarding the theory, the maximum spatial growth rate is predicted to occur at slightly lower $f\theta/U$ values as S is decreased (Michalke 1984). This agrees qualitatively with the data depicted in figure 23. It should be noted that the absolute value $f\theta/U_c$ corresponding with the spatially most amplified mode was found to be some 30–40% below the predicted value, both for $S = 1.0$ and 0.5. This is reminiscent of the fact that in numerous other studies on naturally excited cold air jets, $f\theta/U_c$ for the most energetic shear layer mode observed was likewise some 30–40% below the predicted value (e.g. Gutmark & Ho (1983).

To understand how the oscillating mode tends to dominate the flow field in spite of the fact that it is not associated with spectacular growth rates, we examine in figure 24(*a*) the streamwise evolution of the oscillating mode between $x/\theta = 1$ and 75 by partitioning the interval into four smaller subintervals, and evaluating the amplification

curves for each of the subintervals. For each subinterval, the total amplification of the oscillating mode (560 Hz) is not sharply distinguished from the amplification at neighbouring frequencies. The net total amplification between $x/\theta = 1$ and 75 may be viewed by comparing the power spectra obtained at the two locations, as seen in figure 24(*b*). Figures 24(*a*, *b*) together show that for $D/\theta = 83$, the large base-to-peak intensity of the oscillating mode is established right at the nozzle.

Our observations, in summary, are that, for $D/\theta = 83$, the base-to-peak intensity measured in the immediate vicinity of the nozzle is generally close in value to that measured at other locations upstream of the wave-breaking point; quite generally, in fact, the oscillating mode is not a consequence of an anomalous spatial growth. In the next section, we examine the effect that acoustic signals and other controlled changes to the environment have on the oscillating mode.

6. Response to acoustic forcing and other changes in the environment

6.1. *Sensitivity to coherent disturbances*

It has been established that the Strouhal number of the oscillating mode is independent of the maximum initial shear-layer disturbance level u'/U_o, even when u'/U_o varies by more than a factor of 2 (see figure 15). We can therefore say that the frequency selection is determined uniquely by the overall flow configuration, and by S and D/θ. Figure 18 (§5.2) shows similarly that the near-field base-to-peak intensity is not systematically affected by u'/U_o over the parameter region of interest. This means that a large component of the oscillation intensity is determined by the overall flow, as distinct from external sources. This appears to be so in spite of the significant random scatter seen in figure 18.

The following experiment is aimed at helping us understand the influence that time-dependent, spatially-coherent disturbances can have on the oscillation intensity. The disturbance is a sinusoidal acoustic signal which is spatially coherent in the sense that the acoustic wavelength is much larger than the spatial scales of the flow: $fD/a_\infty \ll 1$. Spatially coherent disturbances could arise in 'unforced' experiments as well, either from acoustic cavity resonances of the upstream settling chamber, or from uncontrolled far-field acoustic sources.

6.1.1. *Overall response*

In figure 25, the r.m.s. value of the hot-wire signal, E', is plotted as a function of x/θ for different values of the acoustic forcing strength, p'. p' is actually calculated using the voltage which drives the loudspeaker, which is directly proportional to the radiated acoustic pressure. These curves in figure 25 provide only a qualitative comparison of fluctuation intensities at differing streamwise locations, because even close to the nozzle, the mean velocity and the mean helium concentration differ for each x/θ, and so the proportionality constant relating E' and u' changes from place to place.

Figure 25(*a*) shows the response of the heterogeneous jet when forced at a frequency (860 Hz) that is unrelated to the oscillating mode (740 Hz). For the range of forcing amplitudes considered, the 860 Hz mode grows in a roughly exponential fashion until nonlinear damping inhibits further amplification. The growth rate in the near field ($x/\theta \leqslant 50$) appears to be unaffected by the forcing amplitude; the forcing merely augments the spectral intensities in a spatially uniform manner. The maximum intensity attained with downstream distance appears to be nearly independent of the forcing amplitude, except that the maximum is reached closer to the nozzle for larger

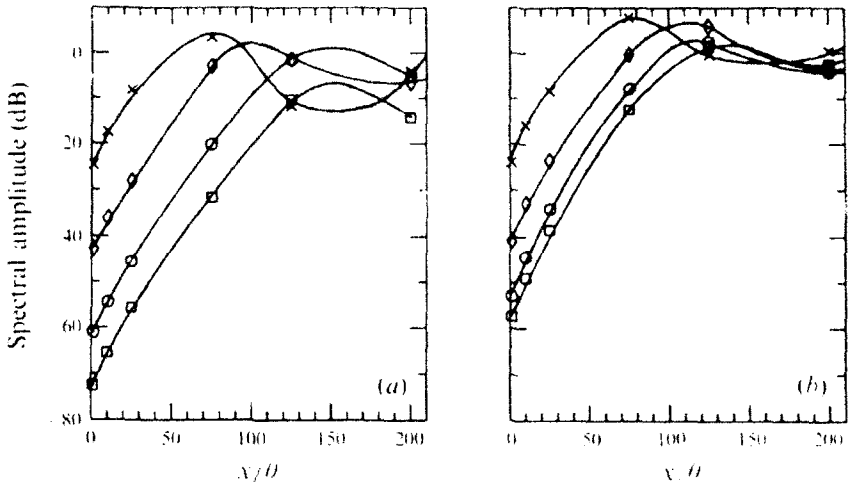

FIGURE 25. The magnitude of the signal from a hot wire located in the shear layer, plotted as a function of x/θ for various acoustic pressure levels p': □, no forcing; ○, 30 dB; ◇, 50 dB; ×, 70 dB. $S = 0.45$; $D/\theta = 83$. (*a*) Pure tone forcing at 860 Hz, and (*b*) pure tone forcing at 740 Hz (oscillating mode).

forcing amplitudes. Acoustically excited shear-layer modes in air jets exhibit these same response characteristics (Frymuth 1966).

Figure 25(*b*) shows that these qualitative results also hold when the same jet is excited at the frequency of the oscillating mode. The two principal differences are: first, the intensity of the oscillating mode in the absence of forcing is significantly greater than the 860 Hz mode; secondly, the fractional increase in intensity induced by the controlled forcing is correspondingly less for the oscillating mode.

Figure 25 helps to explain previous studies in acoustically forced heterogeneous jets. The present authors (Kyle 1986; Sreenivasan *et al.* 1989) found that at a fixed location in the flow, the oscillating mode was essentially insensitive to acoustic forcing, while other shear-layer modes exhibited linear dependence on p' when p' was small. For the present conditions, this behaviour is found at $x/\theta = 100$, where the oscillating mode response is nearly independent of the forcing amplitude (figure 25*b*); whereas, the shear-layer modes, because they are initially less intense, show definite dependence on acoustic forcing when the forcing is small or moderate (figure 25*a*).

6.1.2. *Excited portion of the response*

In order to obtain a more detailed, quantitative picture of the response to external forcing, it is convenient to decompose the velocity field as follows:

$$u' = u'_N(x, r, \text{low-level disturbances}) + u'_E(x, r, p'). \tag{6.1}$$

Here, u' is the measured intensity of velocity fluctuations in the presence of external acoustic forcing. u'_N is the response of the jet with no externally applied acoustic forcing; it is dependent upon the partial coordinates, x and r, and possibly upon low-level disturbances arising from within the jet facility and the ambient. u'_E is the excited portion of the response, and is dependent upon the spatial coordinates and upon p'. This decomposition is essential for recognizing the behaviour of u'_E, which alone is a function of the forcing amplitude, whenever u'_N is of comparable magnitude; this situation occurs when the jet is forced at the frequency of the oscillating mode. Note that (6.1) neither requires nor implies that receptivity is a linear process.

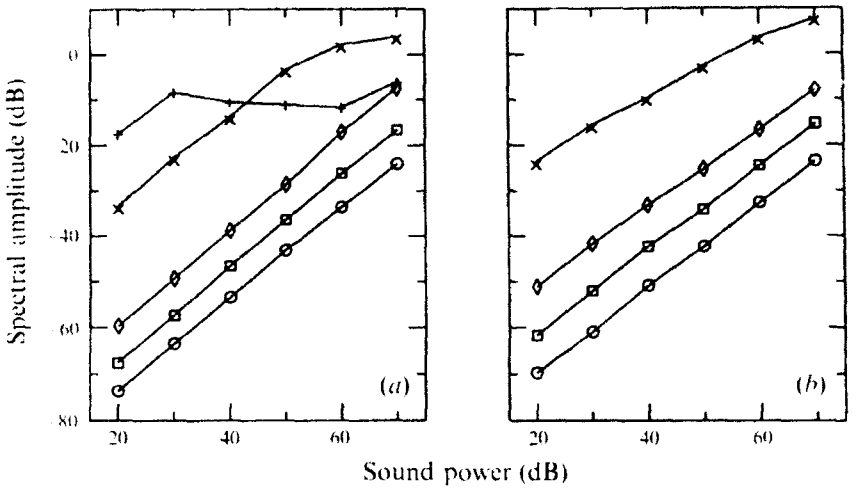

FIGURE 26. Excited portion of the response u_E as a function of p': ○, $x/\theta = 1$; □, $x/\theta = 10$; ◇, $x/\theta = 25$; ×, $x/\theta = 75$; +, $x/\theta = 200$. $S = 0.45$; $D/\theta = 83$. (*a*) Pure tone forcing at 860 Hz, and (*b*) pure tone forcing at 740 Hz (oscillating mode). The arbitrary reference for the dB scale varies from curve to curve.

Figure 26(*a*) shows u_E plotted as a function of p' at various streamwise locations at 860 Hz for the same flow conditions as in figure 25. It is expected that $E' \propto u'$ for data obtained at fixed probe locations very close to the nozzle, say for $x/\theta = 1$, where the acoustically excited disturbances are small enough that they do not significantly affect the mean flow. The data show that for excitation levels spanning approximately two decades, u_E is proportional to the forcing amplitude at $x/\theta = 1$, 10 and 25. It is seen that the linear portion of these three curves are all parallel to one another with slope equal to unity. Hence they must satisfy

$$\log_{10} u_E = \log_{10} p' + G(x), \tag{6.2}$$

where $G(x)$ does not depend upon p'. Letting $G(x) = \log_{10} g(x)$, (6.2) may be rewritten as

$$u_E = p' g(x), \tag{6.3}$$

where $g(x)$ describes the dependence of u_E on x. From (6.3) it is clear that receptivity is indeed a linear phenomenon for heterogeneous flows, just as it is for homogeneous shear flows. To our knowledge, this result has not been shown previously. In fact, (6.3) is a generalization of the results obtained for air jets by Freymuth (1966) who found $g(x) = Be^{\alpha x}$, with B and α dependent upon St_D alone. Although the amplification function $g(x)$ cannot be evaluated in this case, (6.3) shows that growth rate in the near field for the 860 Hz mode is independent of the initial disturbance intensity. This result is reflected in figure 25(*a*), where the amplification curves are all parallel to one another in the near field.

Figure 26(*b*) shows u'_E as a function of p' when the forcing frequency is set equal to the oscillating mode frequency. Note that these conditions are quite far from the onset, as $\Delta S \approx 0.25$. It is seen that u'_E is approximately proportional to p' at $x/\theta = 1$. Furthermore, for these flow conditions, the data suggest that (6.2) and (6.3) obtain with only slight error over a region extending from $x/\theta = 1$ to a location somewhere between $x/\theta = 25$ and $x/\theta = 75$. Thus, background disturbances can affect the evolution of vortical structures associated with the oscillating mode in much the same

way as they do in air jets. Indeed if such disturbances are very strong, figure 25 suggests that they may also affect the wave-breaking length and the overall structure of the mean field in the transition region.

Finally, we recall experimental results presented in Sreenivasan *et al.* (1989) for the case of extremely intense sinusoidal forcing. There, it was shown that the flow can exhibit behaviour that is characteristic of a coupled nonlinear oscillator, in that the oscillatory instability can become entrained or 'locked-in' to the frequency of the forcing.

6.4. *Test for the sensitivity to the turbulence level at the nozzle exit*

We have shown earlier that the frequency of the oscillating mode is independent of weak ambient disturbances. In the following experiment, we examine whether strong, spatially incoherent vortical fluctuations originating upstream of the nozzle have a strong effect on the stability of the oscillating mode (see also Strykowski & Russ 1992).

Two screens of differing mesh sizes were installed separately into the throat of the 13.3 mm nozzle, and the resulting qualitative changes in the power spectrum were observed using a hot wire located on the jet centreline. Although the screens were not fully characterized, the turbulence levels along the centreline in the nozzle plane were measured. The results for $Re = 3380$ were: (*a*) with no screen, $u'/U_c = 0.003$; (*b*) with the small-mesh screen, $u'/U_c = 0.022$; (*c*) with the large-mesh screen, $u'/U_c = 0.055$.

The nozzle fluid was then changed to helium while maintaining the same Re, and the three spectra shown in figure 27 were obtained. With no screen, the fundamental rises 25 dB above the background noise, with prominent harmonics. With the small-mesh screen, the fundamental rose only 20 dB and is somewhat broadened. With the large-mesh screen, the fundamental rose 25 dB above the noise and retained its 'spikiness'; however, its harmonics were attenuated relative to the flow without the screen. Thus, even at moderately high turbulence levels (of the sort not found in respectable jet facilities), the discrete frequency nature of the instability was not quenched. For both screens the frequency decreased. This is not surprising when one considers that the turbulent boundary layer must be thicker than the laminar one, and so by the scaling laws described in §5, the frequency is expected to decrease.

6.5. *Test for the sensitivity to the ambient environment*

Another experiment was made to test the sensitivity of the oscillating mode to the spatial confinement of the jet. If the jet is surrounded by an open-ended circular container sitting on the nozzle block, the oscillating mode hardly changes in intensity but shows a frequency increase by about 6 or 7% when the container diameter and height are about ten nozzle diameters. When the top of the container is covered by a flat board with a small central hole (diameter on the order of the nozzle diameter), the oscillating mode disappears; this is not surprising because the recirculating flow set up in the container renders, in due course, the density of the ambient gas equal to that of the nozzle gas. Experiments with several geometrical combinations of the container have suggested to us that the oscillating mode disappears only under drastic changes of the environment.

6.6. *Sensitivity to local perturbations*

While the oscillating mode is robust to many types of perturbations, it is quite sensitive to modifications of the mean velocity field. A case in point is its behaviour in the presence of an external body such as a small-diameter pin located at a suitable place inside the flow. This was investigated by Sreenivasan *et al.* (1989) who placed in the centre of the jet perpendicular to the axis a straight pin of a certain diameter and

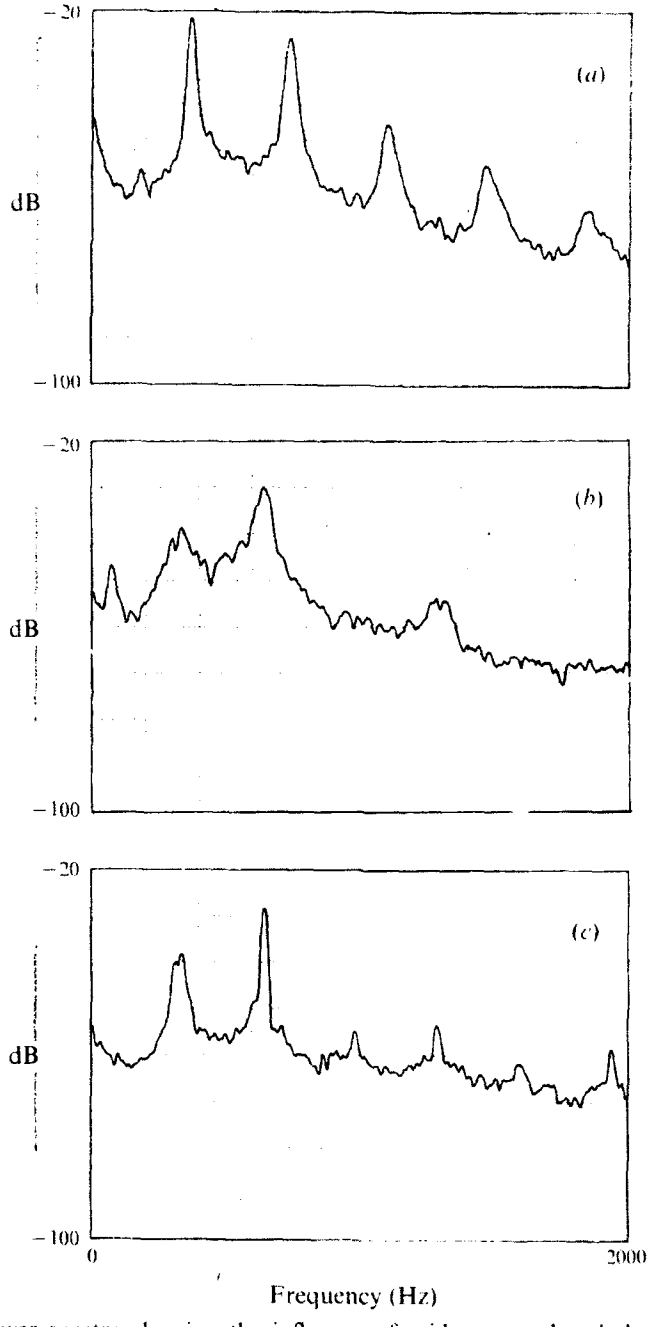

FIGURE 27. Power spectra showing the influence of grid-generated turbulence on the oscillating mode: $S = 0.14$; $D/\theta = 55$; $x/D = 2$; $r = 0$; $D = 13.3$ mm. (*a*) No grid, $u'/U_e = 0.003$; (*b*) finer grid, $u'/U_e = 0.022$; (*c*) coarser grid, $u'/U_e = 0.055$.

monitored the oscillating mode as a function of the pin position along the axis. Typically, the pin diameter was an order of magnitude smaller than the nozzle diameter. They observed that the oscillating mode could be suppressed whenever the pin was located in a certain neighbourhood in the flow. The observation suggests the possibility that the oscillating mode is a consequence of a local instability of the flow

in that neighbourhood, and that it disappear because the pin significantly disrupts the mean flow near where the instability arises (see also Monkewitz *et al.* 1990). It should be noted that perturbations to the mean velocity profile can affect the jet development in isothermal air jets as well (Bradbury & Khadem 1975).

7. Summary and discussion

7.1. *Distinction between various modes*

In heterogeneous jets which do not support the oscillating mode, shear-layer disturbances evolve in an analogous manner to those in constant density jets. We have found that very close to the nozzle, the power spectrum of u' is determined by a combination of the background spectral peaks at the nozzle exit and the spatial amplification rate of shear-layer modes. The latter is a smoothly varying function of the frequency of the disturbance. The maximum of this function is the 'most spatially amplified mode'. The most spatially amplified mode is a smoothly varying function of S. The non-dimensional frequency $f\theta/U_c$ of this mode is in agreement with other experimental studies in air jets. $f\theta/U_c$ decreases with S, as predicted by the spatial stability theory for non-uniform density jets. From films we found that the average value of the wavelength λ/θ is also well-predicted by the theory.

Important changes occur whenever the jet supports the oscillating mode. The structure in the near-field is highly organized both spatially and temporally, and centreline values of u'/U_c can become extraordinarily large. The processes of wave breaking and roll-up formation occur relatively close to the nozzle. The non-dimensional intensity of the oscillating mode and Strouhal number are definite functions of S and D/θ alone, that is they are not systematically affected by background disturbances or by Re within the parameter ranges of this study. The 'most spatially amplified' shear-layer mode also depends smoothly on S and D/θ, but the characteristics $(\lambda/\theta, f\theta/U_c)$ of this mode have been shown to be unrelated to those of the oscillating mode. The base-to-peak intensity of the oscillating mode measured in the immediate vicinity of the nozzle is generally close in value to measurements made further downstream in the near field. Thus, the shear layer acts as a spatial amplifier in the usual way; the oscillating mode does not exhibit an anomalously large spatial growth rate. The initial intensity of the oscillating mode can be influenced by acoustic forcing in a linear fashion, but in a quiet laboratory this component is small relative to the flow-induced portion.

7.2. *Vorticity*

Although we have not measured the vorticity distribution in the presence of the oscillating mode, it is possible to argue that the oscillating mode is associated with highly concentrated vortical structures. The instability of small disturbances in a laminar jet results in the migration of vorticity to form periodic concentrations. In a qualitative sense, the flow field which accompanies such vorticity disturbances is analogous to the nonlinear solutions of the vorticity equation introduced by Stuart (1967). These solutions, which are periodic in one direction and have shear in the other, were used by Stuart to describe the flow patterns in a shear layer with periodic vorticity. The stream function ψ for these solutions is given by

$$\psi = cr + \ln[C\cosh(r) + A\cos(x - ct)], \tag{7.1}$$

where c is the wave speed, and A and C are related by

$$A = (C^2 - 1)^{\frac{1}{2}}. \tag{7.2}$$

The parameter C indicates the degree of concentration of the vorticity: $C = 1$ corresponds to uniform vorticity in the x-direction, while $C \to \infty$ corresponds to a row of point vortices (Lamb 1945). Stuart calculated u'/U_c using (7.1) and (7.2) and found that at every point in the flow, the intensity increases monotonically with C. Note that the area integral of vorticity over any fixed region does not change with C in Stuart's solution; only the distribution is affected. The conclusion is that for a given amount of mean vorticity, the velocity fluctuation intensity can be strongly affected by the degree to which the vorticity disturbance is concentrated. We have measured the r.m.s. velocity u'/U_c along the centreline for two jets with density ratios $S = 1.0$ and $S = 0.29$ but with identical (non-dimensional) mean vorticity distribution at the nozzle exit (§4.4). We found that the jet supporting the oscillating mode ($S = 0.29$) exhibits significantly larger centreline fluctuation intensities (figure 12). This suggests that the vorticity is much more concentrated in the streamwise direction in jets which support the oscillating mode.

Winant & Browand (1974) have proposed a model for the vortex pairing process based on Stuart's solution. Their data show that for a given wave speed, both the initial growth rate of the subharmonic instability and the co-rotating speed of pairing vortices will increase with C. If it is true that the vorticity is more highly concentrated for the oscillating mode, then Winant & Browand's results would suggest that for $S = 0.29$, the pairing process should occur sooner and that the process should be more energetic. We have indeed shown (see table 1) that the pairing generally occurs sooner in jets dominated by the oscillating mode, and that the fluctuation levels reaches abnormally intense values (figure 12) near the location of vortex pairing.

7.3. *Theoretical models*

7.3.1. *Linear theory*

We have not succeeded in experimentally identifying the direct physical cause of the unusual instability arising under certain circumstances in variable-density jets. Various measurements discussed in §§4 and 5 show that a plausible explanation is provided by the linear theory for wave packet growth. Agreement and disparity between theory and experiment will now be reviewed.

If $\omega_i(k^*(0)) > 0$, the theory shows that in a streamwise homogeneous system, any spatially localized disturbance will, as time increases, lead to an increasingly monochromatic response, as observed. In fact, for $S = 0.50$ there is a reasonable correspondence between the predicted and observed values of $f\theta/U_c$, within a limited range of D/θ values around 80. In this same range of D/θ, approximate correspondence has been found between the predicted critical value of $S(= 0.72)$ and the observed onset value $S_o(= 0.61)$.

On the other hand, as D/θ increases much above about 80, the correspondence with the theory breaks down. In contradiction to the theory, S_o rapidly takes smaller values with increasing D/θ (figure 19). For large enough values of D/θ the oscillating mode vanishes, even though the theory predicts that for all $S \leqslant 0.62$, $\omega_i(k^*(0)) > 0$ even in the limit of $\theta \to 0$ (Monkewitz & Sohn 1986, 1988). A complete validation of any linear stability theory might comprise a matching of velocity data with computed eigenfunctions and eigenvalues, and a matching of any predicted critical parameter values with their experimentally determined onset values. By these standards, the correspondence between the oscillating mode and the spatio-temporal theory summarized in §1 would seem quite scant.

Even the somewhat limited correspondence found in §§4 and 5 between the linear theory and experiment may seem surprising because: (*a*) the instability theory assumes

homogeneity in the streamwise direction, whereas the flow in the near field is strongly inhomogeneous, and (*b*) the oscillating mode is so intense that linear mechanisms can be called into question without much thought. As regards (*a*), we have shown that the oscillating mode is global in the sense that the separate processes involved in laminar–turbulent transition occur in a globally organized fashion. On the other hand, its initiation may be related to the local spatio-temporal instability of a certain profile in the near field. Some support for this for this conjecture comes from Chomaz, Huerre & Redekopp (1988) who have shown that it is possible to construct a one-dimensional linear system which exhibits just this behaviour. They have shown that if a certain coefficient of the linearized Ginzburg–Landau equation is allowed to vary spatially, then within the context of that system, the existence of temporally growing modes of the form $\phi(x)e^{i\omega t}$ always requires that $\omega_i(k^*(0)) > 0$ for some spatial interval (see the review by Huerre & Monkewitz 1990). Concerning (*b*), a common experience is that the frequency of instability between the linear and nonlinear stages does not vary much. We stress that, although the linear theory might help in understanding the behaviour of the instability, large-amplitude motions play an essential role in sustaining the stable periodic state overall.

7.3.2. *Nonlinear theory*

Raghu & Monkewitz (1991) have pointed out that considerable physical insight might be obtained from studying the temporal growth of the oscillating mode. They have tried to show that the oscillatory disturbance field in a heated air jet can be modelled as a 'global temporal mode', that is,

$$u'(x,t) = A(t)f(x), \tag{7.3}$$

and that this mode obeys the Landau equation. Because of the similarity between the two flows, such a conclusion would also be appropriate to the heterogeneous flows considered here. Unfortunately, their results are inconclusive in that they obtained data at only a single streamwise location and provide no information as to whether the factorization (7.3) is valid. Moreover, our examination of onset for a wide range of flow conditions (§5.4) indicates that the spatial distribution of fluctuation intensity can itself be strongly amplitude-dependent near onset. For such behaviour the factorization (7.3) is inappropriate. Yet, the 'bifurcation' appears to be of the supercritical type for jets produced in many laboratory facilities. (For an exception under certain circumstances, see Sreenivasan *et al.* 1989.) In further pursuit of this line of inquiry, we propose that transient response simultaneously measured at different streamwise locations would be very valuable. At least under flow conditions with slow transient growth, one might learn more about the incipient stages of the oscillating mode.

We thank Professors Edward Bolton and Boa-Teh Chu for useful discussions. The work was financially supported by a grant from the Air Force of Scientific Research.

Appendix. Interpreting hot-wire spectra of small disturbance in laminar heterogeneous shear layers

While one is primarily interested in measuring the power spectral density of u' in the shear-layer region, a single hot wire cannot be used in regions of variable density where the mass fraction of helium c fluctuates. This is because the hot-wire voltage E is affected by both fields:

$$E(t;x,r) = E(c(t;x,r), U(t;x,r)). \tag{A 1}$$

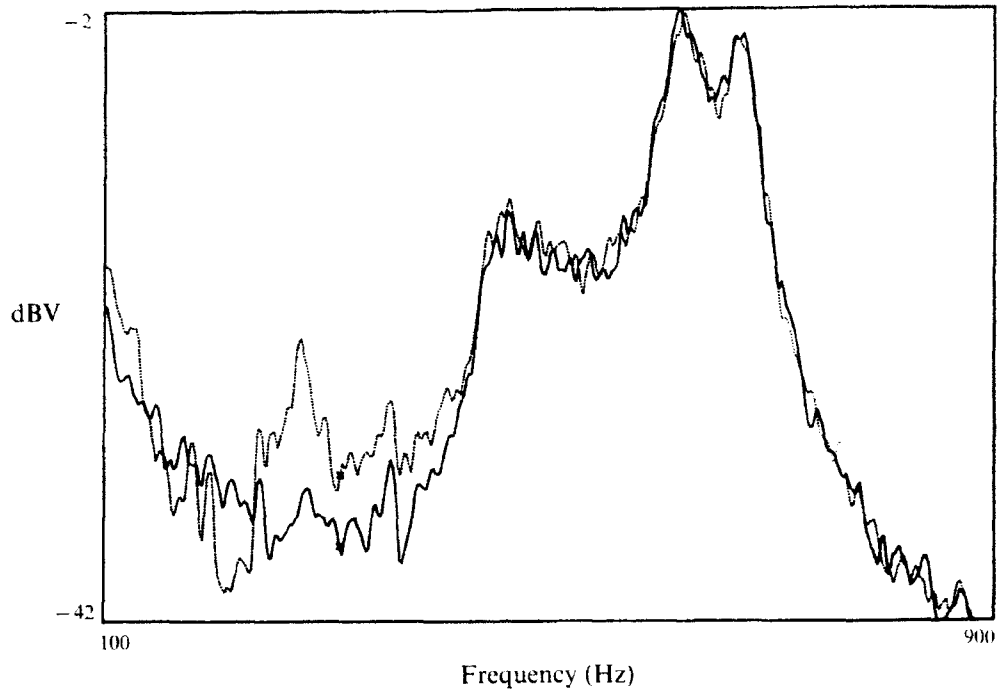

FIGURE 28. Power spectra of u' obtained at different radial locations in the shear layer region: $S = 1.00$; $D/\theta = 83$; $x/\theta = 75$; ——, potential core; – – – –, $r = \frac{1}{2}D + 5\theta$. The arbitrary reference for the dB scale varies for the two curves.

Instead, the power spectral density of u' has been obtained using a hot wire placed within the 'potential core' region, where both the mean velocity and the mean helium concentration are uniformly distributed in the radial direction. Because c can only decrease owing to mixing, it follows that concentration fluctuations are altogether absent in the potential core. For each of the flows discussed in this Appendix, the existence of this region has been confirmed. In each example, the hot wire was placed very near to where either U or c (or both) is just beginning to decrease with r, i.e. near the 'inner edge' of the shear layer. At this location the hot wire responds only to the velocity fluctuations associated with shear-layer disturbances, which are presumed to be strong along the inner edge of the shear layer (see Freymuth 1966).

Flow uniformity within the potential core, as well as the location of the inner edge of the shear layer, was confirmed in each case as follows. As the hot wire is moved radially outward from the centreline by small increments δr, the mean voltage changes according to:

$$E(r+\delta r) - E(r) = \frac{\partial E}{\partial U}\frac{\partial U}{\partial r}(\delta r) + \frac{\partial E}{\partial c}\frac{\partial c}{\partial r}(\delta r). \tag{A 2}$$

The partial derivatives $\partial E/\partial U$ and $\partial E/\partial c$ have been measured directly by placing the hot wire at the centre of the nozzle exit and separately varying U and c for several different conditions. It was found that $\partial E/\partial U, \partial E/\partial c > 0$, while $(\partial E/\partial U)/(\partial E/\partial c)$ is of order unity (see also Way & Libby 1971). Because $\partial U/\partial r, \partial c/\partial r < 0$ the mean voltage will always decrease with r. Thus, the radial extent of the potential core can be unambiguously determined.

Unfortunately, it is not convenient to rely upon measurements obtained in the potential core because the presence of the probe itself can alter the evolution of shear-

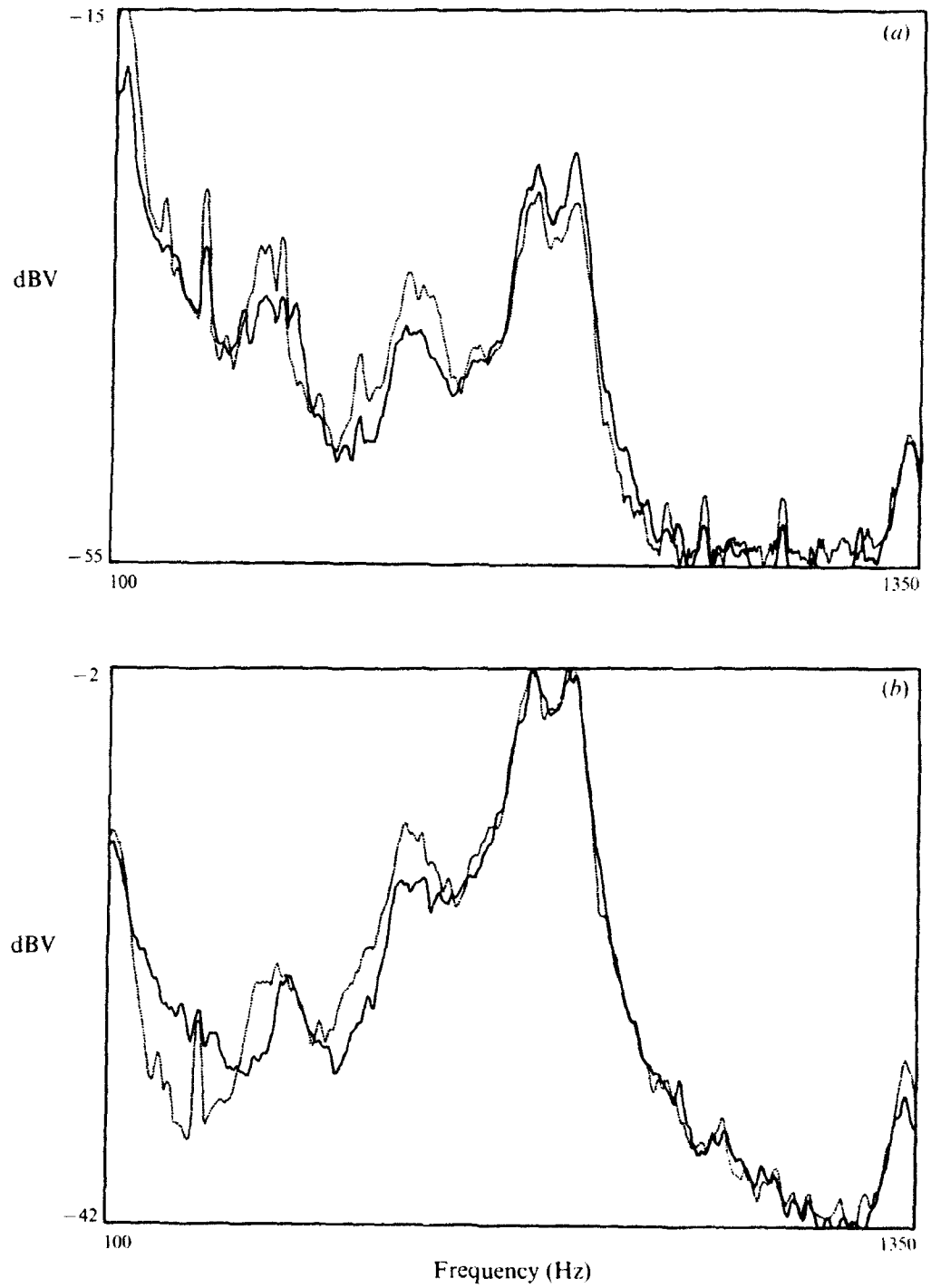

FIGURE 29. Power spectra of u' obtained at different radial locations in the shear layer region: $S = 0.70$; $D/\theta = 83$; – – –, potential core; ——, $r = \frac{1}{2}D + 5\theta$. (*a*) $x/\theta = 25$; (*b*) $x/\theta = 75$. The arbitrary reference for the dB scale varies for the two curves.

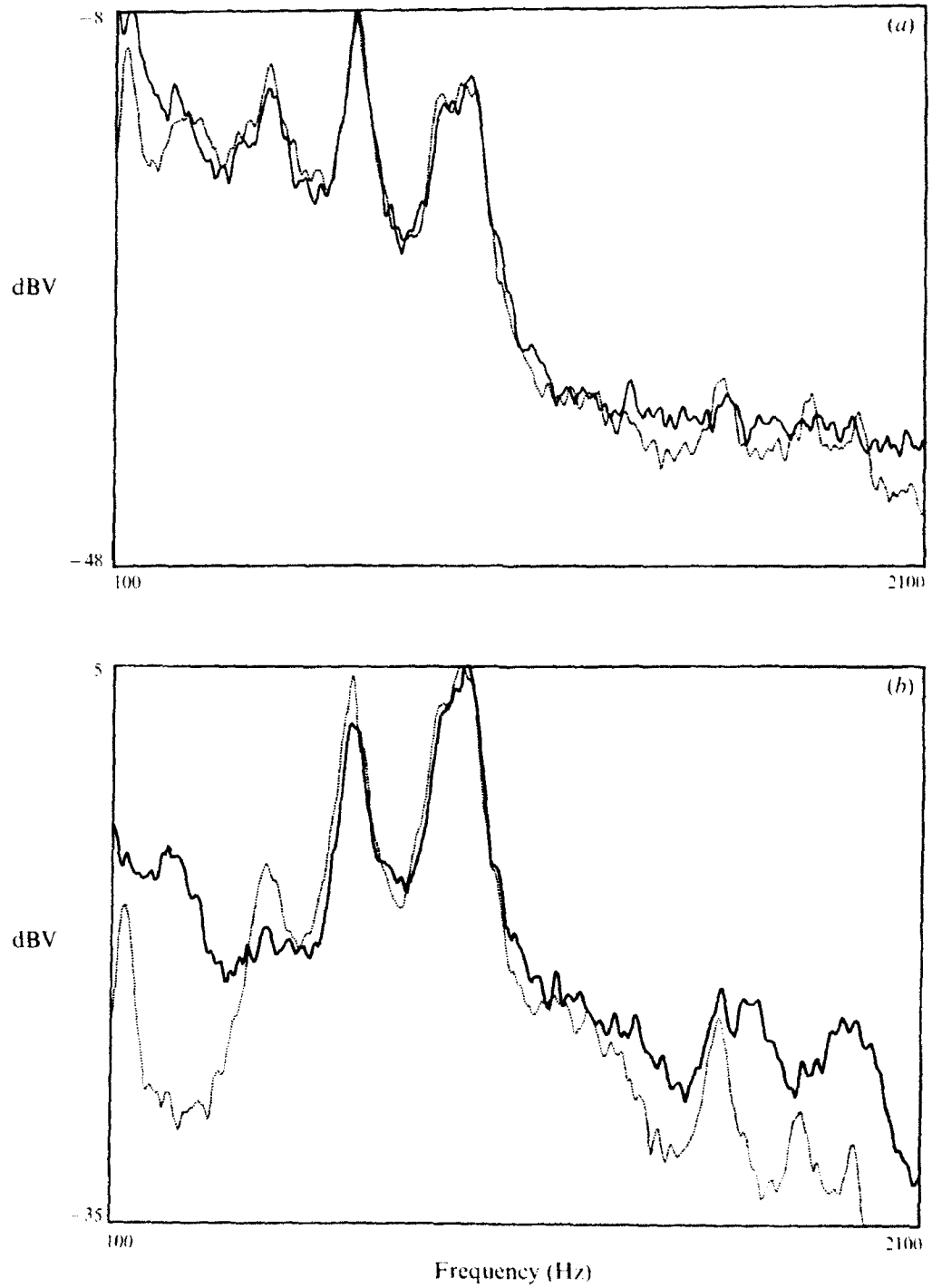

FIGURE 30. Power spectra of u' obtained at different radial locations in the shear layer region: $S = 0.50$; $D/\theta = 83$; – –, potential core; ——, $r = \frac{1}{2}D + 50$. (*a*) $x/\theta = 25$; (*b*) $x/\theta = 75$. The arbitrary reference for the dB scale varies for the two curves.

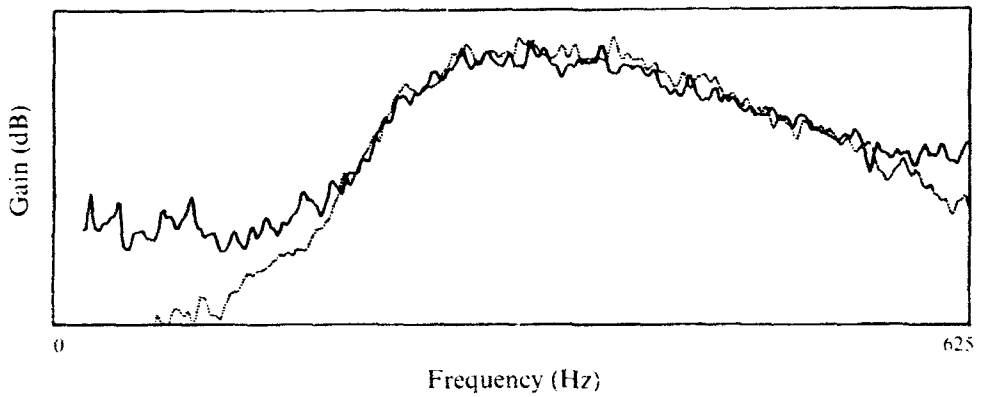

FIGURE 31. Mode amplification between $x/\theta = 25$ and $x/\theta = 75$ as a function of frequency for two different radial locations: $S = 0.60$; $D/\theta = 62.5$; - - -, potential core; ——, $r = \frac{1}{2}D + 5\theta$. The gain at each r is determined to within an arbitrary constant factor.

layer disturbances (Hussain & Zaman 1978; Sreenivasan *et al.* 1989). We have therefore measured the spectrum near the outer edge of the shear layer at $r = \frac{1}{2}D + 5\theta$ and exploited the result, discussed below, that in regions near the nozzle where disturbances are small, the power spectral density function obtained at $r = \frac{1}{2}D + 5\theta$ is approximately the same as the power spectrum of u' obtained in the potential core, except for a constant factor which is independent of the frequency.

Figure 28 shows power spectra of u' obtained in an air jet within the potential core ($r = \frac{1}{2}D - 10\theta$) and near the outer edge of the shear layer ($r = \frac{1}{2}D + 5\theta$) at $x/\theta = 75$. The spectra have been multiplied by arbitrary constants selected to show the similarity in the form of the curve. It is seen that the spectra are very similar, except at the lowest frequencies. Measurements in air jets obtained at different streamwise locations $x/\theta < 75$ and for differing D/θ all yield similar results. Figure 29 shows power spectra for $S = 0.70$ at $x = 25\theta$ and 75θ. Again the spectra obtained within the potential core and at $r = \frac{1}{2}D + 5\theta$ are approximately the same except for a constant normalizing factor. Figure 30(*a*) shows that this similarity can extend even to jets which support the oscillating mode, so long as measurements are made close to the nozzle. In figure 30(*b*), the similarity has degraded somewhat, presumably owing to large-amplitude effects. Note that for each potential core measurement, possible effects associated with the intruding probe were monitored using a second hot wire located well outside the shear layer. No intrusion effects were observed for the examples shown in figures 28–30.

During the course of this study, spectra obtained at $r = \frac{1}{2}D + 5\theta$ are used for calculating the following measures: (i) base-to-peak intensity measured in the immediate vicinity of the nozzle ($x/D = 0.10$). Whenever probe intrusion is not a factor, this measure is found to be roughly independent of r (see figure 30*a*). (ii) Most spatially amplified mode (§4.4). Figure 29 suggests that the functional relation between spatial amplification rate and frequency should be approximately independent of the radial position, except for a constant factor that is independent of frequency. More particularly, the maximum of the spatial amplification curve (§5.5) should be independent of radial position. This is confirmed in figure 31 for $S = 0.60$ and $D/\theta = 62.5$. Again, the spectra are seen to differ most in form at the lowest frequencies. (iii) Frequency of the oscillating mode. This measure is actually a constant for all points in the transitional flow.

REFERENCES

ABRAMOVICH, G. N., YAKOVLEVSKY, O. V., SMIRNOVA, A. N. & KRASHENINNIKOV, S. Y. 1969 An investigation of the turbulent jets of different gases in a general stream. *Acta Astron.* **14**, 229–240.

BEAN, H. S. (ed.) 1971 *Fluid Meters: Their Theory and Application*. ASME.

BECKER, H. A. & MASSARO, T. A. 1968 Vortex evolution in a round jet. *J. Fluid Mech.* **31**, 435–448.

BERS, A. 1983 Space-time evolution of plasma instabilities – absolute and convective. In *Handbook of Plasma Physics* (ed. M. N. Rosenbluth & R. Z. Sagdeev), vol. 1, pp. 451–517. North-Holland.

BRADBURY, L. J. S. & KHADEM, A. H. 1975 The distortion of jets by tabs. *J. Fluid Mech.* **70**, 801–813.

BRADSHAW, P. 1966 The effect of initial conditions on the development of a free shear layer. *J. Fluid Mech.* **26**, 225–236.

BRIGGS, R. J. 1964 *Electron Stream Interaction with Plasmas*. Research Monograph no. 29. MIT Press.

BROWAND, F. K. & LAUFER, J. 1975 The role of large scale structures in the initial development of circular jets. In *Turbulence in Liquids* (ed. J. L. Zakin & G. K. Patterson), pp. 333–344. Princeton, NJ: Science Press.

BROWN, G. L. & ROSHKO, A. 1974 On density effects in turbulent mixing layers. *J. Fluid Mech.* **64**, 775–816.

CHAN, Y. Y. & LEONG, R. K. 1973 Discrete acoustic radiation generated by jet instability. *CASI Trans.* **6** (2), 65–72.

CHOMAZ, J. M., HUERRE, P. & REDEKOPP, L. G. 1988 Bifurcations to local and global modes in spatially developing flows. *Phys. Rev. Lett.* **60**, 25–28.

CHRISS, D. E. 1968 Experimental study of the turbulent mixing of subsonic axisymmetric gas streams. *AEDC-TR-68-133* (available through NTIS).

COHEN, J. & WYGNANSKI, I. 1987 The evolution of instabilities in the axisymmetric jet. Part 1. The linear growth of disturbances near the nozzle. *J. Fluid Mech.* **176**, 191–219.

CORRSIN, S. T. & UBEROI, M. S. 1949 Experiments on the flow and heat transfer in a heated turbulent jet. *NACA Tech. Note* 1865.

CROW, S. C. & CHAMPAGNE, F. H. 1971 Orderly structure in jet turbulence. *J. Fluid Mech.* **48**, 547.

CRIGHTON, D. G. 1975 Basic principles of aerodynamic noise generation. *Prog. Aero. Sci.* **16**, 31–96.

DAVIES, P. O. A. L. & BAXTER, D. R. J. 1977 *Transition in Free Shear Layers* (ed. H. Fiedler). Lecture Notes in Physics, pp. 125–135. Springer.

DRUBKA, R. E. & NAGIB, H. M. 1981 *Fluids and Heat Transfer Report R81-2*. Department of Mechanical and Aerospace Engineering, Illinois Institute of Technology.

FREYMUTH, P. 1966 On transition in a separated laminar boundary layer. *J. Fluid Mech.* **25**, 683–704.

GASTER, M. 1962 A note on the relation between temporally-increasing and spatially-increasing disturbances in hydrodynamic stability. *J. Fluid Mech.* **14**, 222–224.

GASTER, M. 1965 On the generation of spatially growing waves in a boundary layer. *J. Fluid Mech.* **22**, 433–441.

GASTER, M. 1968*a* Growth of disturbances in both space and time. *Phys. Fluids* **11**, 723–727.

GASTER, M. 1968*b* The development of three-dimensional wave packets in a boundary layer. *J. Fluid Mech.* **32**, 173–184.

GASTER, M. & DAVEY, A. 1968 The development of three-dimensional wave packets in unbounded parallel flows. *J. Fluid Mech.* **32**, 801–808.

GEANKOPLIS, C. J. 1972 *Mass Transport Phenomena*. Holt, Rinehart and Winston.

GUTMARK, E. & HO, C. M. 1983 Preferred modes and the spreading rates of jets. *Phys. Fluids* **26**, 2932–2938.

HO, C. M. & HUANG, L. S. 1982 Subharmonics and vortex merging in mixing layers. *J. Fluid Mech.* **119**, 443–473.

HOCH, R. G., DUPONCHEL, J. P., COCKING, B. J. & BRYCE, W. D. 1973 Studies of the influence of density on jet noise. *J. Sound Vib.* **28**, 649–668.

HUERRE, P. & MONKEWITZ, P. 1985 Absolute and convective instabilities in free shear layers. *J. Fluid Mech.* **159**, 151–168.

HUERRE, P. & MONKEWITZ, P. 1990 Local and global instabilities in spatially developing flows. *Ann. Rev. Fluid Mech.* **22**, 473–537.

HUSSAIN, A. K. M. F. & RAMJEE, V. 1976 Effects of the axisymmetric contraction shape on incompressible turbulent flow. *Trans. ASME* I: *J. Fluids Engng* **98**, 58–69.

HUSSAIN, A. K. M. F. & ZAMAN, K. B. M. Q. 1978 The free shear layer tone phenomenon and probe interference. *J. Fluid Mech.* **87**, 349–381.

HUSSAIN, A. K. M. F. & ZEDAN, M. F. 1978 Effects of the initial condition on the axisymmetric free shear layer: Effects of the initial momentum thickness. *Phys. Fluids* **21**, 1100–1111.

KIBENS, V. 1980 Discrete noise spectrum generated by an acoustically excited jet. *AIAA J.* **18**, 434–441.

KOCH, W. 1985 Local instability characteristics and frequency determination of self-excited wake flows. *J. Sound Vib.* **99**, 53–83.

KOTSOVINOS, N. E. 1975 A study of the entrainment and turbulence in a plane buoyant jet. W. M. Keck Lab. Hydraul. Water Res. *Caltech Rep.* KH-R-32.

KYLE, D. 1986 Absolute instability in variable density jets. *Dept. Mech. Engng Rep.* 86FM6. Yale University.

KYLE, D. 1988 LIF images of He/N_2 jets. *Dept. Mech. Engng Rep.* FM88DK1. Yale University.

KYLE, D. 1991 The instability and breakdown of a round variable-density jet. PhD thesis. Department of Mechanical Engineering, Yale University.

KYLE, D. & SREENIVASAN, K. R. 1988 Discrete frequency phenomena in variable density round jets. *Bull. Am. Phys. Soc.* **33**, 2232 (abstract only).

KYLE, D. & SREENIVASAN, K. R. 1989 Stability properties of He/air jets. *Proc. ASME/ASCE Forum on Chaotic Flows*. LaJolla, CA (in press).

LAMB, L. 1945 *Hydrodynamics*. Dover.

LANDAU, L. D. & LIFSHITZ, E. M. 1959 *Fluid Mechanics. 6. Course of Theoretical Physics*. Pergamon.

LANDIS, F. & SHAPIRO, A. H. 1951 *The Turbulent Mixing of Co-axial Gas Jets*. Heat Transfer and Fluid Mechanics Institute. Stanford University Press, California.

LIEPMANN, D. 1991 Streamwise vorticity and entrainment in the near field of a round jet. *Phys. Fluids* A **3**, 1175–1185.

LONG, M. B., FOURGUETTE, D. C., ESCODA, M. C. & LAYNE, C. B. 1983 Instantaneous Ramanography of a turbulent diffusion flame. *Optics Lett.* **8** (5), 244–246.

MASLOWE, S. A. & KELLY, R. E. 1971 Inviscid instability of an unbounded heterogeneous shear layer. *J. Fluid Mech.* **48**, 405–415.

MICHALKE, A. 1971 Instabilitat eines Kompressiblen Runden Freistrahls unter Berucksichtigung des Einflusses der Strahlgrenzschichtdicke. *Z. Flugwiss.* **19**, 319–328.

MICHALKE, A. 1984 Survey on jet instability theory. *Prog. Aerospace Sci.* **21**, 159–199.

MONKEWITZ, P. A., BECHERT, D. W., BARSIKOW, B. & LEHMANN, B. 1990 Self-excited oscillations and mixing in a heated round jet. *J. Fluid Mech.* **213**, 611–639.

MONKEWITZ, P. A., LEHMANN, B. T., BARSIKOW, B. & BECHERT, D. W. 1989 The spreading of self-excited hot jets by side jets. *Phys. Fluids* **7**, 446–448.

MONKEWITZ, P. A. & SOHN, P. A. 1986 Absolute instability in hot jets and their control. *AIAA paper* 86-1882.

MONKEWITZ, P. A. & SOHN, P. A. 1988 Absolute instability in hot jets. *AIAA J.* **26**, 911–916.

MORKOVIN, M. V. & PARANJAPE, S. V. 1971 On acoustic excitation of shear layers. *Z. Flugwiss.* **19**, 328–335.

MORRIS, P. J. 1976 The spatial viscous instability of axisymmetric jets. *J. Fluid Mech.* **77**, 511–529.

PAVITHRAN, S. & REDEKOPP, L. G. 1989 The absolute-convective transition in subsonic mixing layers. *Phys. Fluids* A **1**, 1736–1739.

PRASAD, R. R. & SREENIVASAN, K. R. 1990 Quantitative three-dimensional imaging and the structure of passive scalar fields in fully turbulent flows. *J. Fluid Mech.* **216**, 1–34.

RAGHU, S. & MONKEWITZ, P. A. 1991 The bifurcation of a hot round jet to limit-cycle oscillations. *Phy. Fluids* A **3**, 501–503.

RAYLEIGH, LORD 1894 *Theory of Sound*, vol. 1. Macmillan.

SAROHIA, V. & MASSIER, P. F. 1977 Experimental results of large-scale structures in jet flows and their relation to jet noise production. *AIAA J.* **16**, 831–835.

SFORZA, P. M. & MON, R. F. 1978 Mass, momentum, and energy transport in turbulent free jets. *Intl J. Heat Mass Transfer* **21**, 371–384.

SMITH, D. J. & JOHANNESEN, N. H. 1986 The effects of density on subsonic jet noise. *IUTAM Symp. on Aero- and Hydro- Acoustics, Lyons*. Springer.

SREENIVASAN, K. P., RAGHU, S. & KYLE, D. 1989 Absolute instability in variable density jets. *Exps Fluids* **7**, 309–317.

STEIN, G. D. 1969 Design of a multipurpose wind tunnel. *Rev. Sci. Instrum.* **40**, 1058–1061.

STRYKOWSKI, P. J. & NICCUM, D. L. 1991 The stability of countercurrent mixing layers in circular jets. *J. Fluid Mech.* **227**, 309–343.

STRYKOWSKI, P. J. & RUSS, S. 1992 The effect of boundary layer turbulence on mixing in heated jets. *Phys. Fluids* **A4**, 865–868.

STRYKOWSKI, P. J. & SREENIVASAN, K. R. 1990 On the formation and suppression of vortex 'shedding' at low Reynolds numbers. *J. Fluid Mech.* **218**, 71–107.

STUART, J. T. 1967 On finite amplitude oscillations in laminar mixing layers. *J. Fluid Mech.* **29**, 417–440.

STURROCK, P. A. 1958 Kinematics of growing waves. *Phys. Rev.* **112**, 1488–1503.

SUBBARAO, E. R. 1987 An experimental investigation of the effects of Reynolds number and Richardson number on the structure of a co-flowing buoyant jet. PhD thesis, Department of Aeronautics and Astronautics, Stanford University, Palo Alto, USA.

TOMBACH, I. H. 1969 Velocity measurement with a new probe in inhomogeneous turbulent jets. PhD thesis, California Institute of Technology.

WAY, J. & LIBBY, P. A. 1971 Application of hot-wire anemometry and digital techniques to measurements in a turbulent helium jet. *AIAA J.* **9**, 1567–1573.

WILKI, C. R. 1950 *J. Chem. Phys.* **18**, 517–519.

WILLE, R. 1963 Beitrage zur Phanomenologie der Freistrahlen. *Z. Flugwiss.* **11**, 222–223.

WINANT, C. D. & BROWAND, F. K. 1974 Vortex pairing: the mechanism of turbulent mixing-layer growth at moderate Reynolds number. *J. Fluid Mech.* **63**, 237–255.

YULE, A. J. 1978 Large-scale structure in the mixing layer of a round jet. *J. Fluid Mech.* **89**, 413–432.

Combust. Sci. and Tech., 1993, Vol. 89, pp. 1-7
Photocopying permitted by license only

©Gordon and Breach Science Publishers S.A.
Printed in United States of America

The Thickness Distribution of OH Regions in a Turbulent Diffusion Flame

A. W. JOHNSON and K. R. SREENIVASAN *Department of Mechanical Engineering, Yale University, New Haven, CT 06520, USA*
M. WINTER *United Technologies Research Center, East Hartford, CT 06108, USA*

(Received August 19, 1991; in final form June 12, 1992)

Abstract—The OH radicals in a hydrogen diffusion flame burning in ambient air were visualized using planar laser-induced fluorescence. Local thicknesses of the OH regions were measured at three downstream distances. Measurements show that the thickness is distributed approximately according to a lognormal probability density function.

1. INTRODUCTION

The spatial structure of turbulence plays a significant role in determining dynamical processes such as mixing, stability, and lift-off in turbulent flames. Understanding the basic structure of turbulent diffusion flames involves many issues such as turbulent mixing, scalar diffusion, multistep chemical kinetics and heat release. Molecular mixing occurs across scalar interfaces between the fuel and the oxidant. Combustion occurs when mixing is completed to stoichiometric limits within these interfaces. The corresponding heat release will in turn have a large effect on the local structure of turbulence. This interplay is quite complex, and we shall not be concerned here with those details. Instead, we concentrate on one aspect, namely the thickness distribution of hydroxyl radical (OH) in a hydrogen-air diffusion flame. OH is a product of combustion and, with some limitations to be discussed later, is considered to be a diagnostic of the flame zone.

The spatial structure of OH regions has previously been characterized in terms of thickness, axial scale, orientation, and location in hydrogen-air diffusion flames at various Reynolds numbers (Seitzman et al., 1990). However, the probability density function representing the thickness of OH regions has not previously been studied in detail. In cold flows, the thickness of mixing interfaces is on the order of the smallest scales of motion (LaRue & Libby, 1974; Sreenivasan et al., 1989). It can further be shown that the probability distribution of such scales is lognormal. If reaction zone structures have *similar properties*, it is possible that our knowledge of the cold flow structure may be translated, even if in a somewhat limited sense, to the characterization of combusting systems.

With this in mind, we have made measurements of the thickness distribution of the OH regions in a low-to-moderate Reynolds number hydrogen diffusion flame burning in air. The measurements show that the OH regions are quite fat (in comparison with the Kolmogorov thickness of the cold flow), and that their thickness is approximately lognormal in distribution. Some remarks are made on the interpretation of these observations.

2. EXPERIMENTAL PROCEDURE

Experiments to visualize a diffusion flame were designed at the United Technologies Research center. The goal was to identify the reaction region and obtain a data base for its thickness distribution. Because of the difficulties in imaging instantaneous reaction zones of hydrogen flames and the good signal qualities of OH, images of OH regions—which

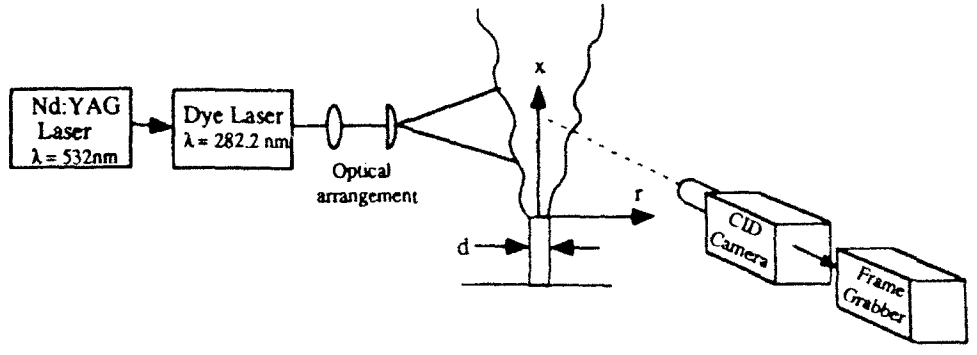

FIGURE 1. Experimental configuration for the measurement of OH radicals in a nonpremixed hydrogen flame. Nd: YAG Laser pulsed at 10 Hz. Dye Laser frequency doubled to $\lambda = 282$ nm. The CID camera had a capacity of 512 × 512 pixels and the overall resolution was about 0.1 mm/pixel. Laser sheet thickness was on the order of 0.1 mm. Nozzle diameter d = 2.5mm. The nozzle Reynolds number was Re = 2400.

mark areas where combustion has been completed—were recorded. The applicability of OH as a marker of reaction regions in flames has been discussed by Hanson (1987) and Vandsburger et al. (1988), and is also addressed later in this paper.

The experimental set up is shown in Figure 1. Hydrogen was ejected upwards from a 2.5 mm diameter round nozzle into ambient air with a nozzle velocity of 108 m/s. The cold flow Reynolds number based on nozzle diameter was Re = 2400. Images were recorded at axial positions centered around distances of 38, 58 and 98 nozzle diameters. Some details are given below.

The OH free radicals from the products of hydrogen-air reaction were visualized by planar laser-induced fluorescence (PLIF). A Spectra-Physics Nd:YAG laser frequency-doubled to a wavelength of 532 nm pumped a dye laser which was frequency-doubled to a peak absorption wavelength of OH atoms at 282 nm. The dye laser beam was passed through an optical arrangement which produced a laser sheet of thickness of the order of 100 μm. The laser pulse width was on the order of 10 nsec and the laser energy at the flame was on the order of 20-30 mJ. Fluorescence of the OH radicals were induced by the energy and wavelength of the laser sheet where the (1,0) band of the $A^2\Sigma^+$-$X^2\Pi_i$ transition was excited at 282 nm. This gives fluorescence from both (1,1) and (0,0) bands. Temperature and quenching effects on OH fluorescence were minimized by adjusting the laser to saturate the transition. Pfefferle et al. (1988) have demonstrated the effectiveness of such a technique in the PLIF images of OH in a chemically reacting boundary layer. In their work, saturation was achieved to within 10%. Illuminated regions were recorded on an intensified XYBION CID camera with a gating synchronized with the pulsing of the laser. For these measurements, the gating time was less than 1 μs and the camera was operated in a non-interlaced mode. Data were recorded through an interference filter with a full width half-maximum (FWHM) of 10 nm centered at 308 nm, allowing detection primarily from the (0,0) band. The camera resolution of 512 × 512 pixels allowed an average image resolution of 0.09 mm/pixel. Output of the camera was fed to a video recorder for continuous acquisition.

The videotaped data were digitized on a Macintosh II using a model DT2255 Data Translation digitizing card with a 640 × 480 square pixel format and associated image processing software. Images were digitized to 8-bits and the dynamic range was on the order of 30; however, the precise value of the signal to noise ratio varied from pixel to

TABLE I

Basic flow parameters with scaling estimates. Nozzle Reynolds number, $Re = 2000$. Nozzle exit velocity, $U_{nozzle} = 108$ m/s. Nozzle diameter, d = 2.5mm. Centerline velocity at a downstream distance x was estimated by $U_c = 6.4(d/x)U_{nozzle}$. The centerline rms velocity fluctuation, $u' = 0.3U$. Integral scale, $l \sim 0.25$ local jet diameter. Turbulent Reynolds number, $Re_l = u'l/\nu$, where ν is the viscosity of hydrogen at 300K. Kolmogorov scale, $\eta = l(Re_l)^{\frac{-3}{4}}$. Damköhler number, $Da = \tau_t/\tau_c$, where τ_t = mixing time scale $= \eta^2/\nu$ and τ_c = reaction time scale. The latter was estimated to be 20 μs for 2-body forward reactions and 3 ms for 3-body recombination reactions (Barlow et al. 1990).

x/d	U_c (m/s)	u'(m/s)	l(mm)	Re_l	η(mm)	τ_t(μsec)	Da_{2-body}	Da_{3-body}
38	18.18	5.45	7.4	368	0.09	73	3.65	0.024
58	11.92	3.57	11.5	368	0.14	176	8.82	0.058
98	7.05	2.11	19.4	368	0.23	476	23.82	0.159

pixel, being the lowest where the structures were diffuse and OH concentrations low. The measurements here were limited to assessing the relative thickness of the spatial distribution of the OH regions, and the absolute value of pixel intensities and their relation to OH concentration were used only to determine the 'edges' of OH regions. Considering the system as a whole, the projected resolution amounts to approximately 0.095 mm/pixel in the vertical direction and 0.15 mm/pixel in the horizontal direction over a 46 mm × 46 mm area. The smallest structure measured was on the order of 1mm in width.

Twenty randomly selected images of the flame at each of the three streamwise locations were digitized. The thickness of the OH region in each of these images was measured at equal intervals along the length of the flame. At each interval, the shortest line across the OH region was defined and a profile of the pixel intensities along the line was obtained. The edge of the OH region was identified by setting a threshold of pixel intensity from which best defined the width of the profile and was sufficiently above the noise level of the image. The number of pixels along the line crossing the OH regions with intensities above the threshold value were then counted. This procedure was repeated using three different pixel intensity thresholds, corresponding to intensities 60, 70 and 80 percent below the maximum intensity. From visual observations, it was found that much lower thresholds would have been contaminated by noise. For comparison, hand measurements were also taken directly from images projected on to a large screen. In this technique the edges of the OH regions were determined visually rather than by pixel thresholding. It should be noted that glancing cuts of the laser through the jet add uncertainties to the interpretation of the data. Structures from the images which were clearly deemed as glancing cuts were not used in the analysis. From the recorded data, histograms of the thickness of the OH regions were produced.

3. RESULTS AND DISCUSSION

The basic parameters of the cold flow, estimated according to the 'standard' evolution of round jets (e.g., Wygnanski & Fiedler, 1968), are shown in Table I. These data are not directly relevant to the local flame front because the latter is nearly laminarized by the large heat release. Yet, the local reaction regions are buffeted by the turbulence in the core of the flow; some idea of the cold flow data was therefore thought to be appropriate. The turbulent Reynolds number Re_l is based on the estimated root-mean-square (rms) centerline velocity and integral scales. The Kolmogorov length and velocity scales, estimated according to the standard turbulence scaling relationship, are included; so are estimates of Damköhler number, Da, based on chemical reaction time scales of both the forward and recombination reactions.

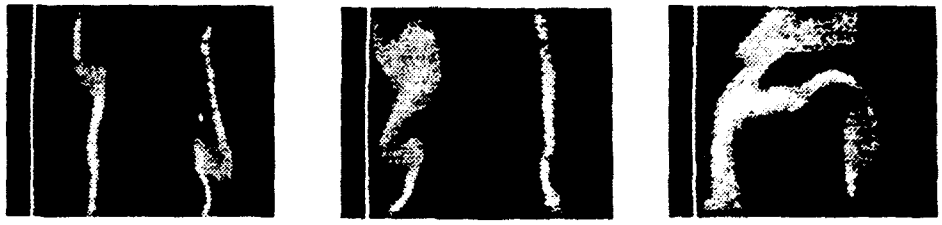

FIGURE 2. Visualizations of OH concentration in a hydrogen diffusion flame at three locations downstream of the nozzle. Reynolds number at the nozzle is Re = 2400. Nozzle diameter, d = 2.5 mm. Width of the images is x ~ 46 mm in real space.

Before we present the results, a comment is in order on the effect of buoyancy, which might be expected to have increasing influence with increasing distances from the nozzle. Some symptoms of buoyancy in jet flows include increases in momentum flux, Reynolds number, and activity and size of large eddies. In studies of buoyancy effects on turbulent diffusion flames of propane, Becker & Yamazaki (1978) found that transition from a momentum driven to a buoyant driven state begins when a nondimensional streamwise coordinate, $\xi = \mathrm{Ri}_s^{1/3}(x/D_s)$, approaches a value between 1 and 2. Here, Ri_s is a 'source' Richardson number based on an effective 'source diameter' given by D_s. The value of ξ is substantially smaller in our flame except at the last measuring station, where it is of the order of 3. Thus, *a priori* considerations suggest that some effect of buoyancy may be present at the last measuring station. We shall later take a closer look at this issue.

Figure 2 shows three typical realizations of the OH regions at the three downstream positions mentioned earlier. As expected, they become more convoluted with increasing downstream distance. The OH regions are thin in comparison with the flow width, but their thickness is far larger than the Kolmogorov scale of the cold flow. As observed in a similar experiment on a hydrogen-air diffusion flame (Kychakoff et al., 1984), this relative fatness of the OH regions is in part due to the low Reynolds number of the flow. In the experiment by Kychakoff et al. (1984) it was found that with increasing Reynolds number, the width of the structures became smaller and had greater variations in size. Similar characteristics were also observed by Seitzman et al. (1990), who note that the diffuse structures are predicted well by the quasi-equilibrium distributed reaction (QEDR) model developed by Bilger (1988). A detailed review of the influence of other factors such as dissipation, mixture fraction and their role in the structure and thickness of turbulent nonpremixed flames can be found in Bilger (1988).

Because of the relatively slow recombination time of OH, we also expect the thickness of the OH regions to be broader than the instantaneous reaction zones. Bilger (1989a) gives an estimate for the flame thickness Λ in terms of the Kolmogorov scale η for one-step, second order irreversible reactions as $\Lambda/\eta = Da^{-1/3}Re^{1/4}Sc^{-1/2}\gamma\prime^{-1/3}$ where Sc is the Schmidt number and $\gamma\prime$ is the rms of mixture fraction. This relationship qualitatively explains how the Damköhler number can affect the size of a reaction zone. As shown in Table I, for hydrogen-air reactions Da is much smaller for the reverse reaction involving the free radical OH than for the forward reaction. Hence we expect OH regions to cover a larger area than the instantaneous flame region. For laminar counterflow methane-air diffusion flames, predicted number densities of both CH and OH in mixture fraction

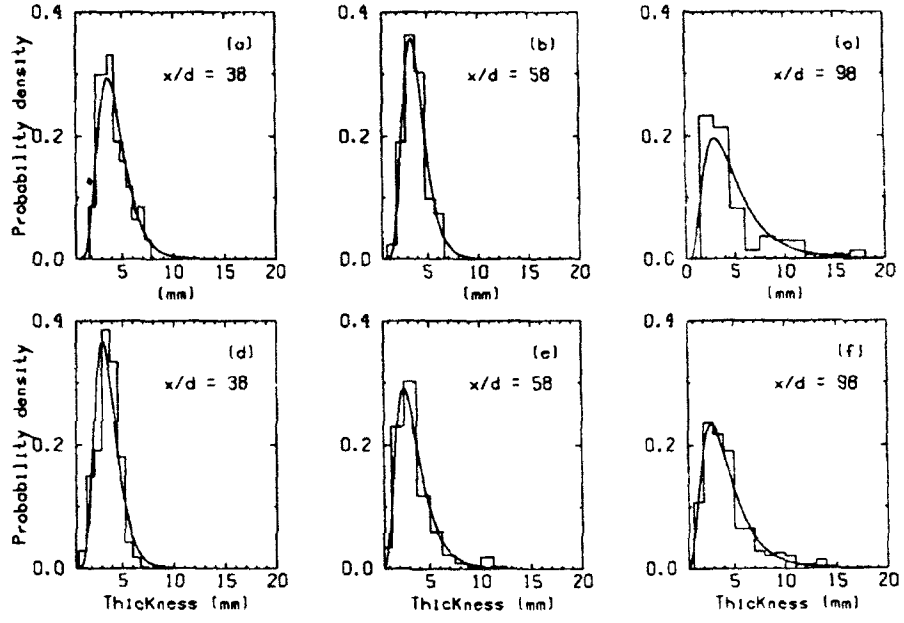

FIGURE 3. Distributions of the thickness of the OH regions at 38, 58, and 98 diameters downstream of the nozzle. (a)-(c): Edges of OH regions determined by setting a threshold on the pixel intensity (see text for details). (d)-(f): Edges of OH regions determined visually. Smooth curves denote fits using mean and rms values from the measurements.

space (Bilger, 1989b) have shown that the OH regions are broader and exist in high concentrations slightly to the lean side of the instantaneous reaction zone marked by CH.

Figures 3(a)-3(f) are histograms of the thickness of OH regions taken from the digitized images at 38, 58 and 98 diameters downstream. Figures 3(a)-3(c) represent measurements obtained by defining the 'edges' of the OH regions by a threshold which is 60% below the largest intensity. It was found that the histograms were the same for two other pixel thresholds (70% and 80% below the maximum intensity). Figures 3(d)-3(f) correspond to hand measurements described earlier. The histograms at each axial location, obtained by the two different methods, are reasonably close to each other. To the extent that the histograms are not sensitively dependent on the axial location, we infer that the buoyancy effects even at the last station are not severe—even though *a priori* considerations suggest otherwise. This should not come as a total surprise because buoyancy has different degrees of effect on different quantities; apparently, the normalized histograms belong to the category where the effects of moderate levels of buoyancy are minimal.

An attempt was made to fit the histograms with a lognormal probability density function using the measured mean and standard deviation. The lognormal fits, shown by the solid curves, are reasonable. The histograms were also fitted by the Rayleigh distribution function which is similar in shape to the lognormal. The Rayleigh distribution fits the body of the histograms reasonably well, but not the tails. It was found that the lognormal estimates were closer to the measurements. Low-order statistical data are presented in Table II.

TABLE II
Statistical averages from OH thickness measurements.

x/d	Average thickness (mm)	rms thickness (mm)	Skewness	Flatness
38	4.40	1.78	1.26	5.07
58	4.32	1.79	1.33	6.77
98	5.22	3.59	1.98	7.11

One would like to extend these statements to the reaction regions themselves. Unfortunately, as already remarked, because of the slow recombination time and temperature dependence of OH radicals, the visualized OH regions are larger than the reaction zone. The exact relationship between the thickness distribution of instantaneous and post combustion regions is not evident. However, OH has previously been noted as a good diagnostic of reaction zone structures (Hanson, 1987; Vandsburger et al., 1988; and Kychacoff et al., 1984). Experiments such as those by Smyth et al. (1985) on methane-air diffusion flames as well as the study of Bilger (1989b) and Keyes & Smooke (1990), have shown that peaks of OH concentrations coincide with high temperature areas and tend toward the lean side of the reaction zone. Although our reservations noted above remain in force, the prospect that these results are applicable to instantaneous flame and mixing regions is promising.

5. CONCLUSIONS

A hydrogen diffusion flame was visualized by the laser induced fluorescence of OH radicals. Measurements showed that the thickness of OH-containing regions is approximately lognormal. Such findings may be applicable to the flame thickness and to mixing interfaces.

ACKNOWLEDGEMENTS

We thank Professor R. W. Bilger for his comments on an earlier draft. A careful reading by a referee improved the text. This research has been supported by the United Technologies Corporation and the Air Force Office of Scientific Research.

REFERENCES

Barlow, R.S., Dibble, R.W., Chen, J.-Y., and Lucht, R.P. (1990) Effect of Damköhler Number on Superequilibrium of OH Concentration in Turbulent Nonpremixed Jet Flames. *Combustion and Flame*, **82,** 235.

Becker, H. A., and Yamazaki, S. (1978) Entrainment, Momentum Flux and Temperature in Vertical Free Turbulent Diffusion Flames. *Combustion and Flame*, **33,** 123.

Bilger, R. W. (1988) The Structure of Turbulent Nonpremixed Flames. *Twenty-Second Symposium (International) on Combustion/The Combustion Institute.* p. 475.

Bilger, R. W. (1989a) Turbulent Diffusion Flames. *Ann. Rev. Fluid Mech.* **21:** 101-135.

Bilger, R. W. (1989b) Reaction Zone Structure in Turbulent Diffusion Flames. *Joint International Conference Australia/New Zealand & Japanese Sections/The Combustion Institute, University of Sydney.*

Hanson, R.K. (1986) Combustion Diagnostics: Planar Imaging Techniques. *Twenty-First Symposium (International) on Combustion/The Combustion Institute.* p. 1677.

Keyes, D. E., and Smooke, M. D. (1989) Numerical Solution of 2-D Axisymmetric Laminar Diffusion Flames. *Combustion Science and Technology*, **67,** p. 85.

Kychakoff, G., Howe, R. D., Hanson, R. K., Drake, M. C., Pitz, R. W., Lap, M., and Penney, C. M., (1984) Visualization of Turbulent Flame Fronts with Planar Laser-Induced Fluorescence. *Science*, **224,** 382.

LaRue, J. C., and Libby, P. A. (1974) Temperature and Intermittency in the Turbulent Wake of a Heated Cylinder. *Phys. Fluids*, **17,** p. 873.

Pfefferle, L. D., Griffin, T. A., and Winter, M. (1988) Planar laser-induced fluorescence of OH in a chemically reacting boundary layer. *Applied Optics*, **27,** p. 3197.

Seitzman, J. M., Üngüt, A., Paul, P. H., and Hanson, R. (1990) Imaging and Characterization of OH Structures in a Turbulent Nonpremixed Flame. *Twenty-Third Symposium (International) on Combustion The Combustion Institute*, p. 637.

Smyth, K. C., Miller, J. H., Dorfmann, R. C., Mallard, W. G., and Santoro, R. J. (1985) Soot Inception in a Methane/Air Diffusion Flame as Characterized by Detailed Species Profiles. *Combustion and Flame* **62**, p. 157.

Sreenivasan, K. R., Ramshankar, R., and Meneveau, C. (1989) Mixing, Entrainment, and the Fractal Dimension of Surfaces in Turbulent Flows. *Proc. R. Soc. Lond.* **A421**, p. 79.

Vandsburger, U., Seitzman, J. M. and Hanson, R. K. (1988) Visualization Methods for the Study of Unsteady Nonpremixed Jet Flame Structure. *Combustion Science and Technology*, **59**, p. 455.

Wygnanski, I., Fiedler, H. (1969) Some Measurements of the Self-Preserving Jet. *J. Fluid Mech.* **38**, p. 577.

An update on the intermittency exponent in turbulence

K. R. Sreenivasan and P. Kailasnath
Mason Laboratory, Yale University, New Haven, Connecticut 06520-2159

(Received 27 July 1992; accepted 19 October 1992)

The issue of experimental determination of the intermittency exponent μ, is revisited and it is shown that the "best" estimate for it is 0.25 ± 0.05. This "best" estimate is obtained from recent atmospheric data, and is based on several different techniques.

Ever since Kolmogorov[1] introduced the intermittency exponent, more than a dozen attempts have been made to obtain its numerical value from experiments. The resulting estimates have varied from as low a value as 0.18 to as high as 0.7. (See Ref. 2 for a summary of early measurements, Table IV of Ref. 3 for measurements until about 1975 and Refs. 4–10 for experiments made thereafter.) It is unsatisfactory that this exponent, which plays a moderately important role in the theoretical framework of turbulence, should be known with no better certainty. We present in this Brief Communication a brief critique of the various definitions and experimental techniques used for determining the intermittency exponent, and provide the best estimate for it from recent atmospheric data.

Some of this variability is clearly due to differences in the definitions of the intermittency exponent, and it is therefore essential to describe all of them briefly. We find it convenient to adopt different symbols to denote the different definitions of the intermittency exponent. First, there is the constant μ_1 in Kolmogorov's lognormal hypothesis[1] given by

$$\sigma^2 = A + \mu_1 \log(L/r). \tag{1}$$

Here, σ^2 is the variance of the logarithm of ϵ_r, which is the energy dissipation averaged over an interval of size r, L is the "macro" or "integral" scale of turbulence, and the additive constant A is presumed to depend on the large scale of the flow.

On the basis of a generic self-similar cascade model—for relevant background, see Refs. 2 and 11; for a more modern interpretation in terms of multifractals, see Refs. 9, 10, and 12—we can write

$$\langle \epsilon_r^2 \rangle \sim r^{-\mu_2}. \tag{2}$$

From Novikov's[11] argument (discussed at some length in Ref. 2, Sec. 25), one can also write for homogeneous turbulence that

$$\langle \epsilon(x)\epsilon(x+r) \rangle \sim r^{-\mu_3}. \tag{3}$$

By Fourier transforming Eq. (3), one obtains for the spectral density of the energy dissipation $E_1^{\epsilon}(k) \sim k^{1-\mu_3}$, which we shall write as

$$E_1^{\epsilon}(k) \sim k^{1-\mu_4}. \tag{4}$$

Finally, use has also been made in the past of the definition that

$$\langle [\epsilon(x) - \langle \epsilon \rangle][\epsilon(x+r) - \langle \epsilon \rangle] \rangle \sim r^{-\mu_5}. \tag{5}$$

Equation (5) is equivalent to Eq. (3) only at very high Reynolds numbers.

It is safe to say that $\mu_2 = \mu_3$, and that $\mu_3 = \mu_4$ trivially. However, Eq. (4) may not yield satisfactory results because of crossover effects discussed by Nelkin;[13] these effects are important at all finite Reynolds numbers. Further, the scaling region apparent in one procedure may well be different from that in another. The quantity we shall call intermittency exponent is $\mu = \mu_2 = \mu_3$. The constants μ_4 and μ_5 are good approximations to μ only if the Reynolds number is very high. The constant μ_1 is not related to the other μ's except through the hypothesis of some cascade model.

We are now in a position to comment on experiments in more specific terms. Most of the early estimates of the intermittency exponent were made by using Eq. (4). Nelkin[13] pointed out the difficulty in estimating μ via μ_4 when the scaling range is finite and, with this background and a model calculation, deduced a value of 0.25 from Kholmyansky's[14] spectral data. Antonia *et al.*[5] followed up with an immediate experiment in a fairly high Reynolds number jet ($R_\lambda = 966$), and confirmed Nelkin's estimate. They obtained, by means of Eq. (3), the exponent to be around 0.2. This latter estimate was confirmed by Anselmet *et al.*,[6] who also used Eq. (3). It is interesting that Anselmet *et al.* found, from the same data at a moderate Reynolds number, that μ_5 was about 0.45, emphasizing the finite Reynolds number effect to which we have already alluded. The recent multifractal scaling work[9,10] has yielded a value of about 0.25 ± 0.05. These same experiments also showed that the measured value of μ_1 was about 0.23, in close agreement with 0.25. This may indicate that some kind of cascade process is not a bad model for turbulence.

Despite this seemingly conclusive evidence that the intermittency constant is about 0.25 ± 0.05, older estimates have often found favor in the literature. For example, Baker and Gibson,[7] and Gibson[8] have used a value of 0.5 for μ. Gibson (private communication) has indicated how the smaller value of 0.25 would imply, when used in conjunction with the lognormal model for the energy dissipation, an astronomical value for the energy-containing scale. It seemed that an effort at revisiting the issue, and settling it conclusively if possible, was worthwhile.

We systematically examined the various methods of determining the intermittency exponent using some recent data obtained in the atmosphere. Measurements were made in the atmospheric surface layer about 6 m above a long stretch of a wheat field canopy, and at a height of 2 m

 0899-8213/93/020512-03$06.00 © 1993 American Institute of Physics

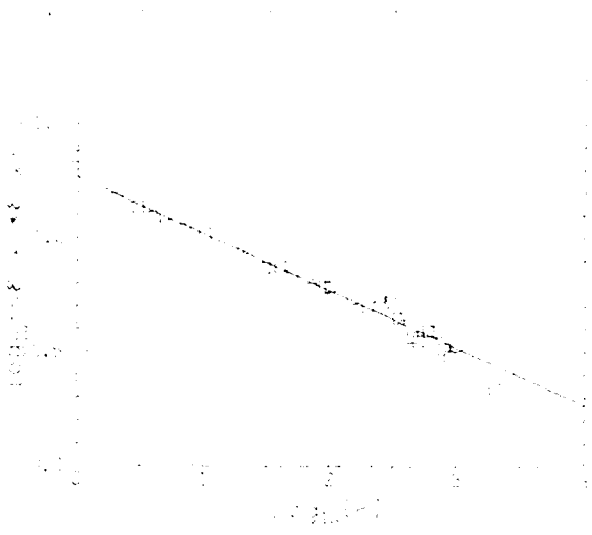

FIG. 1. The log–log plot of $\langle \epsilon(x)\epsilon(x+r)\rangle$ vs r (assuming Taylor's hypothesis). In this and the following two figures, r is expressed in terms of sampling units = 1/6000 sec and the wind velocity was 6 m/sec. The best estimate of $\mu = 0.25$. This so-called best estimate was obtained by trying various values of the exponent μ, and deciding upon the value of μ which yielded the best flat line in plots of (ordinate/$r^{-\mu}$) in Eq. (3).

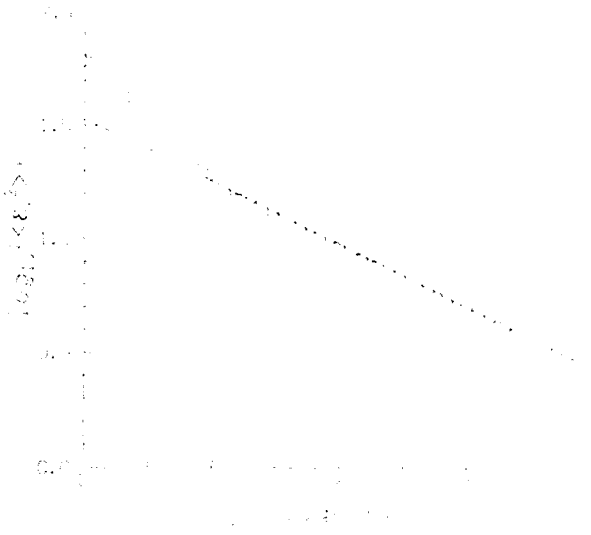

FIG. 2. The log–log plot of $\langle \epsilon_r^2 \rangle$ vs r for the same set of data used in Fig. 1. The best slope is 0.27.

above the roof of a four-story building. The mean wind velocity varied between 4 and 6 m/sec. Velocity fluctuations were measured using a standard hot wire (5 μm in diameter, 0.6 mm long) operated on the constant temperature mode on a DISA 55M01 anemometer. The anemometer voltage was digitized on a 12-bit digitizer at a sampling frequency of 6000 Hz. This sampling frequency was found to be adequate for capturing most of the small-scale fluctuations. The linearization of the signal yielded a time trace of the streamwise velocity fluctuation $u(t)$. The dissipation field was approximated by $(du/dt)^2$. This assumes that the space derivative could be approximated by the time derivative according to Taylor's frozen flow hypothesis, and that one component of dissipation is an adequate representation of the total dissipation statistically. It is believed that these approximations were not critical to the determination of the intermittency exponent. The internal Reynolds number based on the root-mean-square velocity and the Taylor microscale varied between 1500 and 2000.

The following characteristics of the data reassured us about their quality. The power spectral density showed a sizeable scaling range with a slope of approximately $-5/3$ (actually slightly steeper). The third-order structure function varied linearly with the separation distance[15] for more than a decade of variation in the separation distance.

The most unambiguous methods of determining μ are from the Eqs. (2) and (3); to our knowledge, all previous measurements that used these methods have given a value close to 0.25. Figures 1 and 2 from the atmospheric data show that both Eqs. (3) and (2) yield essentially the same answer, namely, μ is about 0.25. (Note, however, that the scaling ranges in the two figures are somewhat different.)

While the experience of Anselmet *et al.*[6] would suggest that there is little point in using Eq. (5), we obtain more or less the same exponent irrespective of whether we use Eqs. (4) or (5). See Fig. 3. We tentatively conclude that the discrepancy in the two methods of measurement in the experiments of Anselmet *et al.* is their lower Reynolds number.

We now use an alternative method for the determination of the intermittency exponent. This method uses the so-called multiplier distributions[4,11,12] appropriate to the inertial range. Briefly, the multipliers M_a are defined as the ratio of the energy flux (or the energy dissipation rate) contained in an eddy of size r in the inertial range to that in a box of size ar, where a is an integer that equals the number of subeddies into which a parent eddy is presumed to break up. The multipliers M_a are random variables that possess a well-defined probability density function, $p(M_a)$. In Ref. 12, it was shown that, for any given a, $p(M_a)$ is

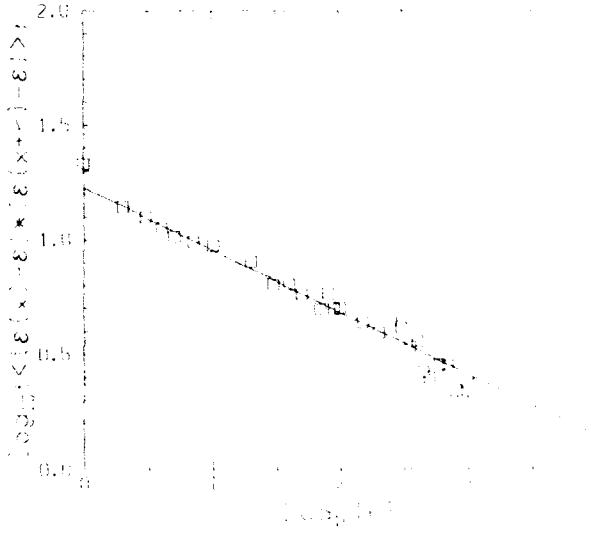

FIG. 3. $\langle [\epsilon(x)-\langle\epsilon\rangle][\epsilon(x+r)-\langle\epsilon\rangle]\rangle$ vs r for the same set of data used in Fig. 1. The best slope is 0.27.

independent of r for all r in the inertial range. Chhabra and Sreenivasan[12] obtained the distributions of these multipliers for several values of a, and published results for $a=2$, 3, and 5 (Fig. 2 of Ref. 12). The fact that $p(M_a)$ is independent of r for any given base a can be used to advantage in obtaining converged values of high-order moments that one would otherwise not be able to measure reliably. Although the probability density $p(M_a)$ depends on a, the various scaling exponents given by the multifractal spectrum are independent of a. In particular, the intermittency exponent is independent of the precise value of a chosen.

It is easy to compute μ_2 from multiplier distributions. Let us start with an eddy of size unity, and normalize the total energy dissipation in that eddy to be unity. Let such an eddy break down into a pieces, and let the energy dissipation contained in each piece (as a fraction of the total contained in the parent eddy) be picked randomly from the appropriate distribution $p(M_a)$. Let us examine the subeddies that have resulted after n steps in this cascade. By the definition of the multipliers, the amount of energy dissipation E_r contained in a box of size $r=a^{-n}$ is given by

$$E_r = \prod_{i=1}^{i=n} M_a(i). \tag{6}$$

Here, by the respective definitions of the two quantities, $E_r = r\,\epsilon_r$ (in one dimension). The product in Eq. (6) over the index i (which varies between 1 and the current step n of the cascade) occurs because the total energy dissipation E_r contained in a subeddy of size $r=a^{-n}$ is the product of the multipliers from one step to another starting with the scale unity. These multipliers will be chosen from the appropriate probability density function $p(M_a)$.

It follows that

$$\langle (E_r)^2 \rangle = \left\langle \left[\prod M_a(i) \right]^2 \right\rangle = \prod \langle M_a^2 \rangle, \tag{7}$$

where the products are taken over all values between 1 and n, and the angle brackets denote probability averages over the appropriate multiplier distribution. The last step follows because the multipliers are statistically independent of the step of the cascade. Noting that $E_r = r\,\epsilon_r = a^{-n}\epsilon_r$ and that $\Pi \langle M_a^2 \rangle = (\langle M_a^2 \rangle)^n$, we can show by a few steps involving only algebra that

$$\mu = \log_a \langle M_a^2 \rangle + 2. \tag{8}$$

From the probability distribution $p(M_a)$ measured in Ref. 12, we obtain that $\mu = 0.23 \pm 0.05$ for all three values of a (2, 3, and 5). This is consistent with the present estimates obtained by other methods. It should be noted that similar calculations made in Ref. 4 yielded values between 0.18 and 0.22. Van Atta and Yeh[4] also note that these values are consistent with Kholmyanski's result of 0.23.

Using the triangular approximation to $p(M_a)$ recommended in Ref. 12 for $a=2$, we can analytically show that $\langle M_a^2 \rangle = 7/24$, which gives $\mu = 0.22$. For the p model of Ref. 16, also for $a=2$, $\langle M_a^2 \rangle = 0.29$, which gives $\mu = 0.21$.

All these considerations lead us to conclude that the "best estimate" for the intermittency exponent is $\mu = 0.25 \pm 0.05$.

Incidently, all our estimates[3,17] for the intermittency exponent in the case of the scalar dissipation are in the vicinity of 0.35.

ACKNOWLEDGMENTS

One of us (KRS) is thankful for useful correspondence to Professor M. Nelkin (who also provided the impetus for this note) and Professor C. Gibson. We thank Mr. G. Stolovitzky for his help with multiplier distributions leading to Eq. (8).

The work was supported by the Air Force Office of Scientific Research.

[1] A. N. Kolmogorov, "A refinement of previous hypotheses concerning the local structure of turbulence in a viscous incompressible fluid at high Reynolds number," J. Fluid Mech. **13**, 82 (1962).

[2] A. S. Monin and A. M. Yaglom, *Statistical Fluid Mechanics* (MIT Press, Cambridge, MA, 1971).

[3] K. R. Sreenivasan, R. A. Antonia, and H. Q. Danh, "Temperature dissipation fluctuations in a turbulent boundary layer," Phys. Fluids **20**, 1238 (1977).

[4] C. W. Van Atta and T. T. Yeh, "Evidence for scale similarly of intermittency in turbulent flows at large Reynolds numbers," J. Fluid Mech. **71**, 417 (1975).

[5] R. A. Antonia, N. Phan-Thien, and B. R. Satyaprakash, "Autocorrelation and spectrum of dissipation fluctuations in a turbulent jet," Phys. Fluids **24**, 554 (1981).

[6] F. Anselmet, Y. Gagne, E. J. Hopfinger, and R. A. Antonia, "High-order velocity structure functions in turbulent shear flows," J. Fluid Mech. **140**, 63 (1984).

[7] M. A. Baker and C. H. Gibson, "Sampling turbulence in the stratified ocean: statistical consequences of strong intermittency," J. Phys. Oceanogr. **17**, 1817 (1987).

[8] C. H. Gibson, "Fossil turbulence and intermittency in sampling oceanic mixing processes," J. Geophys. Res. **96**, 20403 (1991).

[9] C. Meneveau and K. R. Sreenivasan, "The multifractal spectrum of the dissipation field in turbulent energy dissipation," Nucl. Phys. B (Proc. Suppl.) **2**, 49 (1987).

[10] C. Meneveau and K. R. Sreenivasan, "The multifractal nature of turbulent energy dissipation," J. Fluid Mech. **224**, 429 (1991).

[11] E. A. Novikov, "Intermittency and scale similarity in the structure of a turbulent flow," Appl. Math. Mech. **35**, 231 (1971) [original Russian in Prikl. Math. Mech. **35**, 266 (1971)].

[12] A. B. Chhabra and K. R. Sreenivasan, "Scale-invariant multiplier distributions in turbulence," Phys. Rev. Lett. **68**, 2762 (1992).

[13] M. Nelkin, "Do the dissipation fluctuations in high Reynolds number turbulence define a universal exponent?" Phys. Fluids **24**, 556 (1981).

[14] M. Z. Kholmyansky, "Measurements of the microturbulent fluctuations of the wind velocity derivative in an atmospheric surface layer," Izv. Akad. Nauk SSSR Fiz. Atmos. Okeana **8**, 818 (1972).

[15] A. N. Kolmogorov, "Dissipation of energy in the locally isotropic turbulence," Dokl. Akad. Nauk SSSR **32**, 19 (1941). For English translation, see Proc. R. Soc. London Ser. A **434**, 15 (1991).

[16] C. Meneveau and K. R. Sreenivasan, "Simple multifractal cascade model for fully developed turbulence," Phys. Rev. Lett. **59**, 1424 (1987).

[17] R. R. Prasad, C. Meneveau, and K. R. Sreenivasan, "The multifractal nature of the dissipation of passive scalars in fully turbulent flows," Phys. Rev. Lett. **61**, 74 (1988).